Total Cross Sections for Pion Charge Exchange on the Proton

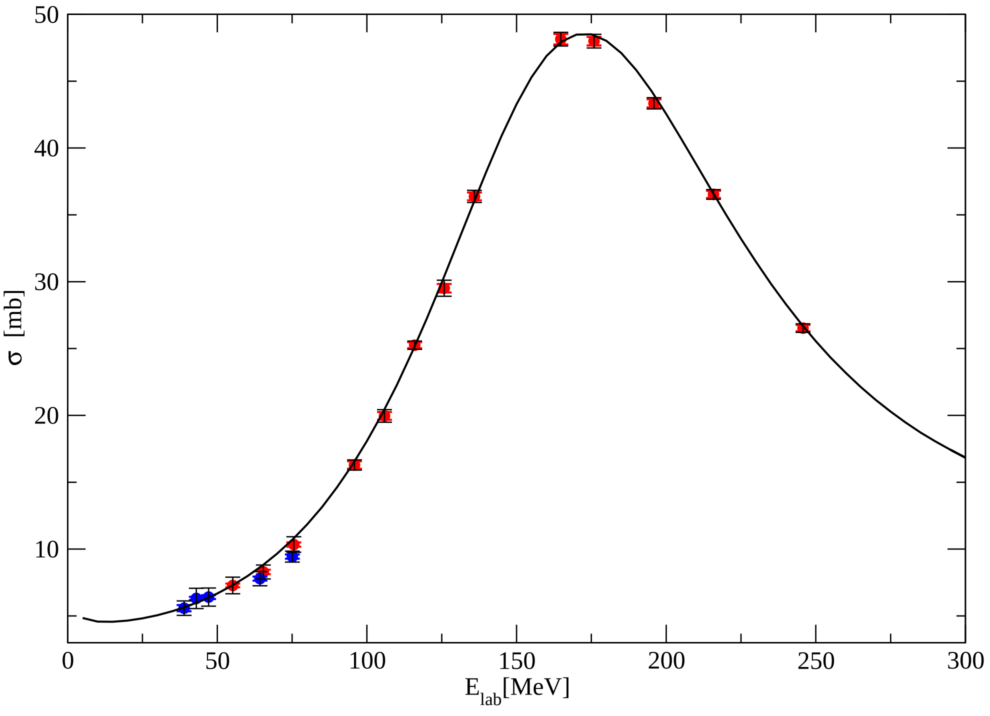

Dissertation

zur Erlangung des Grades eines Doktors
der Naturwissenschaften
der Fakultät für Mathematik und Physik
der Eberhard-Karls-Universität Tübingen

vorgelegt von
Johannes Breitschopf
aus Schwäbisch Hall

2006

Tag der mündlichen Prüfung 28.04.2006
Dekan: Prof. Dr. P. Schmid
1. Berichterstatter: Prof. Dr. G.J. Wagner
2. Berichterstatter: Prof. Dr. H. Clement

Zusammenfassung

In der QCD ist die Massendifferenz von Up- und Down-Quark die Ursache der Isospinbrechung in der starken Wechselwirkung. Als das am einfachsten zugängliche hadronische System bietet das πp-System den besten Zugriff auf die Verletzung der Isospinsymmetrie in der starken Wechselwirkung. In πp-Streuexperimenten ist die elastische $\pi^{\pm}p \rightarrow \pi^{\pm}p$ Streuung und die einfache Ladungsaustauschreaktion (SCX) $\pi^{-}p \rightarrow \pi^{0}n$ am leichtesten zu messen. Die Streuamplituden dieser drei Reaktionskanäle stehen in einer Beziehung zueinander, welche als "Dreiecksidentität" bezeichnet wird. Ist der Isospin erhalten, dann ist diese Relation erfüllt. Verschiedene Arbeitsgruppen haben in Analysen von Streudaten widersprüchliche Resultate mit Werten für die Isospinbrechung zwischen 0.7 % und 7 % erhalten. Die Ergebnisse dieser Analysen sind jedoch durch den geringen Umfang und die Ungenauigkeit der SCX-Datenbasis beeinträchtigt. Aus diesem Grunde wurde ein Meßprogramm zur Verbesserung der SCX-Meßdaten durchgeführt. Diese Arbeit beschreibt die Messung des totalen SCX-Wirkungsquerschnittes mit der Hilfe eines neuen 4π-Szintillationsdetektors. Der in der Messung abgedeckte Energiebereich für einlaufende Pionen beträgt 38 bis 250 MeV. Die verwendete Meßmethode mißt die Transmission eines Strahls monoenergetischer negativer Pionen an einem Protonentarget durch Vergleich der Intensitäten von ein- und auslaufenden geladenen Pionen. Auf diese Weise werden Ereignisse mit neutralen Reaktionsprodukten gezählt. Drei Zähler, die der Strahldefinition dienen, detektieren die einlaufenden negativen Pionen. Der 4π-Szintillationsdetektor, der das Target umgibt, ist nicht empfindlich auf die bei der SCX-Reaktion entstehenden neutralen Teilchen. Um den totalen SCX-Wirkungsquerschnitt von Wasserstoff zu erhalten, wurden sukzessive Messungen mit einem CH_2-Target, einem C-Target und einem Leertarget durgeführt. Daraus wird der totale SCX-Wirkungsquerschnitt von Wasserstoff ermittelt. Ein wesentlicher Teil dieser Arbeit besteht aus einer umfangreichen, auf Einzelereignissen basierenden Offline-Datenanalyse. Dafür wurden zu jedem Ereignis die Meßdaten aller im Experiment beteiligten QDC, TDC und FADC Module verwendet. In der Datenanalyse wurden verschiedene Korrekturen auf die Daten angewendet. Diese sind die Korrektur auf zufällige Ereignisse, die Detektion der ungeladenen Teilchen im Detektor, den Dalitz-Zerfall, den Pion-Zerfall und den Pion-Einfang. Als bisher einziges Experiment deckt diese Messung die Δ-Resonanz und die sp-Interferenzregion in *einem* experimentellen Aufbau ab und verbessert damit deutlich die vorhandene SCX-Datenbasis. Eine Genauigkeit von besser als 2 % wurde fast durchweg erreicht. Lediglich bei Energien unterhalb von 80 MeV stieg der Meßfehler infolge von Absorptionseffekten in den Targets an. Signifikante Abweichungen von früheren Messungen wurden i. a. nicht beobachtet. Die Kontroverse zwischen früheren Transmissionsexperimenten wurde zu Gunsten der früheren Messungen von Bugg et al. entschieden. Die interessanteste Abweichung von anderen Messungen wie auch von den Vorhersagen der SAID FA02 Streuphasenanalyse wurde im Bereich 60 bis 90 MeV gefunden, wo dieses Experiment signifikant kleinere Wirkungsquerschnitte ergibt. Es wird versucht die Abweichung als Ergebnis einer Isospinbrechung zu verstehen. Die s-Wellen Amplituden sind durch elastische Pion-NuKleon Streudaten gut festgelegt. Es wird gezeigt, daß die Beschreibung der SCX-Wirkungsquerschnitte dadurch verbessert werden kann, daß die s-Wellen Amplituden um $(4 \pm 1.5)\%$ verringert werden. Der genaue Wert ist abhängig von den verwendeten SCX-Daten und von den Parametern der Δ^0 Breit-Wigner Resonanz, welche die p_{33}-Welle beschreibt. Dies zeigt auf, daß zur Bestimmung der Isospinbrechung sowohl s-Wellen- als auch p-Welleneffekte mit eingeschlossen werden sollten. Interessanter Weise stimmen unsere für die Δ^0-Resonanz erhaltenen Parameter besser mit denen der Δ^{++}-Resonanz überein als bisher angegeben.

Abstract

In QCD the mass difference of the up- and down-quarks is the origin of the isospin violation in the strong interaction. The pion-nucleon system is the simplest accessible system which provides information about the isospin breaking in the strong interaction. There are three experimentally accessible reaction channels which may be used to obtain information about the role of isospin in the πN system: $\pi^{\pm}p \rightarrow \pi^{\pm}p$ elastic scattering and the single charge exchange (SCX) $\pi^{-}p \rightarrow \pi^{0}n$. The amplitudes for these reactions fulfill a triangle relation if isospin is conserved. Various tests from several groups result in contradictory outputs with an isospin violation ranging from 0.7 % to 7 %. What arises from these different results is that the analyses are severely affected by the small amount of SCX data. Therefore a program to increase the available SCX data base was undertaken. This work describes the measurement of total SCX cross sections employing a new 4π scintillation counter to perform transmission measurements in the incident pion energy range from about 38 to 250 MeV. The main focus was to obtain improved accuracy in comparison to existing measurements in the energy region below 100 MeV. A small 4π detector box consisting of thin plastic scintillators has been constructed. The transmission technique, which was used, relates the number of transmitted charged pions to that of incident beam pions and this way effectively counts events with neutral products. The incoming negative pions were counted by three beam defining counters before they hit a target of very well known size and chemical composition. The target was placed in the box detector which was not sensitive to the neutral particles resulting from the SCX. The total cross section for emerging neutral particles was derived from the comparison of the numbers of the incoming and transmitted charged particles. The total SCX cross section on hydrogen was derived from the transmissions of a CH_2 target, a carbon target and an empty target. For a detailed offline analysis all TDC, QDC and FADC information was recorded in an event by event mode for each triggered beam event. Various corrections had to be applied to the data, such as random correction, the detection of neutrals in the detector, Dalitz decay, pion decay and the radiative pion capture. This measurement covers, as the only experiment, the whole Δ-resonance and the sp-interference region in *one single* experimental setup and improves the available data base for the SCX reaction. An accuracy of better than 2 % was achieved for almost all energies. Unfortunately at energies below 80 MeV unforeseen experimental problems with absorption effects, energy loss in the targets and a careful analysis resulted in increased errors at low energies. In general the results of this experiment show no significant discrepancies with previous measurements. The dispute between former transmission experiments was settled in favor of the early measurement of Bugg et al.. The most interesting discrepancy to former experiments as well as to the SAID FA02 partial wave analysis was found in the range form 60 to 90 MeV were the results of this measurement are significantly smaller. This deviation can be understood as a result of an isospin violation. It is shown that the description of the SCX cross sections is improved if the s-wave amplitudes, that have been fixed essentially by elastic pion-nucleon scattering data, is reduced by (4 ± 1.5)%. The exact value depends on the SCX literature data included and on the parameters of the Δ^0 Breit-Wigner resonance describing the p_{33}-waves. This shows that p-wave as well as s-wave effects should be considered in studies of isospin symmetry breaking. Interestingly, our best fit parameters of the Δ^0-resonance are much closer to that of the Δ^{++}-resonance than previously reported.

Contents

Chapter 1

Introduction

Carrying a mass of $m_\pi \approx 140$ MeV/c^2 the pion is the lightest strongly interacting particle. Existing in three charged states (π^+, π^-, π^0) the *pseudo scalar meson* can be generated and annihilated individually as a boson with spin and parity $J^\pi = 0^-$. Posited by Yukawa [Yuk35] as the exchange particle of the strong interaction in 1935 the pion was first discovered about 10 years later in cosmic radiation. Among the hadrons the pion has an exceptional position. It is the lightest hadron and hence responsible for the long range part of the NN-interaction. With a mass of $m_\pi \approx 938$ MeV/c^2 the proton belongs to the family of *baryons*. With spin and parity $J^\pi = \frac{1}{2}^-$ the proton is observed to be stable. The nuclei of the elements are composed of protons and neutrons held together by the strong interaction. Even nowadays experimental access to the simplest hadronic system, the $\pi\pi$-system, is not possible due to the short lifetime of the pions and the lack of high density pion beams. Only the creation of pionium[1] provides limited access to the $\pi\pi$-system but involves big effort [DIR94]. For that reason the simplest experimentally accessible hadronic system is the pion-nucleon-system (πN-system). Fundamental observables of the strong interaction can be extracted from πp-scattering data in particular the πNN-coupling constant, the σ-term of the nucleon and the isospin breaking of the strong interaction.

-πNN coupling constant:
The binding of the nucleons can be characterized by meson exchange models. The coupling constant gives the strength of the interaction and can be determined from NN-scattering or πN-scattering.

-πN sigma term:
The sigma term is a fundamental parameter of low energy hadron physics and provides a measure of chiral symmetry breaking. The sigma term is connected to the strange quark content in the nucleon and may be derived from an extrapolation of the πN-scattering amplitudes to the unphysical Cheng-Dashen Point.

-Isospin invariance:
For a long time isospin was considered to be conserved in particle reactions caused by the strong interaction. Modern Quantum Chromodynamics (QCD) includes small isospin breaking based on the up- and down-quark mass difference. The knowledge of the size of the isospin breaking would lead to a better determination of the quark masses.

None of these quantities are presently determined with satisfactory agreement between the various analyses. For that reason our group is involved in various πp-scattering experiments [Den04], [Mei04] to determine these observables. This thesis contributes to the problem of isospin breaking in the strong interaction by improving the πp-scattering data base.

As a physical quantity and mathematically analogous to the spin, Werner Heisenberg established the isospin T in 1932. His motivation was the fact that the strong interaction is almost the same between two protons, two neutrons or between a proton and neutron pair (in a spin 0 state). The difference of the properties basically results from the electromagnetic interac-

---

[1] pionium = atom consisting out of π^+ and π^-

tion, hence the neutron and proton can be considered as the same particle with two isospin states. This is similar to the spin up and spin down orientation of a spin 1/2 particle, described simply by two states of the same particle instead of treating it as two particles. The proton and neutron represent an isospin doublet with $T = 1/2$ with the third component $T_z = +1/2$ and $-1/2$. The pion exists in three charged states and is interpreted as an isospin triplet with $T = 1$ and $T_z = +1, 0, -1$. The third component is related to the charge and is conserved in all interactions. Even if the electromagnetic effects are neglected, the neutron and the proton are not completely symmetric and the neutron is slightly more massive than the proton since electromagnetic effects alone would suggest a proton mass exceeding that of the neutron. This suggests that isospin is not a conserved variable in the strong interaction. The remaining mass difference of the two nucleons can be traced back to the different masses of the up- and down-quarks and the conclusion is that the isospin conservation in the strong interaction is violated. The exact knowledge of the masses of the up- and down- quark would give access to the size of the isospin breaking but the confinement resulting from the quantum Chromodynamics (QCD) prohibits the appearance of free quarks. This makes a determination of quark masses indirect and model dependent. In the literature the so called "current-quark masses"are presently quoted with $m_{\mathrm{up}} = 1.5 - 4.5$ MeV and $m_{\mathrm{down}} = 5 - 8.5$ MeV [PPB02]. The mass ratio $m_{\mathrm{up}}/m_{\mathrm{down}}$ was calculated using chiral symmetry and the known pion and kaon masses. But the question of the free quark masses is under steady discussion and far from being solved.

Another access to test the isospin symmetry in the strong interaction is provided by the πN-system. With five valence quarks the πN-system is the simplest experimentally accessible hadronic system. Direct access to the isospin invariance is possible in elastic $\pi^{\pm}$p-scattering and the $\pi^- p \rightarrow \pi^0 n$ -charge exchange reaction (SCX). From different analysis of πp-scattering data and experiments with pionic atoms isospin breaking ranging from 0.7 % to 7 % was derived recently. As the source of the discrepancy in the results one quickly finds the πp-data base. While the elastic scattering data base contains reliable data covering the Δ-resonance, for energies below 100 MeV there was an obvious need for further data to be taken. Therefore much effort has been made also by our group to gain more elastic scattering data at low energies [Den04], [Mei04]. The situation for the SCX data base is even worse. Most of the existing data are from differential cross section measurements which cover only a small energy range or lack high precision. The extraction of total cross sections from differential measurements is straight forward but for the used experimental setups complex Monte Carlo simulations were involved. Only two direct measurements of total SCX cross sections currently exist. Additionally, not a single experiment covers the whole Δ-resonance region and the sp-interference region. This work describes the measurement of the total cross section for pion proton single charge exchange performed with a new 4π-scintillation detector used for a transmission experiment. Chapter 2 gives an overview of πp-scattering and the access to isospin breaking. In Chapter 3 the principle of the measurement is described while Chapter 4 explains the detector setup. The measurements taken are outlined in Chapter 5 and the data analysis is described in Chapter 6. Monte Carlo simulations have been made to correct the data for various effects, these and further corrections are described in Chapter 7. The question of the applied statistical and systematical errors is addressed in Chapter 8 and the experimental tests are discussed in Chapter 9. In Chapter 10 the results are presented and a short discussion is included where estimates of the size of the isospin breaking are given. This thesis closes with a final short outlook given in Chapter 11.

Chapter 2

The role of pionic Single Charge eXchange on the proton (SCX)

2.1 Isospin breaking in the πp-system

The easiest experimentally observable processes within the πN-system are the elastic scattering and charge exchange reactions of charged pions on the proton:

$\pi^+\mathrm{p} \rightarrow \pi^+\mathrm{p}$	elastic scattering
$\pi^-\mathrm{p} \rightarrow \pi^-\mathrm{p}$	elastic scattering
$\pi^-\mathrm{p} \rightarrow \pi^0\mathrm{n}$	single charge exchange (SCX)

The study of these reactions contributes to the understanding of the strong interaction. Within the isospin formalism the SCX reaction is connected with the elastic $\pi^\pm$-scattering. Hence isospin symmetry can be tested by measurements of this three reaction channels. Under the *assumption of isospin symmetry* the scattering amplitudes of the channels can be expressed by the two isospin amplitudes $A_{\frac{1}{2}}$ and $A_{\frac{3}{2}}$:

$$A_+ = A_{\pi^+p\rightarrow\pi^+p} = A_{\frac{3}{2}} \tag{2.1}$$

$$A_- = A_{\pi^-p\rightarrow\pi^-p} = \frac{1}{3}A_{\frac{3}{2}} + \frac{2}{3}A_{\frac{1}{2}} \tag{2.2}$$

$$A_0 = A_{\pi^-p\rightarrow\pi^0n} = \frac{\sqrt{2}}{3}(A_{\frac{3}{2}} + A_{\frac{1}{2}}) \tag{2.3}$$

This is an overdetermined system of equations and resolves into the “triangle relation”

$$\sqrt{2}A_0 = A_+ - A_-. \tag{2.4}$$

Therefore a measurement of all three reaction channels allows the verification of the isospin invariance in the hadronic system once all Coulomb effects have been properly accounted for. The test is done by first obtaining A_0^{SCX} directly from single charge exchange. Then A_0^{SCX} is compared to $A_0^{elastic}$ extracted from elastic scattering data using the isospin triangle identity (2.4). From chiral perturbation theory the difference of A_0^{SCX} and $A_0^{elastic}$ is estimated to be $1 - 2$ % [Fet99]. In experiments with pionic atoms no significant isospin breaking was found [Cha97]. A recent work by Fettes and Meißner et al. [Fet01] implies an isospin breaking of 0.7 % while two recent empirical analyses by Gibbs et al. [GAK95] and Matsinos et al. [Mat97b] show large isospin violation on the 7 % level for the s-wave amplitude around $E_\pi = 40 - 50$ MeV. As a word of caution Meißner et al. emphasize that their results can not directly be compared to the empirical results because the mass differences between charged pions and the π^0 as well as electromagnetic effects are explicitely treated in their work while this is not the case in the other analysis.

A closer look at [Mat97b] and [GAK95] shows that their seeming agreement could be accidental and that there exist indeed discrepancies which could be partly due to deficiencies in the πp-data base. The analyses of Gibbs et al. and Matsinos et al. give consistent results for the differential

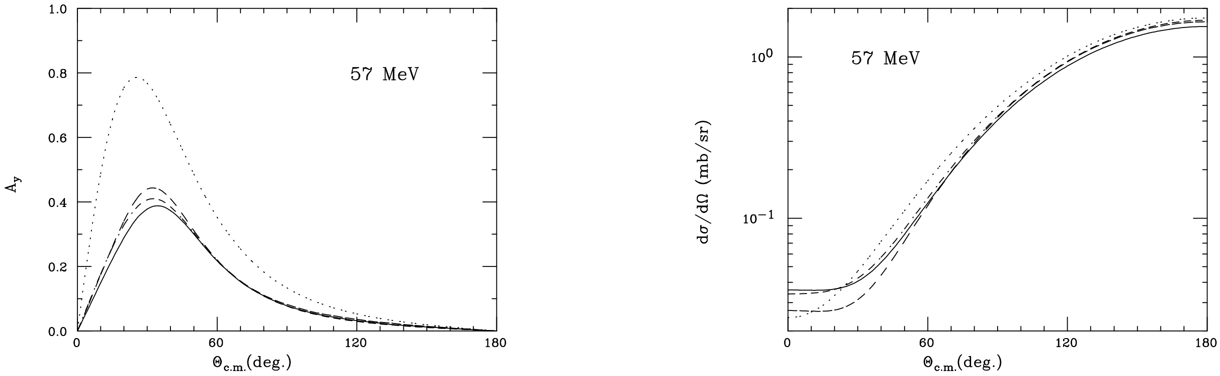

Figure 2.1: *Analyzing powers (left) and differential cross sections (right) for the SCX reaction calculated with amplitudes fitted to elastic cross sections and SCX cross sections respectively for 57 MeV (from [Com99]):*
- *Solid line: from elastic scattering, Gibbs et al.*
- *Dot-dashed line: from elastic scattering, Matsinos et al.*
- *Dashed line: from SCX, Gibbs et al.*
- *Dotted line: from SCX, Matsinos et al.*

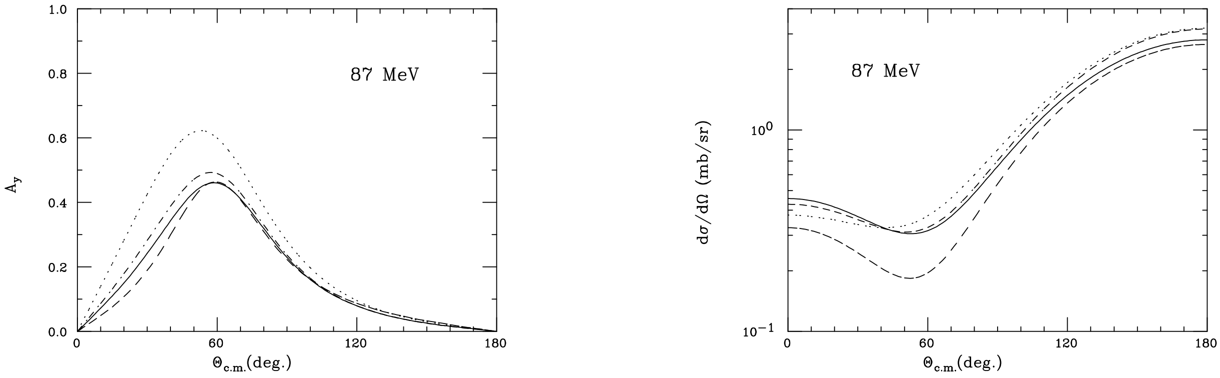

Figure 2.2: *As fig. 2.1, but for 87 MeV (from [Com99]).*

SCX cross sections calculated from elastic $\pi^{\pm}$-scattering via the triangle identity (2.4). However the differential SCX cross sections extracted from the SCX amplitudes (Matsinos et al. and Gibbs et al.) show significant differences to the cross sections extracted from elastic scattering as well as between each other. As an example the results of the two analyses are shown in fig. 2.1 and 2.2 for pion energies of 57 and 87 MeV.

Another access to isospin breaking provides the Quantum Chromodynamics (QCD) with quarks as elementary particles and gluons as exchange particles of the strong interaction. In the simple quark model the nucleons are bound states of three quarks and the pions are bound states of quark anti-quark pairs. Then the πN-system contains five valence quarks.

$$|p\rangle = |uud\rangle \quad |n\rangle = |ddu\rangle$$

$$|\pi^+\rangle = |u\overline{d}\rangle \quad |\pi^-\rangle = |\overline{u}d\rangle \quad |\pi^0\rangle = \frac{1}{\sqrt{2}}(|u\overline{u}\rangle - |d\overline{d}\rangle)$$

The isospins of the pion and nucleon combine to $T = 1/2$ or $T = 3/2$. All possible pion-nucleon reaction channels are described in the isospin formalism by the scattering amplitudes $A_{\frac{1}{2}}$, $A_{\frac{3}{2}}$ with the total isospin $T = 1/2$ or $T = 3/2$ and the πN-states can be obtained with the Clebsch-Gordan-coefficients.

In QCD quarks are described as carrying a color charge and their interaction is via gluons. The Lagrangian for the up-, down- and strange-quark flavors is

$$\mathcal{L}_{QCD} = \sum_{k=u,d,s} \overline{q}_k i\gamma^\mu(\partial_\mu - ig\frac{\lambda^a}{2}A^a_\mu)q_k - \frac{1}{2}trG^a_{\mu\nu}G^{a\mu\nu} - \sum_{k=u,d,s} m_k\overline{q}_k q_k \tag{2.5}$$

where g is the coupling constant of the strong interaction. q_k indicates the quark fields, A the gluon gauge fields and λ the Gell-Mann matrices. The last term is the quark mass term which is written, only considering the up- and down-quarks, as

$$m_u\overline{u}u + m_d\overline{d}d.$$

This can be rewritten as

$$m_u\overline{u}u + m_d\overline{d}d = \underbrace{\frac{m_u + m_d}{2}(\overline{u}u + \overline{d}d)}_{\text{chiral symmetry breaking}} + \underbrace{\frac{m_u - m_d}{2}(\overline{u}u - \overline{d}d)}_{\text{isospin violation}}. \tag{2.6}$$

The first (isoscalar) term is a direct measurement of the explicit breaking of chiral symmetry and intimately related to the sigma term. The second (isovector) term relates the breaking of isospin symmetry in the strong interaction [Fet01] to the difference of the up- and down-quark masses. The quark masses are free parameters in QCD and high precision experiments which measure the observables in equation 2.6 are matter of concern.

2.2 Database of the πp-scattering

The question of isospin breaking in the πN-system is far from being solved. While a consistent data base for differential cross sections [Pav01] and analyzing powers for elastic πp-scattering [Sev89], [Hof98] and [Hof03] exists today for pion energies covering the delta resonance, there is a lack of data for elastic scattering and for SCX observables at lower pion energies. Therefore as part of an extensive effort of our group analyzing powers were measured for elastic $\pi^{\pm}$-scattering at the **P**aul-**S**cherrer-**I**nstitut (PSI), Villigen, Switzerland [Mei04] as well as differential cross sections [Den04] at TRIUMF[1], Vancouver, BC, Canada. Fig. 2.3 shows the results from the TRIUMF measurements [Den04]. It can be seen that the SAID[2] predictions are in relatively good agreement with the data. With these experiments the situation of elastic scattering data has undergone a great improvement.

Data for the SCX reaction were mainly taken as differential cross sections relying on the detection of gamma rays from the decay of the π^0. As suggested from figs. 2.1 and 2.2 the experiments by Comiso et al. [Com75], Salomon et al. [Sal84], Bagheri et al. [Bag88b], Frank et al. [Fra67], Berardo et al. [Ber72] and Sadler et al. [Sad04] do not provide a consistent data base. The experiment of Comiso et al. only covers part of the Δ-resonance and exhibits

---

[1] TRIUMF = **TRI** **U**niversity **M**eson **F**actory

[2] **S**cattering **A**nalysis **I**nteractive **D**ialin, a partial wave analysis facility, which applies partial wave fits to the existing world data base of πp-scattering and does consistency checks as well. http://lux2.phys.va.gwu.edu/

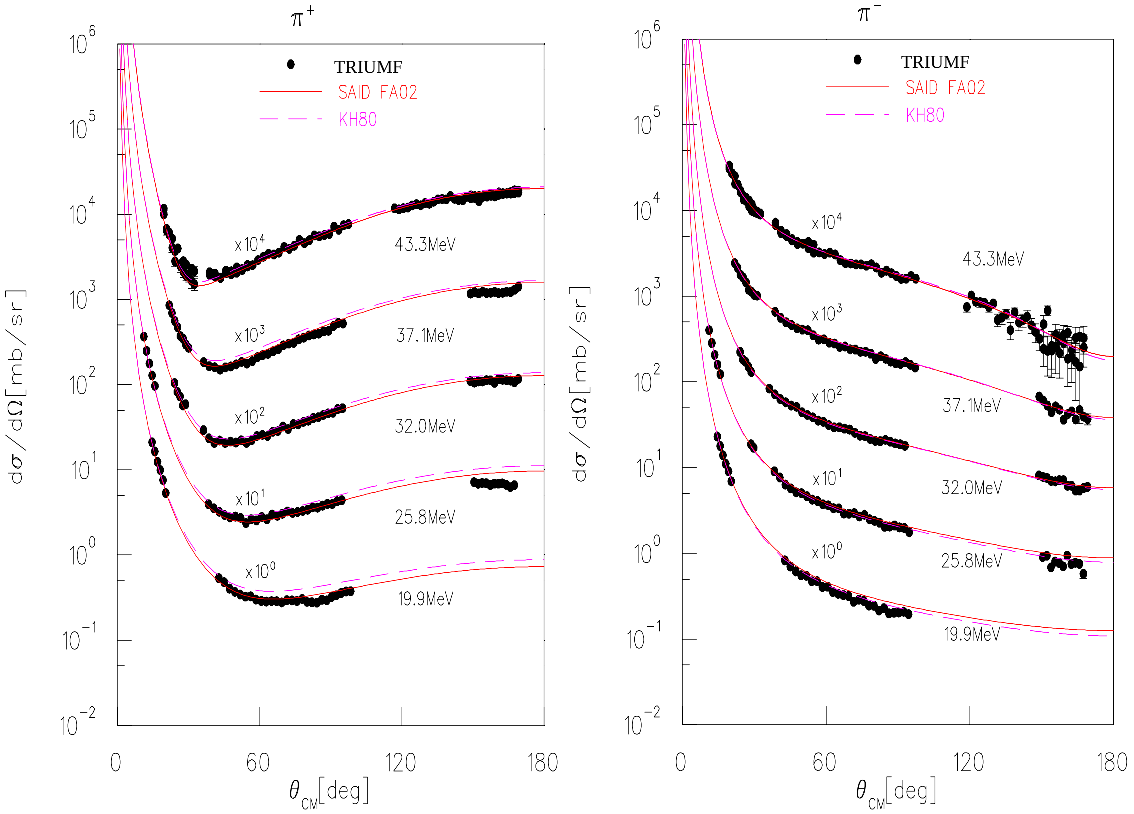

Figure 2.3: *Differential cross sections for πp elastic scattering at low energies [Den04] compared to predictions from phase shift analysis [SAID] (from fall 2002 (FA02)) [KH80].*

very large errors. The data of Frank et al. and Berardo et el. contribute only one data point below 300 MeV each. The results of Salomon et al. and Bagheri et al. only cover the low energy region. The data of Sadler et al. nicely cover the Δ-resonance but the errors are very large. The experiments measuring the total cross section directly applied a totally different independent method, the transmission method, which is used in the present thesis and which is further discussed in Section 3.2. The detectors of these experiments did not have 4π solid angle coverage and did not measure at pion energies below the resonance. The low energy region becomes important for the question of isospin breaking in the s-wave amplitudes due to the fact that the s-wave amplitudes become dominant there. Fig. 2.4 shows the s- (dotted-dashed) and p-wave (dashed) content of the total SCX cross section (solid). The s- and p-waves are sufficient to describe the SCX cross section in the plotted energy range from $15 - 300$ MeV. Waves of higher order become relevant for higher energies. Figs. 2.5 and 2.6 show some selected data sets.

In fig. 2.6 the data points are plotted with the SAID prediction (solid line) and calculated SAID predictions obtained with an assumed isospin breaking in the s-wave amplitude of $\pm$ 7 % (dotted lines). It was calculated using equation 10.3 (with the factor $f = 0.93$ and 1.07 which will be introduced in Section 10.3.1). It is obvious that high precision measurements are needed if an isospin breaking with a precision of a few percent is to be tested experimentally.

2.3 Partial wave representation of the total SCX cross section

The partial waves representation can be used to link the theoretical models with the experimental data. The approach introduced in this Section will be used later for a fit to the data.

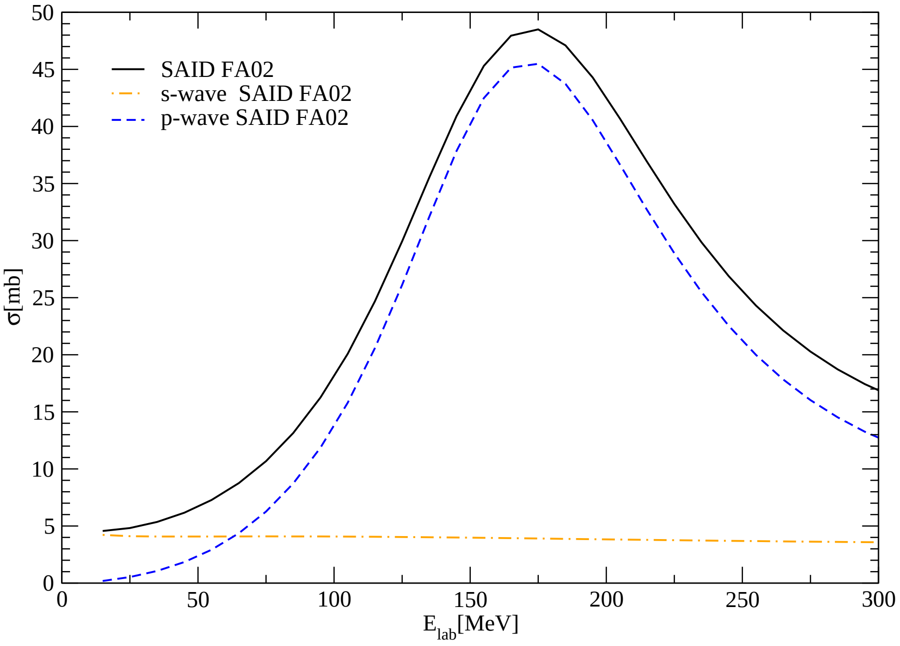

Figure 2.4: *s- and p-wave content of the total SCX cross section (solid line) calculated from the SAID predictions using equation 2.13.*

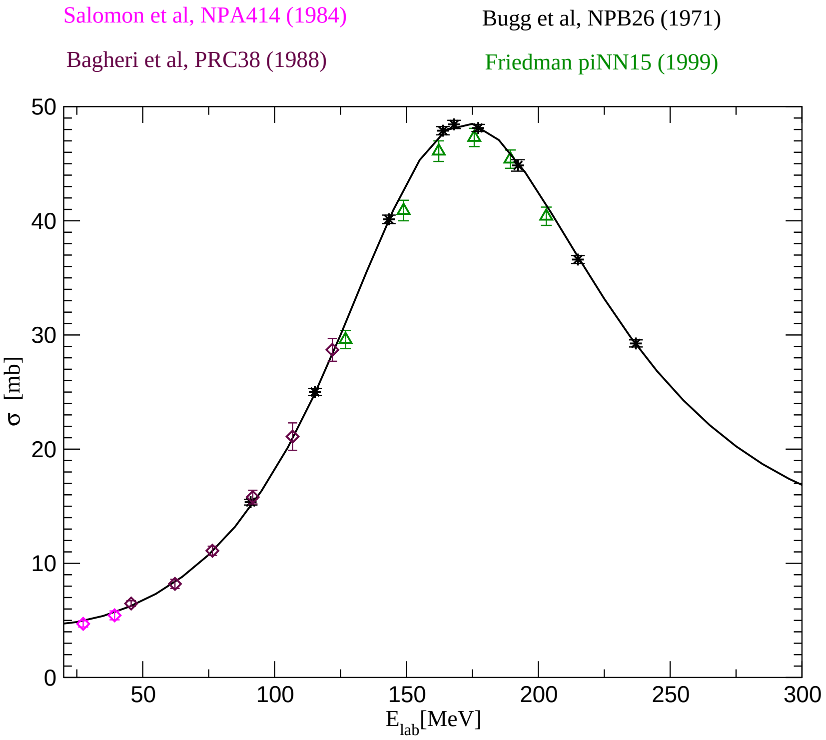

Figure 2.5: *SCX data base compared with predictions from SAID FA02 (solid line). Shown are only selected data sets.*

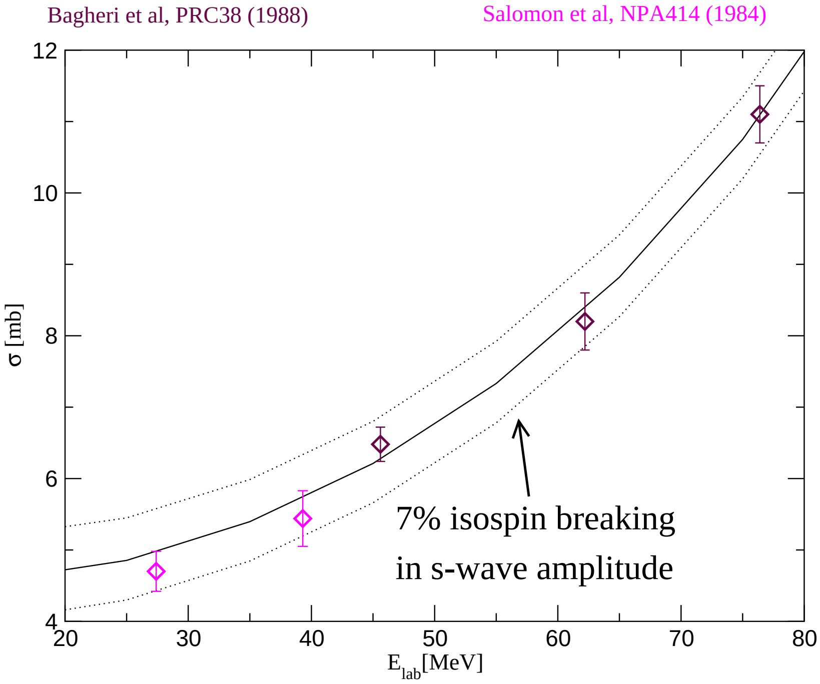

Figure 2.6: *SCX data base at low energies compared with predictions from SAID FA02 (solid line). The dotted lines show the calculated SAID FA02 results assuming ± 7 % isospin breaking in the s-wave amplitude.*

The wave function of a scattered spinless particle from a spherically symmetric potential can be considered as a superposition of an incident plane wave and an outgoing spherical wave:

$$\psi(\mathbf{r}) = \frac{1}{\sqrt{k}}\left(e^{i\mathbf{kr}} + f(\mathbf{k}',\mathbf{k})\frac{e^{ikr}}{r}\right) \qquad \text{with } r = |\vec{r}| \;\text{ and } k = |\vec{k}| \tag{2.7}$$

The differential cross section is given by

$$\frac{d\sigma}{d\Omega} = |f(\mathbf{k}',\mathbf{k})|^2. \tag{2.8}$$

The phase shift analysis provides the πN-scattering amplitude $f(\mathbf{k}',\mathbf{k})$ expanded in Legendre polynomials $P_l(cos\theta)$. With the conservation of the total angular momentum j, the orbital angular momentum l and the isospin T, f can be written as [Kol69]

$$f(\mathbf{k}',\mathbf{k}) = \sum_T Q_T \sum_l (2l+1) \sum_j \widehat{P}_{l,j} \alpha^l_{2T,2j}(k) P_l(cos\theta). \tag{2.9}$$

In the low energy approximation the $\alpha^l_{2T,2j}(k)$ term corresponds to the scattering amplitudes with T, j and l as quantum numbers. Q_T is the isospin projection operator which can be expressed for $T = 1/2,\ 3/2$ as

$$Q_{1/2} = \frac{1}{3}(1 - t\tau), \quad Q_{3/2} = \frac{1}{3}(2 - t\tau) \tag{2.10}$$

with t as the π isospin operator and τ the nucleon Pauli isospin operator. The spin projection operator $\widehat{P}_{l,j}$ may be expressed in terms of the orbital momentum operator L and the nucleon (Pauli) spin operator σ

$$\widehat{P}_{l,j=l-1/2} = \frac{l - \sigma \cdot L}{2l+1}, \quad \widehat{P}_{l,j=l+1/2} = \frac{l + 1 + \sigma \cdot L}{2l+1} \tag{2.11}$$

Using the relation

$$\sigma \cdot L P_l(cos\theta) = +i\sigma \cdot n P_l'(cos\theta)$$

[Kol69], where $P_l'(cos\theta)$ denotes the derivative of $P_l(cos\theta)$, and equation (2.10) for low energies (only s- and p-waves included) one gets

$$f(\mathbf{k}', \mathbf{k}) = \sum_T Q_T \{\alpha^0_{2T,1} + (\alpha^1_{2T,1} + 2\alpha^1_{2T,3}) cos\theta - i\sigma \cdot n(\alpha^1_{2T,1} - \alpha^1_{2T,3}) sin\theta\}. \tag{2.12}$$

With the more convenient notation of S_{2T2j} for $\alpha^0_{2T,2j}$ and P_{2T2j} instead of $\alpha^1_{2T,2j}$ the total cross section can be written as

$$\sigma = [|S_{11} - S_{31}|^2 + 2|P_{13} - P_{33}|^2 + |P_{11} - P_{31}|^2] \frac{2 \cdot 4\pi}{9 \cdot k_i^2} \frac{k_f}{k_i}, \tag{2.13}$$

with the wave numbers k_i and k_f in the c.m. system,

$$k_i = \left[\frac{m_p^2 (T_{\pi^-}^2 + 2m_{\pi^-} T_{\pi^-})}{(m_p + m_{\pi^-})^2 + 2m_p T_{\pi^-}} \right]^{\frac{1}{2}} \frac{1}{\hbar c}$$

and

$$k_f = \left[\frac{m_n^2 (T_{\pi^0}^2 + 2m_{\pi^0} T_{\pi^0})}{(m_n + m_{\pi^0})^2 + 2m_n T_{\pi^0}} \right]^{\frac{1}{2}} \frac{1}{\hbar c},$$

where T_π is the kinetic energy in the lab system. This formulation will be used in Section 10.3 to evaluate the results of the experiment in context of isospin breaking. As shown in fig. 2.4 the s- and p-waves are sufficient to describe the total cross section in the plotted energy range. For larger energies d-waves and waves with higher order become more relevant. Note that due to the nature of the total cross section there is no interference term between amplitudes with different angular momentum l.

Chapter 3

Experimental method

The object of this work is the measurement of the total cross section of the SCX reaction $\pi^- p \to \pi^0 n$. The outgoing π^0's have a mean life of $\tau_{\pi^0} = (8.4 \pm 0.6) \cdot 10^{-17}$ s and 99.98 % decay into two gammas or into an electron positron pair, the so called Dalitz decay. The relative ratio of these decay channels is

$$\pi^0 \to 2\gamma \ (98.798\ \%) \qquad \text{or} \qquad \pi^0 \to e^+e^-\gamma \ (1.198\ \%).$$

The SCX on the proton is the only reaction type with only outgoing neutral particles. To access the reaction one can use two different experimental methods. One obvious technique is the detection of the outgoing neutrals, the neutron and/or gammas from the π^0 decay. A totally different and independent method is a transmission experiment with detection of the transmitted charged pions or recoiling protons. On an hydrogen target disappearing charged pions are uniquely associated with a SCX reaction. From a reaction on targets other than hydrogen generally also charged reaction products emerge. The transmission technique was used in this work.

3.1 Detection of neutrals

Measurements of the SCX cross section by detecting the outgoing neutrals were made in earlier experiments at low energies e. g. by [Sal84], [Bag88a] at TRIUMF[1], Vancouver, BC, Canada. In these experiments a NaJ-crystal was used to detect the γ rays from the π^0 decay. Furthermore other measurements [Com75], [Ber72] using the neutron-photon coincidence method with detection of one of the outgoing gammas [Fra67] were performed.
The latest measurement of the SCX by detecting the outgoing neutrals was performed with the Crystal Ball detector at BNL[2] [Sad04]. Crystal Ball is a multi photon spectrometer covering the full angular space. The SCX cross section was measured by detecting the two γ rays of the π^0 decay.

3.2 Transmission measurement

A pioneering measurement of the total SCX cross section by detecting the transmitted charged pions was made by Bugg et al. in 1971 [Bug71] using a liquid hydrogen target and a scintillation detector. A more recent transmission experiment with a solid CH_2- together with a C-target for background subtraction was undertaken by Friedman et al. [Fri93]. The basic idea of a transmission experiment is to use an incident charged pion beam of a known intensity I_0 and to measure the transmitted intensity $I = I_0 e^{-\alpha\sigma}$ (see fig. 3.1) of transmitted or scattered charged pions. The total cross section σ for the production of neutrals then follows from the well known target properties α which are specified in Section 4.4.1. On a hydrogen target a SCX reaction process results in outgoing neutral particles which are not detected by the detector and therefore

---

[1] TRIUMF = **TRI** **U**niversity **M**eson **F**actory

[2] BNL = **B**rookhaven **N**ational **L**aboratory

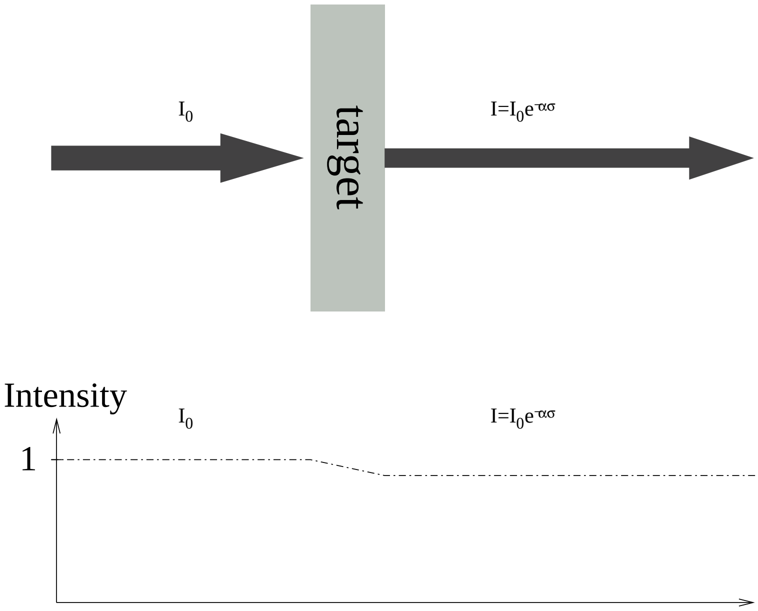

Figure 3.1: *Principle of a transmission measurement: I_0 is the intensity of the incident beam, $I = I_0 e^{-\alpha\sigma}$ is the intensity of the outgoing charged particles.*

the transmission is below unity. In all transmission experiments performed so far an arrangement of small scintillation counters has been used to define the incoming beam by a coincidence of counter signals. As a detector for the outgoing charged particles a collection of scintillation counters arranged so as to cover most of the 4π solid angle turned out to be suitable. In the experiment of Bugg et al. [Bug71] the covering of the full solid angle was difficult due to the use of a liquid hydrogen target. The experiment done by Friedman et al. [Fri93] at TRIUMF as well did not cover the full solid angle. The reason here was also due to the target handling. This experiment used various solid targets which had to be exchanged during the experiment. This was achieved by moving a target ladder through slots in the bottom and top scintillator. In addition the detector was not closed on the upstream side. Instead of backscattered pions the recoil protons were registered. The advantage of the use of solid targets in contrast to a liquid H_2 is that there is no aerosis, the target thickness is well known and the target handling and therefore the detector setup is easier to realize. The disadvantage of the solid targets is the need for statistics due to having to make two measurements one with the CH_2-target and the other for the C-target for background subtraction. Nowadays with the availability of high intensity pion beams and fast electronics this is no longer a serious problem.

3.3 Total cross section

The transmission T through a target is obtained by the ratio of the transmitted beam events to the incident beam events:

$$T = \frac{\text{number of transmitted events}}{\text{number of incident events}}$$

or expressed by intensities:

$$T = \frac{I_{transmitted}}{I_{incident}} = e^{-\alpha\sigma}$$

where the intensities I are corrected for the detection efficiency of the scintillation counters. The general expression for the transmission T through a target (tgt) is:

$$T_{\mathrm{tgt}} = e^{-\alpha_{\mathrm{tgt}}\sigma_{\mathrm{tgt}}},$$

where α_{tgt} is a target parameter containing the Avogadro number N_0, the atomic weight A and the areal density t, e. g. in units of g/cm^2

$$\alpha_{\mathrm{tgt}} = \frac{N_0 t}{A}.$$

For a measurement with no target inserted, the resulting transmission T_0 is naively expected to be unity. Due to scattering and losses in air and SCX and pion capture reactions in the last beam defining counter (def.) the resulting transmission is slightly smaller than one. Therefore the "empty" transmission also has to be measured for each energy. The target transmission T_{tgt} has to be corrected by the empty transmission T_0.

$$T_{\mathrm{tgt}} = T_0 e^{-\alpha_{\mathrm{tgt}}\sigma_{\mathrm{tgt}}}$$

The formal expression for the measured transmission is

$$T_{\mathrm{tgt}} = e^{-(\alpha_{\mathrm{tgt}}\sigma_{\mathrm{tgt}} + \alpha_{\mathrm{def.}}\sigma_{\mathrm{def.}} + \alpha_{\mathrm{air}}\sigma_{\mathrm{air}})}$$

or

$$log T_{tgt} = -(\alpha_{\mathrm{tgt}}\sigma_{\mathrm{tgt}} + \alpha_{\mathrm{def.}}\sigma_{\mathrm{def.}} + \alpha_{\mathrm{air}}\sigma_{\mathrm{air}}).$$

For the empty transmission T_0 we assume

$$T_0 = e^{-(\alpha_{\mathrm{def.}}\sigma_{\mathrm{def.}} + \alpha_{\mathrm{air}}\sigma_{\mathrm{air}})}$$

or

$$log T_0 = -(\alpha_{\mathrm{def.}}\sigma_{\mathrm{def.}} + \alpha_{\mathrm{air}}\sigma_{\mathrm{air}}).$$

For T_0 details are of little importance. The essential assumption is the additivity of the various matter components. Since

$$log T_{tgt} - log T_0 = -\alpha_{\mathrm{tgt}}\sigma_{\mathrm{tgt}}$$

the total cross section σ for the disappearance of charged particles can be written as

$$\sigma_{\mathrm{tgt}} = -\frac{1}{\alpha_{\mathrm{tgt}}} log \frac{T_0}{T_{\mathrm{tgt}}}.$$

The total cross section for hydrogen is then gained from the difference between the C and CH_2 target cross sections σ_{CH2} and σ_{C} as

$$\sigma_{\mathrm{H}} = \frac{1}{2}(\sigma_{\mathrm{CH2}} - \sigma_{\mathrm{C}}).$$

To illustrate the principle of obtaining the total SCX cross section from the measurements with solid targets results are shown in fig. 3.2 which will be discussed later (Chapter 10). Fig. 3.2 shows the measured total cross sections for events with outgoing neutrals for the C- (triangle up) and CH_2-target (triangle down) for π^- and π^+. The resulting total cross sections for hydrogen are presented by the circles.

The C and CH_2 cross sections which have to be subtracted are numbers similar in size and therefore the measurements require high statistics. Note that the π^- cross section reflect the underlying Δ-resonances and that the π^+p cross sections are zero as they must be with no open charge exchange channel.

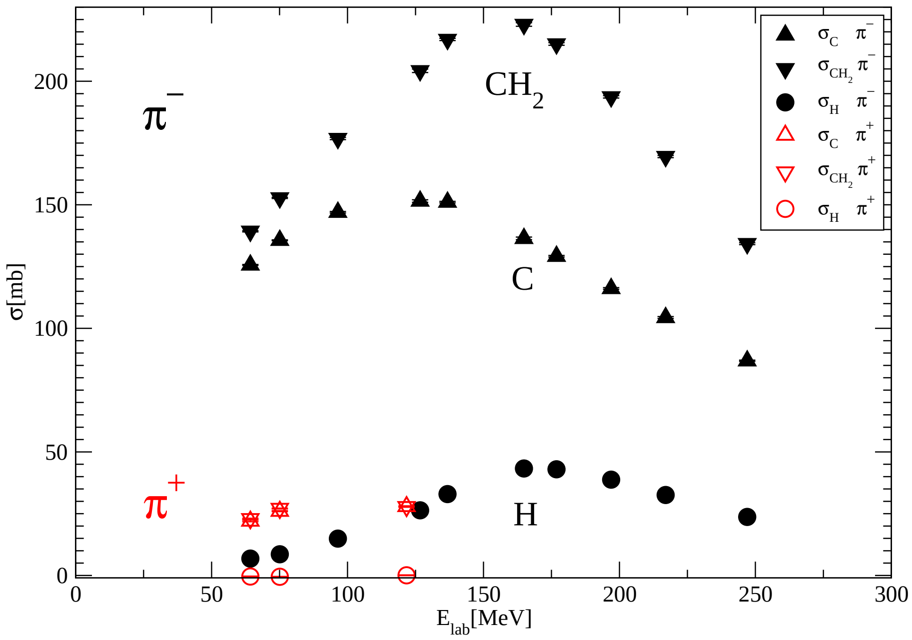

Figure 3.2: *Total cross sections for production of neutrals from the C- and CH_2- targets and the resulting H cross section for π^+ (red) and π^- (black).*

Chapter 4

Experimental setup

To carry out experiments with unstable pions ($\tau_\pi = 26$ ns) one has to use dedicated accelerator laboratories which provide charged pion beams. In general the pion beams are produced in nuclear reactions using an incident primary particle beam, normally a proton beam, hitting a production target. One of the world's largest meson factories is the **P**aul-**S**cherrer-**I**nstitut (PSI), located on the river Aare in Villigen, Switzerland. The experiment described in this work was performed at the PSI. In the following chapter the accelerator components and the 4π-detector are described.

4.1 The Paul Scherrer Institut (PSI)

The PSI is a national research institute which hosts different disciplines of basic science including solid state physics, materials sciences, elementary particle physics, life sciences, nuclear and non-nuclear energy research and energy-related ecology. For elementary particle physics the PSI operates a cyclotron which delivers a pulsed proton beam of 590 MeV with a frequency of 50.63 MHz. The accelerator facility of the PSI provides an excellent research environment for particle physics and was originally designed for the production of secondary muon and pion beams. Nowadays the facility concentrates more and more on experiments with thermal, cold and ultra cold neutrons to explore questions of solid-state physics and material properties.

Protons are accelerated up to 870 keV by a Cockcroft-Walton-accelerator before they are injected into a so called injector, a ring cyclotron, which increases the proton energy up to 72 MeV. Finally the protons pass the main cyclotron and leave it with 590 MeV to pass two production targets TM [1] (2 mm thickness) and TE [2] (40 mm thickness) consisting of a rotating cone of polycrystalline graphite. Hitting the production targets with an intensity of about 1.8 mA every 19.75 ns and a pulse width of ≈ 0.3 ns the proton beam bunches produce nuclear fragments, photons and pions. The charged particles, the pions and their decay products muons and electrons/positrons, are transported by secondary beam lines for use in the various experimental areas (see fig. 4.1). The secondary beam lines consist out of a collection of dipole magnets (particle momentum selection), quadrupole magnets (beam focusing) and various slits which are used to control the beam size, flux and momentum acceptance.

4.2 The beam lines πM1 and πE3

For this experiment two different pion channels were employed which transport pions from the two different production targets. The channel πM1, extracting pions from the TM target, was used for the high energy part of the measurement ($E_\pi = 55 - 250$ MeV). For pion energies from 38 to 76 MeV the beam line πE3 attached to the TE target was used.

---

[1] **m**ince=fr. thin

[2] **é**pais=fr. thick

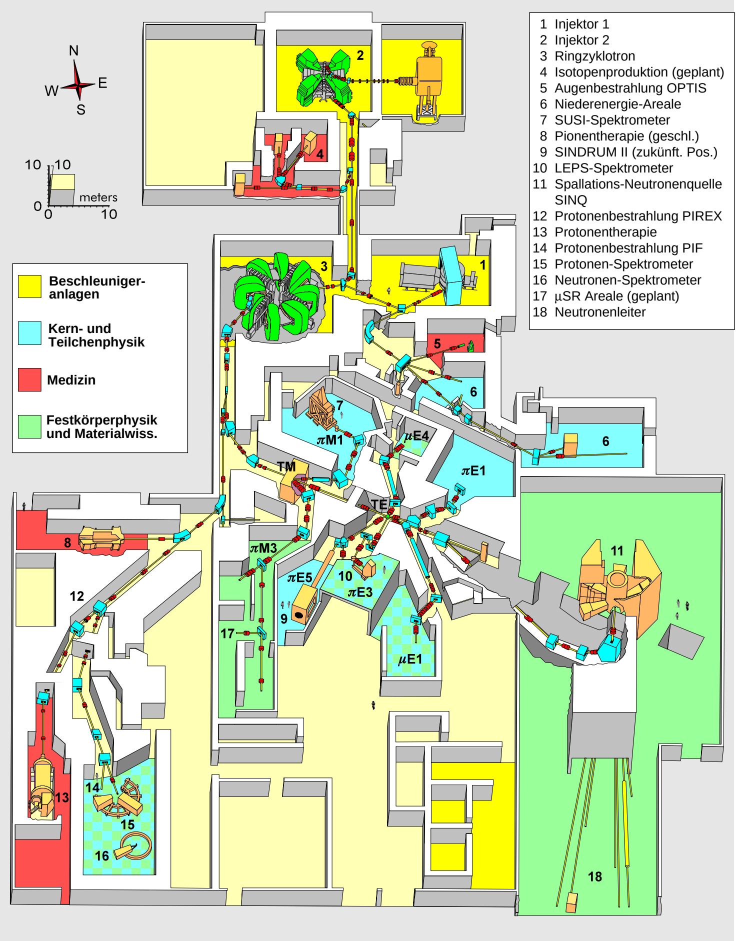

Figure 4.1: *Schematic top view of the PSI - experimental hall west. Injectors (1, 2) and ring cyclotron (3) accelerate protons to 590 MeV. At the production target TM, the pions for the channel πM1 are produced. The particles for the beam line πE3 are extracted at the target TE (source [PSI94]).*

4.2.1 πM1-channel

The πM1 beam line delivers pions in a momentum range of 100 to 500 MeV/c. It is a high resolution beam line connected to the target station TM in the direction of the target wheel orientation. Therefore the extracted beam width is horizontally equal to the thickness of the target of 2 mm. Consisting of 2 dipole and 9 quadrupole magnets the beam line provides a momentum resolution of better than 0.1 %. Fig. 4.2 shows the layout of the beam line. In table 4.1 the main characteristics of the beam line are listed. This beam line was used to measure

Table 4.1: *Characteristics of the πM1-beam line [PSIM1]*

Total path length	21 m
Momentum range	100 - 500 MeV/c
Solid angle	6 msr
Momentum acceptance (FWHM)	2.9 %
Momentum resolution	0.1 %
Dispersion at focal plane	7 cm/%
Spot size on target (FWHM)	15 mm horizontal 10 mm vertical
Angular divergence on target(FWHM)	35 mrad horizontal 75 mrad vertical

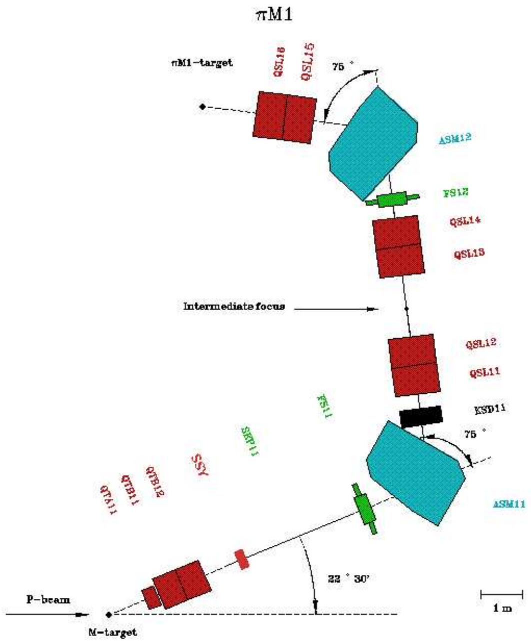

Figure 4.2: *Magnetic elements of the πM1 beam line [PSI94]*

the SCX reaction for pion kinetic energies from 60 to 250 MeV.

Beam line calibration

An electrostatic separator that was previously installed had been removed, such that the originally determined available beamline settings could not be considered as reliable. In order to tune the exact beam energy a new beam line calibration was required. It was performed by measuring the **T**ime **O**f **F**light (TOF) of protons of a specific momentum over a distance of 568.7 cm. Protons were used due to the fact that for a given adjusted momentum protons have a longer TOF, allowing for a more precise measurement. 250 MeV pions have a momentum of 363.71 MeV/c and need 20.32 ns for a distance of 5.69 m. 363.71 MeV/c protons pass a distance of 5.69 m in 52.49 ns. To minimize the energy loss of the protons in air an additional vacuum pipe was attached as an extension to the beam pipe. The end of the beam pipe was covered by a mylar foil of 190 μm thickness. First, a scintillator detector B0 (see setup 1 in fig. 4.3) with a thickness of 3 mm was inserted into the vacuum pipe which had a total length of 600 cm.

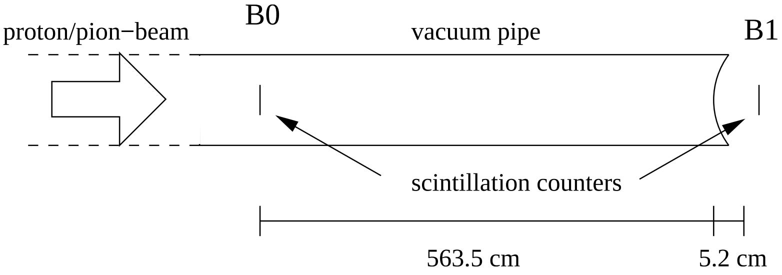

Figure 4.3: *Setup 1, beam line calibration πM1, the counter B0 is inserted in the vacuum pipe.*

In a second setup the position of detector B0 was outside of the vacuum pipe extension (see setup 2 in fig. 4.4) in front of B1. Fig. 4.6 shows the πM1 experimental area with the beamline calibration setup (left). The right hand fig. shows the assembly of the 4π-detector in use with the target located 213 cm away from the end of the channel. The length for the TOF path was

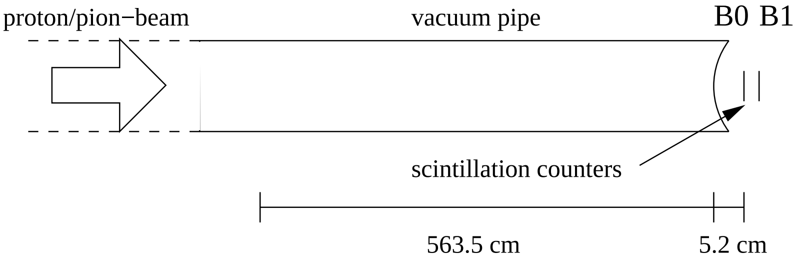

Figure 4.4: *Setup 2, beam line calibration πM1, the counter B0 is moved close to counter B1 at the end of the vacuum pipe.*

the distance between the position of B0 in setup 1 (fig. 4.3) and the position of B0 in setup 2 (fig. 4.4). For the proton time of flight measurement four time measurements were necessary which are described in following paragraph:

The data acquisition was gated by the coincidence between the detector B0, B1 and the so called *tcap*[3] signal of the accelerator. The *tcap* as well as each of the detectors B0 and B1 were connected to a channel of a **T**ime to **D**igital **C**onverter (TDC). A signal in detector B1 was the common start for the three TDCs (see fig. 4.5).

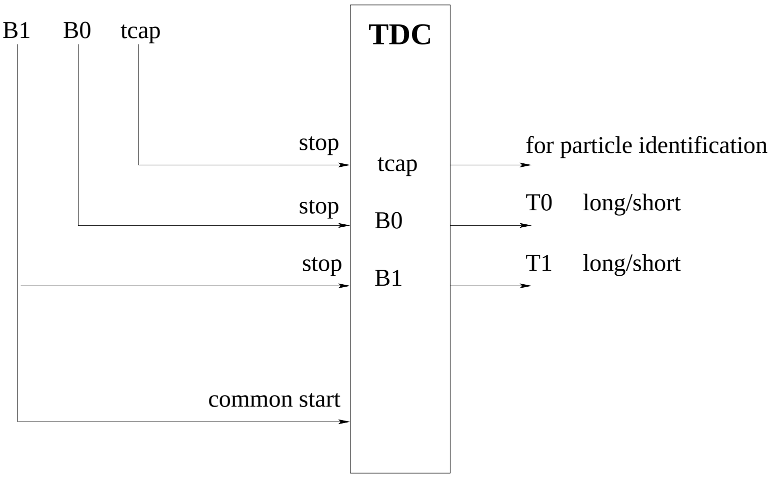

Figure 4.5: *Sketch of TDC connection for the beam line calibration:*

1: *The TDC of B1 was stopped by itself. For setup 1 the resulting time difference between start and stop is $T1_{short}$.*
2: *In setup 2 the corresponding time difference is $T1_{long}$.*
3: *The TDC of B0 was stopped by B0. In setup 1 the resulting time difference between B1 start and B0 stop is $T0_{short}$.*
4: *In setup 2 the corresponding time difference is $T0_{long}$.*

The particle type was selected by the time of flight measured from the *tcap* TDC spectrum. With the four TOF measurements the time of flight of the protons could be calculated without accounting for different signal delays due to different cable lengths and delays caused by the electronics of the data acquisition:

$$T_{protons} = |T1_{long} - T0_{long}| - |T1_{short} - T0_{short}|$$

To determine $T1_{long}, T0_{long}, T1_{short}, T0_{short}$ one must fit the peaks with a Gaussian function in the time of flight spectra of the counters B0 and B1. To assign a time to the fits the spectra

---

[3] 50 MHz pulse signal from the accelerator

have to be calibrated using the pulse structure of the accelerator. The peaks in the time of flight spectra caused by randoms originating from different beam bunches have a distance of 19.75 ns and can be used to calculate the time width of one channel of the TOF-spectra. For spectra and further calibration details see Appendix C. The dipole magnet ASM11 (see fig. 4.2) was responsible for the selection of the momentum. After tuning the chosen momentum ASM12 was used to optimize the beam rate. The energy calibration was done with a momentum setting of 363.71 MeV/c. For other desired momenta P the dipole magnet ASM11 was tuned according to

$$P = \frac{ASM11(P)}{ASM11(363.71\ \frac{\mathrm{MeV}}{c})} 363.71\ \frac{\mathrm{MeV}}{c}$$

The calibration was also repeated at 220 MeV and 180 MeV and confirmed the nominal beamline settings [Ped78] within an uncertainty of $2 - 3$ ‰ in the momentum.

Figure 4.6: *Experimental area of the πM1 beam line: With the 4π detector setup (right) and with the setup for the beam line calibration (left) where the detector was replaced by a 6 m vacuum extension pipe*

4.2.2 πE3-channel

Consisting of two dipole, nine quadrupole and 3 sextupole magnets, the πE3 beam line was originally designed to match the optical characteristics of the **L**ow **E**nergy **P**ion **S**pectrometer **LEPS**. The beam line images more than half of the target TE under an angle of 90°. This produces a larger beam spot in the experimental area of the πE3 channel than in the channel πM1. It is the only beam line with a vertical bending plane and as a result the experimental area is located 6 m above the floor of the experimental hall. The layout of the πE3 beam line is shown in fig. 4.7.

The beam line can be operated in two different modes. A high resolution *chromatic* mode was specially designed for the spectrometer LEPS. For the SCX measurements the beam line was operated in the *achromatic* mode which is optimized for high flux experiments with stopped pions or muons. When used in the *achromatic* mode the πE3 channel provides pions and muons in a momentum range of $10 - 250$ MeV/c with a momentum resolution of < 0.5 %. The most important properties of the channel are listed in table 4.2. Two pairs of slits, one in the horizonal and one in the vertical plane, allow the flux and momentum acceptance to be changed as required. The low energy data from $38 - 76$ MeV were taken with the πE3 channel. As there was a reliable beam line calibration available for exactly this channel configuration it was not necessary to repeat the calibration and the existing beam line settings from [Wie95] were used.

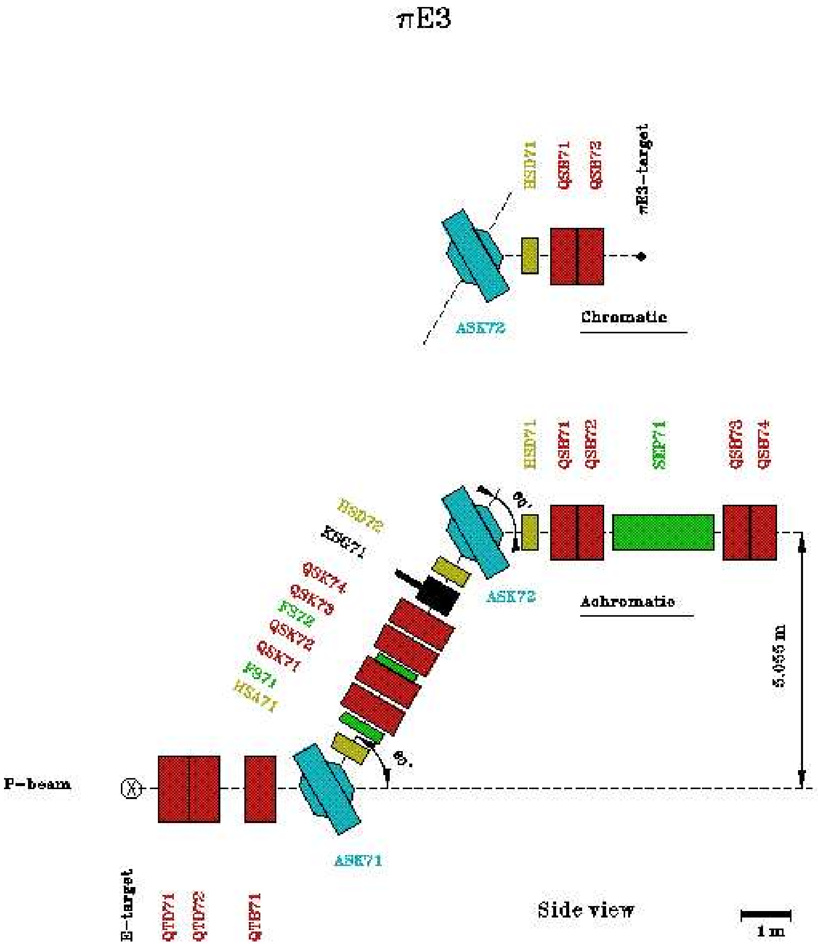

Figure 4.7: *πE3 beam line [PSI94].*

Table 4.2: *Characteristics of the πE3-beam line [PSIE3] (achromatic mode)*

Length	13 m
Solid angle	16 msr
Momentum acceptance (FWHM)	3.4 %
Momentum resolution (FWHM)	0.5 %
Spot size (FWHM)	15 mm horizontal 30 mm vertical
Divergence (FWHM)	80 mrad horizontal 20 mrad vertical
Surface muon polarization	95 %

4.3 Beam definition and beam defining counters

To measure a transmission, one needs to count the incident beam pions. Three scintillator counters (S1, S2, S3) made of EJ-200 plastic scintillator material manufactured by Eljen Technology (see Appendix E) were set up to define the incoming beam (see fig. 4.8).

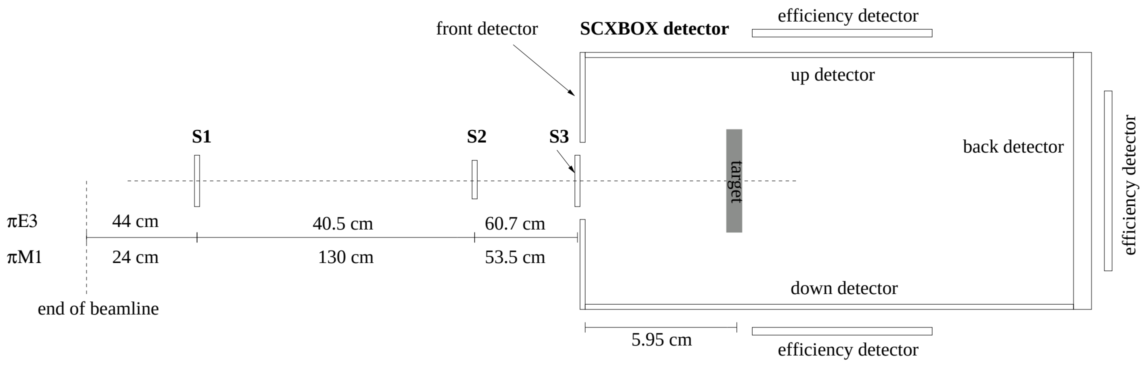

Figure 4.8: *Beam definition counter setup: S1, S2 and S3 are aligned with the help of a laser aiming at the target middle.*

S1 and S3 were made of 20 x 20 x 2 mm^3 scintillators. The dimension of the S2 scintillator was 15 x 15 x 2 mm^3. The beam defining counters were placed between the end of the beamline and the target. The beam defining counter (S3) which is the closest to the target is positioned 5.8 cm in front of the target in the opening of the box detector parallel to the up stream side of the 4π-detector ("front" detector). To be able to mount it close to the front detector the light guide of the S3 detector required a a special design (see fig. G.4 in Appendix G). In the πM1 beam line the S2 detector was positioned 53.5 cm (πE3: 60.7 cm) further upstream of the S3 counter, placed on the right side into the beam. The detector S1 was set up 130.0 cm (πE3: 40.7 cm) upstream of S2 in front of the end of the vacuum pipe. The distance to the mylar foil which was sealing the vacuum pipe was 24 cm (πE3: 44 cm). The beam profile of the low energy channel πE3 is wider and more divergent than the profile of the πM1 and therefore beam definition counters were set up closer together to get a reasonable trigger rate. The three defining counters were mounted on light guides manufactured out of Lucite with a width of 2.5 cm and a thickness of 5 mm (see Appendix G figs. G.3 and G.4). The light of the scintillators was transported by the dove tailed light guides to the photomultipliers (PM). The PMs were the model R6427 from the manufacturer Hamamatsu (see Appendix E) were used. For better reflection of the scintillator light the light guides and scintillators were packed in aluminum foil (thickness: 0.015 mm). The aluminum foil featured a hexagonal relief pattern to hold air between the foil and the scintillator to ensure the total reflection. Black plastic foil (thickness: 0.15 mm) in combination with black tape (thickness: 0.15 mm) was used to make the detectors light tight. The beam defining counters were arranged in different orientations to prevent particle scattering in air or in the S1 detector, passing S2 and S3 in the light guides, producing Cherenkov light and triggering this event as a valid beam event (see Chapter 4.7). The rough alignment of the beam definition counters was determined with a laser which was set up at the end of the beam line aimed at the center of the target (see fig. 4.8). Afterwards a beam rate optimization was made using remote controlled x-y scanner tables to scan for the highest beam rates.

4.4 Target properties and handling

4.4.1 Target properties

The realization of a true 4π-detector required a simpler target setup than for example the extensive implementation of a liquid H_2-target. The most suitable alternative was to use a solid target. A CH_2-target with well known properties and a C-target for background subtraction had been used in an earlier experiment at TRIUMF [Fri93]. These targets turned out to be suitable for use in our SCX experiment too. There were three different pairs of C- and CH_2-targets available. The target sets differed from each other in thickness. The different thicknesses of each C- and CH_2-target pair was chosen so that the energy loss of the pions in the CH_2-

and C-targets was the same. Due to this requirement and the fact that the different targets had different densities the CH_2-target used was thicker than the C-target. Table 4.3 shows the properties of the targets. All targets had a 35 x 40 mm area perpendicular to the pion beam.

Table 4.3: *Table of target properties*

Target	Area [cm^2]	Weight m [g][1]	Areal density t [mg/cm^2]	$1/\alpha$ [barn]
CH_2 thick	13.9864(17)	9.969(1)	712.76(11)	32.676(05)
CH_2 mid	13.9957(18)	6.088(1)	434.99(09)	53.542(12)
CH_2 thin	14.0341(45)	4.367(1)	311.17(12)	74.845(28)
C thick	14.0183(45)	11.801(1)	841.82(28)	23.690(08)
C mid	14.0175(73)	7.235(1)	516.14(28)	38.638(21)
C thin	13.9825(14)	5.188(1)	371.03(08)	53.749(12)

[1] buoyancy corrected

The target properties were precisely determined several times with a high precision scale (Company: Kern Model 434-33, accuracy 0.001 g). The areal density given in mg/cm^2 was calculated from the measured weight and area taking into account the buoyancy in air. The new target property measurements and the values obtained in the TRIUMF experiment in 1992 showed excellent agreement within the errors. The thickness of the targets was measured at 14 different points each with a micrometer gauge (accuracy 5 μm) and the resulting homogeneity was better than $2 \cdot 10^{-3}$. The quantity $1/\alpha$ was needed to calculate the single target cross sections and was directly obtained from the target parameters area and weight,

$$\alpha = \frac{N_0 t}{A}$$

with N_0 the Avogadro number, A the atomic weight of the target molecules and t the areal density of the target. To calculate the total cross section the stoichiometrical ratio between the carbon and the hydrogen in the CH_2-targets was needed. Several analyses were made resulting in a hydrogen to carbon ratio of 1.989 ± 0.015. Nevertheless a stoichiometrical ratio between the carbon and the hydrogen of 1:2 was assumed. The graphite was very clean reactor grade and activation and microprobe tests showed it to be much cleaner than the CH_2-target.

4.4.2 Target changer system

The use of the solid targets required several target changes for each measured energy: to prevent longtime drifts of the detectors or influences caused by external sources over longer time periods a repeated change between the CH_2- and C- and an empty target frame was required. An interchange between the targets during the measurement about every 30 minutes seemed reasonable to account for long time effects resulting from the detector setup. A manual change of the targets in the closed detector over a time period of several weeks would not have been practical and therefore an automatic remote controlled solution was developed. Each target had a specific target frame manufactured out of aluminum (see Appendix H.1 for detailed drawing). Two pairs of targets and an empty frame could be placed in fork like holders (see Appendix H.1) which were attached along an aluminum profile connected to a linear drive unit. Centered on the bottom scintillator ("down" detector) of the 4π-detector and 5.8 cm away from the upstream end of the down detector the counterpart (see Appendix H.1) of the target holder was attached on which the different target frames could be placed. The bottom detector itself was attached to a linear drive feed unit and could be lowered automatically. With a specific sequence of movements of the two linear drive units the target holder mounted in the 4π-detector could be removed and a new holder with a different target or an empty holder could be placed instead. Figs. 4.9 and 4.10 show the target change setup while the 4π-detector is open. For a more detailed description of the target change see [Bau03]. The two linear drives were driven by a

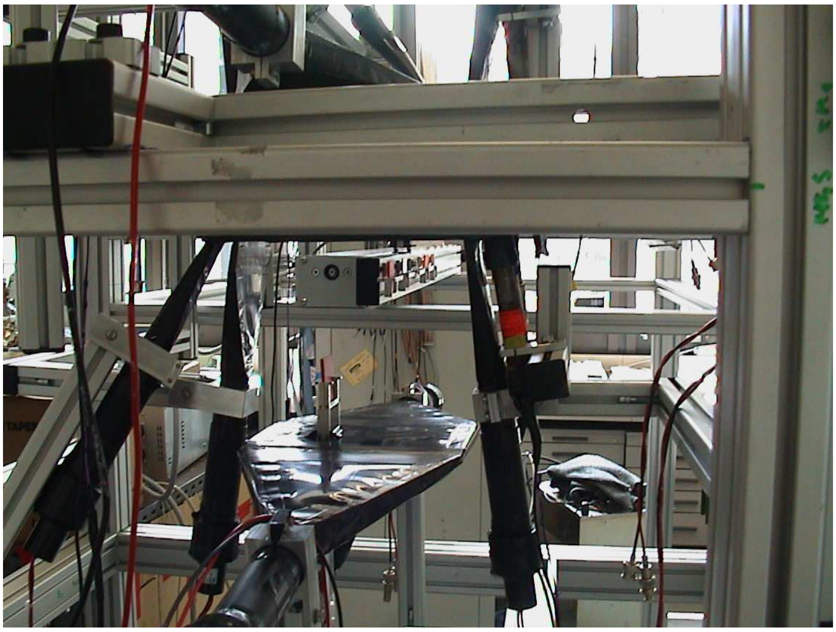

Figure 4.9: *In order to change the a target in the 4π scintillator box, the bottom detector is lowered and the target mounted on the scintillator is changed automatically.*

Figure 4.10: *Insertion of the thick CH_2-target during a measurement*

motor controller. This controller was connected to the computer running the data acquisition through a RS323 serial link. The exchange of the targets was controlled by the data acquisition software. This simple target changing setup proved to be very reliable. Nevertheless the whole changing process was secured by a number of mechanical end-switches. This safety feature was never triggered.

4.5 The 4π scintillator box

To carry out the transmission measurement a new detector sensitive to charged particles was built. For the construction of the detector it was very important to cover as much of the 4π solid angle as possible. All the scintillator parts of the detector were made out of EJ-200 scintillator produced by Eljen Technology (for specifications see Appendix E). The center of the detector consisted of six scintillator plates, five with a thickness of 2 mm and one with a thickness of 7 mm. For a schematic drawing see fig. 4.11. To cover the full 4π solid angle the six different scintillator parts of the detector were arranged in the shape of a rectangular box of 10 x 10 x 19 cm^3. Two scintillators with a length of 20 cm and a width of 10 cm formed the side of the detector and therefore were called the “left” (downstream viewing direction) and “right” side counters. At each end of the scintillators light guides, which consisted of Lucite with a

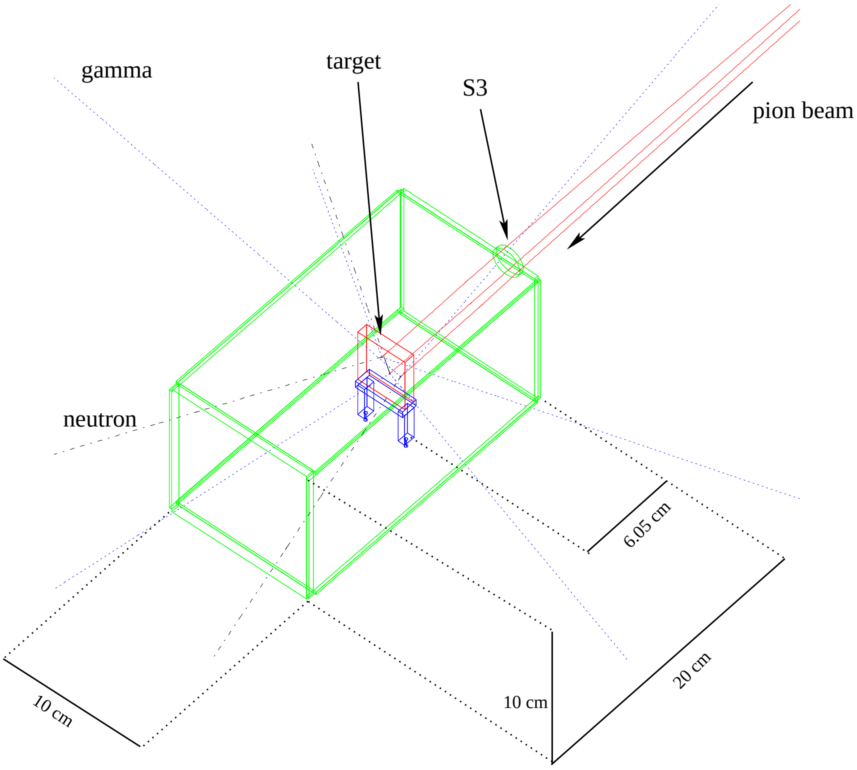

Figure 4.11: *GEANT3 plot of the scintillating part of the detector. The picture also shows some simulated SCX events. The incoming pions are represented by the red full lines, the neutrons (dashed dotted) and gammas (dotted) are leaving the target.*

dove tail end of 10 cm width and a thickness of 6 mm, were attached to the scintillators (for a detailed component drawings see Appendix G) to direct the light to the PMs. The upper and lower part of the detector consisted of two scintillators with a length of 19 cm and and a width of 10.4 cm. These were called the “up” and “down” detectors. On both sides light guides with a front width of 19 cm were attached. The light guides and scintillators of the left and right counters were glued together at an angle of 5° to the plane of the scintillators which made it possible to arrange the single detector parts without obstructing each other. A total view of the detector including light guides and photomultipliers is shown in the GEANT3 plot in fig. 4.12.

To cover the full 4π solid angle up- and downstream (“front” and “back” counter) counters were set up. The downstream detector was the most important part because more than 99 % of the transmitted or scattered pions hit this scintillator. For a better efficiency the back counter had a thickness of 7 mm, a width of 10 cm and a height of 10.4 cm. The front detector consisted out of a scintillator with a height and width of 10.4 cm and 10 cm respectively and a thickness of 2 mm. The incident pion beam had to pass the front counter, therefore the scintillator featured a hole of 3 x 3 cm^2 through which the beam could enter the detector. Light guides were connected on the up and down side of the detector (see fig. 4.12). For an easier arrangement of the 4π-detector components the light guides of all detectors were not glued parallel to the scintillator but with an angle of 8° for the front and back detector and 5° for the other detector parts (see figs. 4.13). The larger angle for the front and back detector was necessary to guarantee an easy and safe lowering of the down counter for the required target changes (see Section 4.4.2). For a quick survey of the scintillator dimensions see table 4.4.

The gap in the front counter covers a solid angle of $\Delta\Omega = 0.254$ sr which is 2 % of 4π (see fig. 4.14). The differential cross section for elastic π^- scattering on hydrogen is suppressed for larger scattering angles. For the lowest measured energy the pion hits the target with 40.3 MeV and the cross section for elastic scattering into the solid angle of the gap is approximately

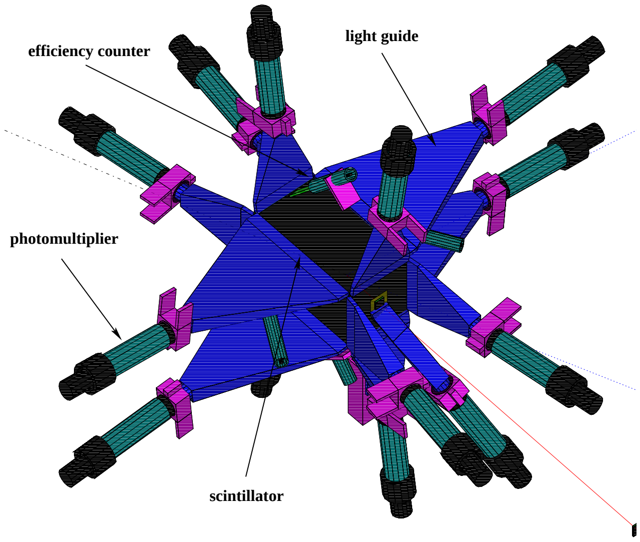

Figure 4.12: *GEANT3 plot of the heart of the box detector, showing the scintillator plates (black) light guides (blue), photomultipliers (dark green tubes), efficiency counters (seen above the top counter and partially seen on the side counters) and the last beam defining counter (in front of the upstream detector).*

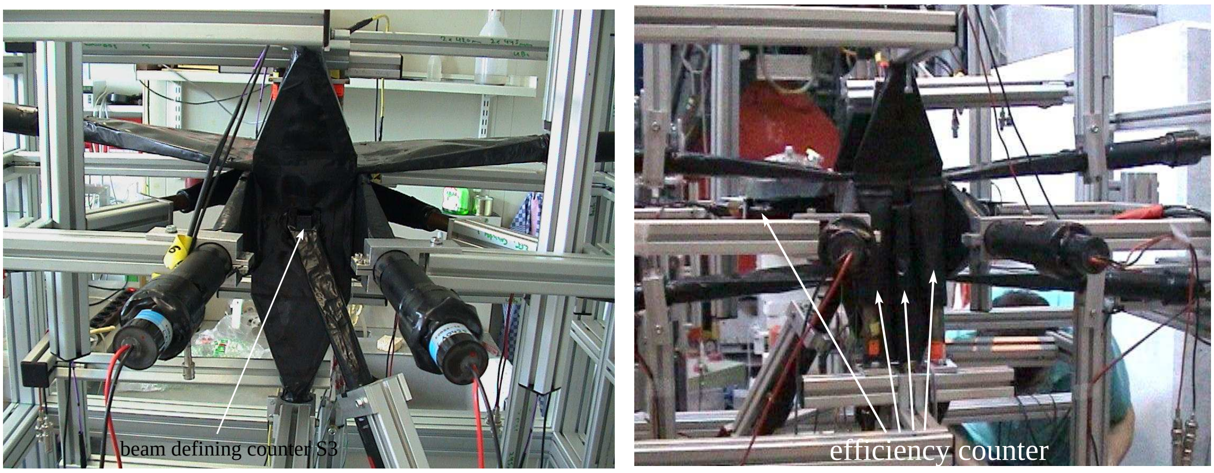

Figure 4.13: *Front view of the 4π-detector, with the last beam defining counter positioned in the front counter opening (left) and from the back side with the three efficiency counters of the down stream counter.*

Table 4.4: *Dimension of the six different 4π-detector scintillators*

detector scintillator	length [mm]	width [mm]	thickness [mm]
front	104	100	2
back	104	100	7
up	190	104	2
down	190	104	2
left	200	100	2
right	200	100	2

$\Delta\Omega \cdot d\sigma_{elastic}/d\Omega = 0.254$ sr $\cdot$ 0.022 mb/sr = 0.0056 mb. Compared to the expected total SCX cross section of 5.793 mb (SAID FA02 prediction) this loss is negligible and was considered irrelevant. For higher energies the loss is even smaller. The resulting recoil protons from back scattered 45 MeV pions already leave the target (thick CH_2-target) and are detected in the back

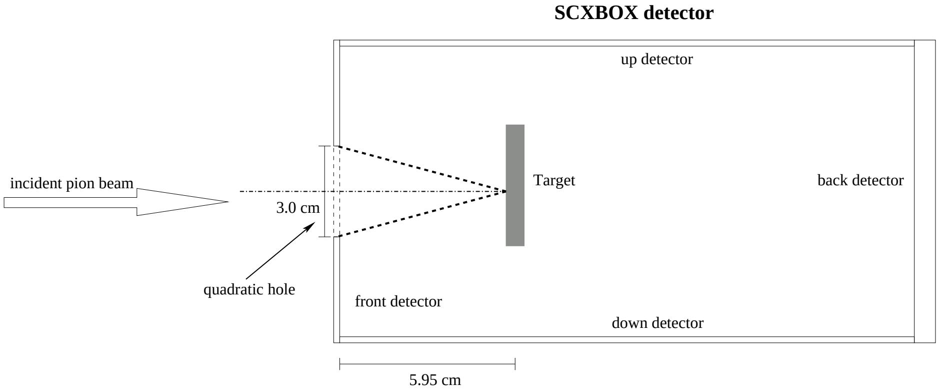

Figure 4.14: *Side view cut of the SCX detector*

counter by depositing at least 2 MeV. Therefore for a detected recoil proton the back scattered pion is counted as transmitted beam event and there is effectively no loss of events. For elastic π^+p back scattering the differential cross section is explicitly larger. The cross section for pions which pass undetected through the box opening is slightly less than 0.3 mb for an incident π^+ energy of $T_\pi = 40.3$ MeV. Recoil protons which emerge from scattering in the first 0.9 mm of the thick CH_2-target (thickness: 7.63 mm) get stopped in the target. Protons from scattering processes which occur deeper in the target already leave the target and deposit enough energy in the back counter to count this beam event as a transmitted event. If one assumes a homogeneous distribution of the pion scattering points in the target, only about 12 % of the back scattered π^+ are lost. Hence the cross section for a non detected π^+ is about 0.036 mb, which can also be neglected.

The photomultipliers HM R6427 (see Appendix E) which detect the scintillation light were physically connected to the light guides with clamps fixed to an aluminum frame to give the detector parts stability. A cage like arrangement of aluminum profiles from a commercial building kit system [ITM05] was used to set up and adjust the six detector parts. For the optical connection between PM and light guide an optical grease was spread on the connecting areas. The light guides and scintillators were wrapped in aluminum foil which enhances the reflection of the light to the PM tubes (see Section 4.3). To make the detector parts light tight we used black plastic foil which was fixed with black tape.

4.6 Efficiency counters

Depending on the target and the pion energy only between 0.7 and 1.1 % of the incident pions undergo the charge exchange reaction. In order to determine this with an accuracy of 10^{-2}, the knowledge of the efficiency of the detector and its associated electronics is very important. For each scintillator the efficiency was measured online. To determine this a second small scintillator counter (70 mm x 15 mm x 3 mm) was placed behind each box counter. The efficiency counters were placed such that a triggered beam event which hit the efficiency counter always had to pass the corresponding detector counters (see fig. 4.12 and fig. 4.13). There was one efficiency counter for each detector part, except for the back counter which was monitored by three efficiency counters and the front detector which was not monitored by an efficiency counter. For the extraction of the efficiencies from the counter spectra see Section 7.1.

4.7 Trigger

The SCX experiment used a very simple trigger to select if an event was recorded to disc (and tape) or rejected. Later on in the analysis the thresholds and further trigger conditions could be applied and changed in software. The only trigger condition used, required hits in the three beam defining counters S1-S3 together with the *tcap* signal. The output signals from the beam defining counters were directed using a linear fan in fan out module[4] into a quad discriminator unit[5] and a coincidence unit[6] (see fig. 4.15). The output of this coincidence unit was connected to a second coincidence unit[7] and together with the signal for a waiting Charge to **D**igital **C**onverter (QDC), TDC and **F**lash **A**nalog to **D**igital **C**onverter (FADC) readout (data acquisition ready) this unit gave the trigger for a valid beam event (see fig. 4.15). For a more detailed trigger connection diagram see Appendix D.

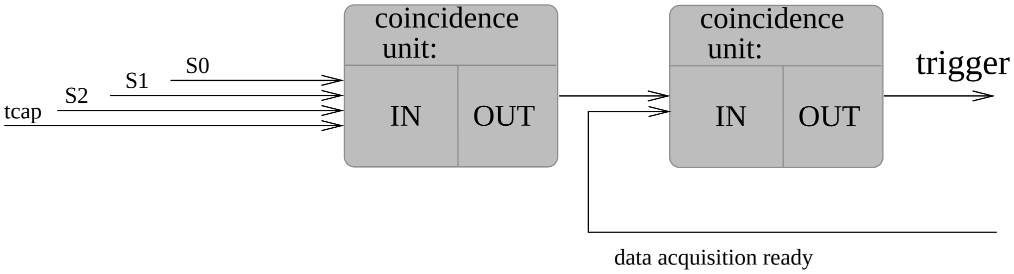

Figure 4.15: *Basic trigger setup: A valid event is recorded for a coincidence of the three counters S0, S1, S2 and the tcap.*

When the trigger started the data readout, it generated a veto signal which blocked the trigger input for following events until the data conversion was finished (8 μs). Every twenty events the QDC, TDC and FADC modules were transmitting buffered events to the front end computer. For the trigger no specific time of flight information was used, therefore coincidences caused by muons, electrons and pions were recorded. For high trigger rates at some energies an electron veto (*eveto*) was switched on to reduce the amount of recorded data pertaining to electron scattering. With the electron veto, the data acquisition electronic rejected coincidences which had the flight time of electrons.

4.8 Electronics and data acquisition

The signals of each of the 22 photomultipliers (3 beam defining counters, 12 photomultipliers for the main box detector, and 7 efficiency counters) were recorded, using the data acquisition electronic standards VME[8] and CAMAC[9]. Fig. 4.16 shows the setup of the signal processing beginning with the incoming 22 analog PM signals and the *tcap* signal (S0-S22) up to the read out of the VME through the frontend computer. The readout of the connected 32 channel QDC[10] (accumulating gate 50 ns) and 32 channel TDC[11] (accumulation period 156 ns) VME modules was performed by a PC-style[12] front end computer using the MIDAS[13] data acquisition program running under the operating system Windows NT 4.0. In addition the front and back detectors were connected to a $1-4$ channel Flash-ADC[14] (accumulation period 128 ns) which stored (for some selected runs) the signals with a sample rate of 250 MHz during a time interval of 128 ns for each triggered event. In addition the event rates of each detector, the trigger

---

[4] LeCroy 428F

[5] LeCroy 821

[6] FC 104

[7] LeCroy 465

[8] **V**ersa **M**odule **E**urope

[9] **C**omputer **A**utomated **M**easurement **A**nd **C**ontrol, see [Leo94]

[10] VME Caen V792

[11] VME Caen 775

[12] πM1: 266 MHz Pentium II processor, πE3: 1.3 GHz Athlon processor

[13] **M**aximum **I**ntegrated **D**ata **A**cquisition **S**ystem Version 1.8.1 [MID01]

[14] VME Wiener 7515

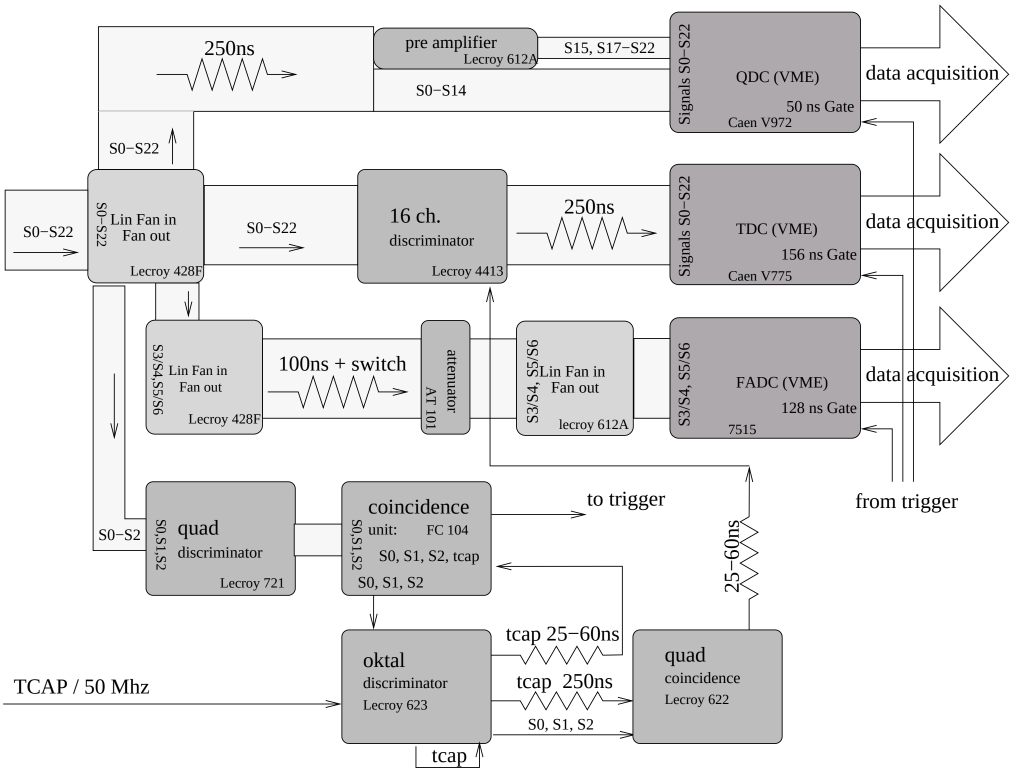

Figure 4.16: *Block diagram of the data acquisition setup of the 23 incoming analog signal lines (22 photomultiplier signals and the tcap) referred to as S0-S22.*

and LAM's[15] were counted by scalers which were read out every 10 seconds. The front end computer read out twenty buffered events together. With this technique the dead time of the data acquisition was reduced. But note that the deadtime affected only the statistics of the run, not the resulting cross sections. The data were transmitted to the main data acquisition computer through a fast Ethernet connection. The PC-style[16] data acquisition computer was running the operating system SuSE Linux Version 7.3. The data acquisition program MIDAS received the data and stored the πM1 data on DLT-Tape[17]. A backup of the data was stored on CD-R[18]. The data of the πE3 beam time were stored on disc (RAID[19] array with 1.2 TB capacity) and the backup was stored on DLT-Tape. A running MIDAS-analyzer performed a raw partial online analysis of the received data.

The software package MIDAS consists out of fully independent network capable program modules for the various tasks such as data storage (mlogger), the frontend (frontend) for the VME data read out and a server module (mserver) connecting the various components to the shared data base ODB[20] (odbedit). Out of many other modules (mhttp (MIDAS web server), mstat (status display), webpaw (PAW web/midas sever), mlxspeaker (speech synthesizer)) the analyzer (analyzer) has to be emphasized. The online analyzer provides a simple calibration of a fraction[21] of the obtained data and an extraction of first results output in the HBOOK-Format [CERN].

For each event the QDC, TDC and FADC information was stored. The data acquisition system was capable of recording up to 20000 events/s with a dead time of ≈ 50 %. The typical event rate was about $5000 - 8000$ events/s with a data flow of $1 - 1.5$ MB/s. Every 2.6 million

---

[15] **L**ook **A**t **M**e: Read out request of the trigger electronic

[16] double Athlon 1.2 GHz processor system

[17] **D**igital **L**inear **T**ape 40/80

[18] **C**ompact **D**isc **R**ecordable

[19] **R**edundant **A**rray of **I**nexpensive **D**isks

[20] **O**nline **D**ata **B**ase

[21] depending on the beam rate and the CPU speed

events the data acquisition was stopped to close the file the events were stored in. Almost 4000 files of that type were written for the whole experiment, giving a total of 3.5 TB of data.

Chapter 5

Measurements

5.1 Taken data

Table 5.1 shows a summary of runs including the measured energies, channel polarities and targets used. In the summer of 2001 the πM1 beam line was used to measure the cross section for pion lab energies from 55 to 250 MeV. The data for the energies from 38 to 76 MeV were taken in the summer of 2002 using the πE3 beam line. The role of the measurements with positively

No.	Channel	Channel polarity	Channel Energy [MeV]	Mid target energy [MeV]	Targets
1	πE3	$-$	43.69	38.92	C, CH_2 thick
2	πE3	$+$	43.69	38.92	C, CH_2 thick
3	πE3	$-$	43.69	39.48	C, CH_2 mid
4	πE3	$+$	43.69	39.48	C, CH_2 mid
5	πE3	$-$	43.69	39.72	C, CH_2 thin
6	πE3	$-$	47.50	42.99	C, CH_2 thick
7	πE3	$-$	51.40	47.10	C, CH_2 thick
8	πE3	$-$	51.40	47.61	C, CH_2 mid
9	πE3	$-$	51.40	47.82	C, CH_2 thin
10	πM1	$-$	60.00	55.55	C, CH_2 thick
11	πE3	$-$	68.00	64.27	C, CH_2 thick
12	πE3	$+$	68.00	64.27	C, CH_2 thick
13[1]	πM1	$-$	70.00	65.88	C, CH_2 thick
14	πM1	$-$	70.00	66.31	C, CH_2 mid
15	πE3	$-$	78.60	75.09	C, CH_2 thick
16	πE3	$+$	78.60	75.09	C, CH_2 thick
17[1]	πM1	$-$	80.00	76.10	C, CH_2 thick
18	πM1	$-$	100.00	96.47	C, CH_2 thick
19	πM1	$-$	110.00	106.54	C, CH_2 thick
20	πM1	$-$	120.00	116.62	C, CH_2 thick
21[1]	πM1	$-$	130.00	126.70	C, CH_2 thick
22	πM1	$+$	130.00	126.70	C, CH_2 thick
23	πM1	$-$	140.00	136.77	C, CH_2 thick
24	πM1	$-$	168.00	164.89	C, CH_2 thick
25	πM1	$-$	168.00	165.22	C, CH_2 mid
26	πM1	$-$	180.00	176.86	C, CH_2 thick
27	πM1	$-$	200.00	196.96	C, CH_2 thick
28	πM1	$-$	220.00	216.99	C, CH_2 thick
29	πM1	$-$	220.00	217.29	C, CH_2 mid
30	πM1	$-$	250.00	247.00	C, CH_2 thick

Table 5.1: *Parameters of completed runs*

---

[1] Run subdivided into runs with different beam rates

charged pions as an important test of the measuring method will be discussed in Section 9.1. In addition to these high statistics measurements a quick energy scan down to 15 MeV was performed. Besides the listed π^+ tests various other tests with different targets, such as $CH_{1.1}$ and measurements with different target thicknesses were performed. The main motivation for these tests was to determine possible effects on the results at low energies from the use of the C- and CH_2-targets (see Chapter 9). The high statistics data sets consisted typically of runs with 2.6 million triggered, recorded beam events or runs with 5 million recorded events if the FADC was not used. This resulted in a typical run time of 5 to 9 minutes depending on the trigger rate. For each target (C, CH_2, and empty) a set of 5 such runs was taken before it was changed to the next target. This interval length was short enough to prevent long time drifts in the detector setup and photomultiplier tubes affecting the measurements. The trigger rate varied between 3000 events/s for the low energies and 12000 events/s for the maximm of the Δ-resonance. The overall amount of taken data added up to 3.5 TB stored on disc and magnetic DLT IV tapes with a capacity of 80 GB.

Chapter 6

Data analysis

The purpose of the offline data analysis is to extract the total SCX cross section from the stored raw data. The first step is to determine incident pion events and to extract the efficiency of the detectors. Then this chapter describes how the incident and transmitted pions were identified and the total SCX cross section was extracted.

6.1 Data sets and format

The raw data were stored in a format called MIDAS-format (for more details see [MID01]). The information for each event is stored in several banks. The analysis software extracts the zipped data, accumulates the events and produces histogram and *ntuple*[1] output files which can be read and presented by a program package for histogramming and graphical representation called PAW[2] [PAW].

6.2 Analyzing programs

For the analysis of the data the programming language C was used. The offline analysis program (analyzer) is a further development of the online analyzer that was used and it produced histograms and *ntuple* files. The analyzer read the MIDAS format, calibrated and adjusted the pedestals, applied various relations and cuts in the spectra and wrote *ntuple* files and histograms.

6.3 Calibration of raw data — pedestal

The first step of the analysis was to calibrate the spectra. For each of the 22 photomultipliers a QDC and a TDC spectrum was recorded. For parts of the measurements an additional FADC spectrum of one of the two photomultipliers from the front and back scintillators was stored. We emphasize that a detected event required a non-zero entry within a gate period of 50 ns (see fig. 7.1) in one of the box scintillators. If the QDC received no signal during a gate period of 50 ns, which is defined by the trigger, the modules still delivered a non zero value which is called the pedestal. Shifting the pedestal to the same predefined specific channel (channel 95) for all the photomultipliers was the initial step of the analysis. The six box scintillators were read out by two photomultipliers each. The two QDC spectra obtained (as an example see fig. 6.1), had to be calibrated to the same pedestal and energy loss per QDC channel. Then the geometric mean of the two QDCs was determined (see fig. 6.1) by histogramming the geometric mean event by event. By comparing the calibrated spectra of the two PMs we found that 99.997 % of the detected events in the back counter and 100 % of those detected in the side counters were recorded in both PMs. Hence the light collection efficiency of the detectors was excellent.

---

[1] Ntuple: a data-type used to store data, a compact way to store event information, in table like way, each event gives a row and the variables of each event are the columns

[2] **P**hysics **A**nalysis **W**orkstation

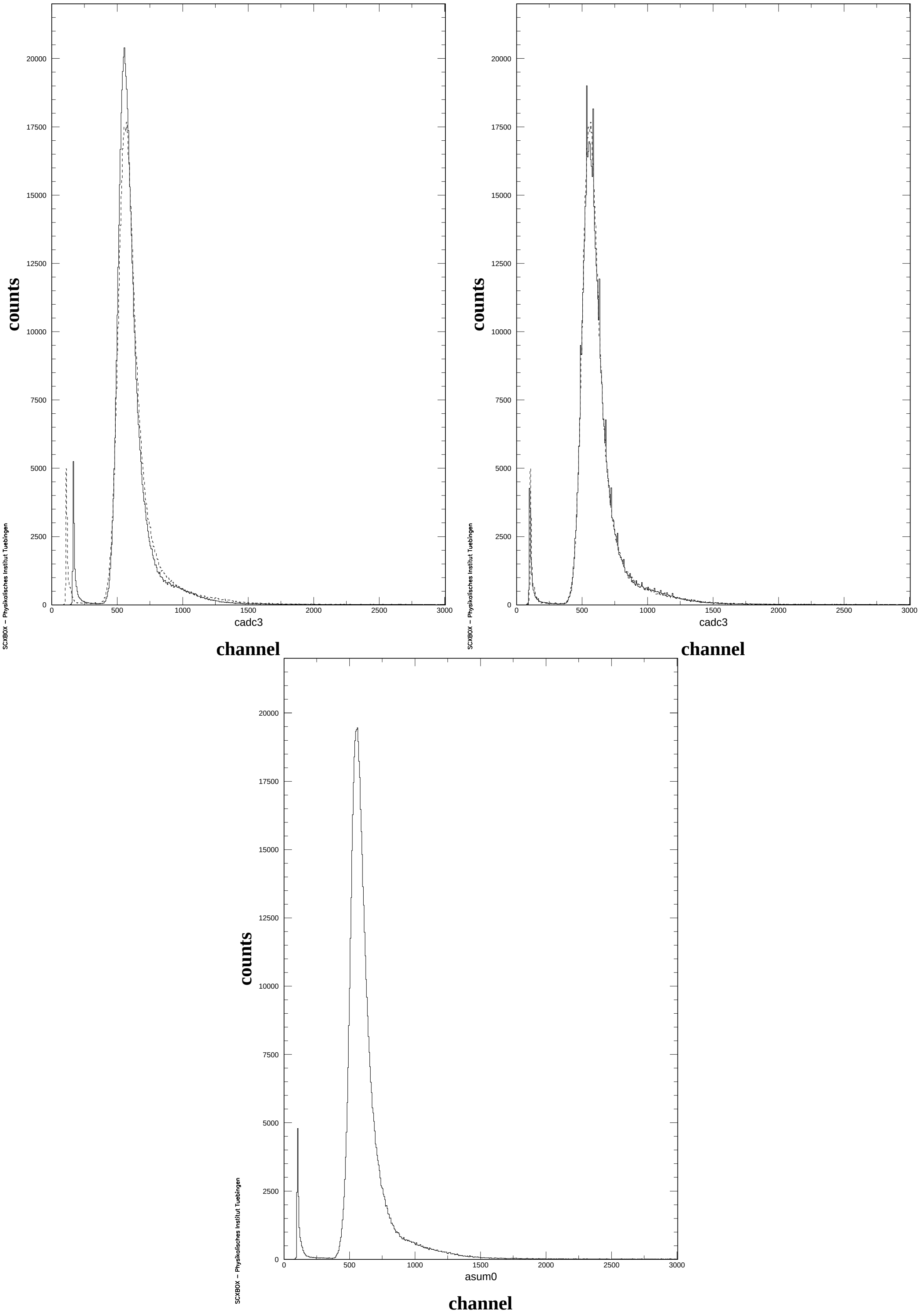

Figure 6.1: *Energy loss spectra of the back counter*
Top left: Uncalibrated spectra of each of the two PMs
Top right: Nearly identical spectra after calibration
Bottom: Histogram of the geometric mean of the calibrated signals

For the time measurement in the TDC spectra it was convenient to move the zero point (offset) to the same location in the spectra for all detector channels. The difference in the zero point arose from different cable length and signal travel times for the different channels. If the TDC received no signal during the open gate period, which was 156 ns for the TDCs, the overflow channel of the spectrum was filled with an entry.

6.4 Definition of incoming beam events

The next step was to select the valid incoming beam events. The trigger condition only returned valid events if there was a coincidence between an accelerator beam bunch (*tcap*) and a hit in all three beam defining counters.

TOF

The TDC spectrum of the last beam defining counter was started by a hit in the counter (S3) and stopped by the *tcap* signal. The resulting TDC spectrum (see fig. 6.2) shows the difference in the TOF for the electrons, muons and pions.

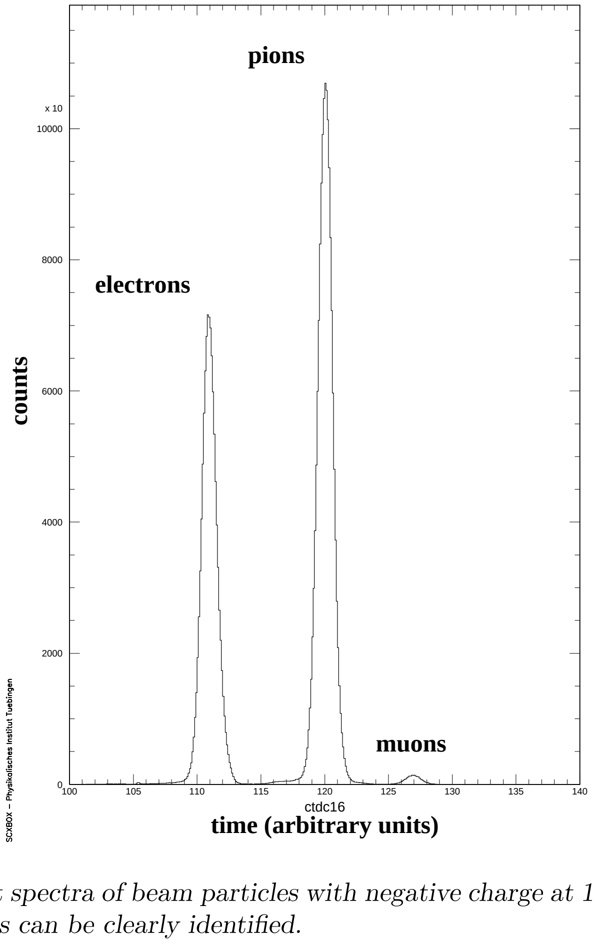

Figure 6.2: *Time of flight spectra of beam particles with negative charge at 130 MeV, negative polarity: The different particle types can be clearly identified.*

Using this TOF information, a cut on the resulting TOF spectra was applied to select a specific particle type. In the case of the spectrum shown in fig. 6.2 a cut was applied from channel 118 to 122 to select the pions. Note, that an accidental removal of pion events due to a narrow cut will only reduce the statistics of the measurement, but does not affect the resulting cross sections otherwise.

Beam definition counters

Cuts in the QDC spectra of the three beam defining counters were used (see fig. 6.4), to cut off the Landau tail[3] and to define particles within a specific energy distribution. Due to the geometric alignment a particle hitting all three beam defining counters will always hit the target in the box except when the beam particle was scattered off the S3 beam defining counter. Therefore, an incident particle fulfilling the prober TOF and energy loss requirement in the defining counters was treated as an incident pion hitting the target. Similarly to the TOF spectrum a narrow cut will only affect the statistics and not the resulting cross sections.

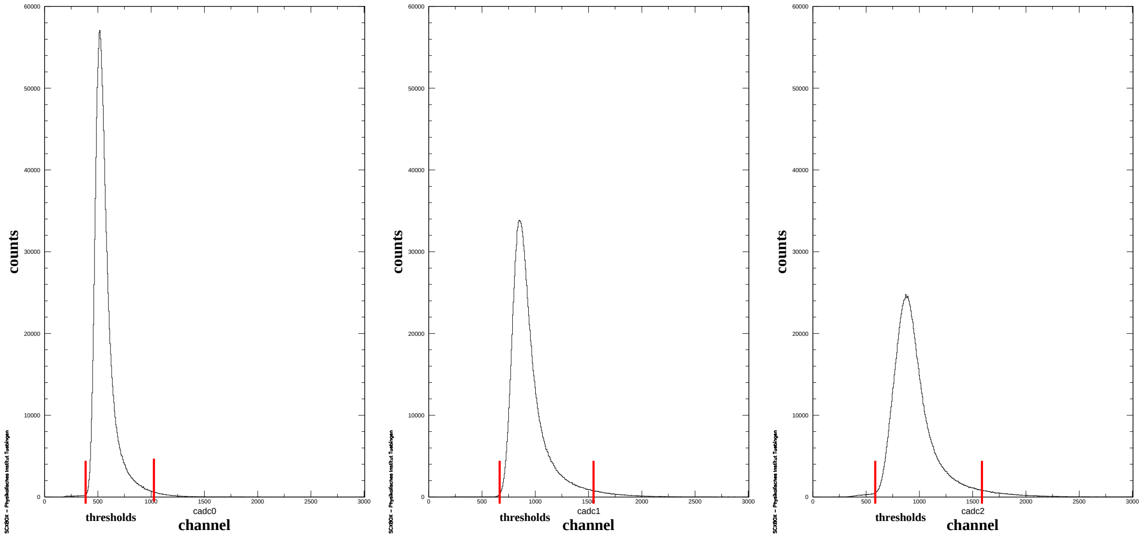

Figure 6.3: *Energy loss spectra in the three beam defining counters S1, S2, and S3 under the conditions of the TOF for pions in S3 and a coincidence of the three counters. The solid bars indicate the thresholds for a valid beam event.*

6.5 Identification of events with transmitted particles

To identify the detected scattered charged particles cuts in the spectra of the box counters have to be applied. There are six detectors which have to be evaluated.

Back detector: About $97-98$ % of the scattered pions are scattered in the forward direction and are detected by the back detector. Also back scattered pions transfer enough energy (for energies larger than $T_\pi = 45$ MeV) to the recoil proton that these protons can leave the target and hit the back detector, therefore accurate event registration in this counter is very important. The efficiency of this detector was measured online with three different efficiency counters. Furthermore to achieve a high efficiency the detector thickness was 7 mm. To identify the scattered events and recoil protons the minimum between the pedestal and the elastic scattering peak in the energy loss spectra was fitted by using a combination of a Lorentzian and an offset. Fig. 6.4 shows such an energy loss spectrum in the back counter consisting of pion and recoil proton events.

Side detectors: All detectors other than the back detector will be called “side detectors” Depending on the energy about 1 % of the scattered pions leave the box detector by passing through one of the five side counters. To count the scattered pions, cuts in the spectra of these five side detectors have to be applied. A typical spectrum of a side detector is shown in fig. 6.5 (left hand side). There is no peak of elastic scattered events visible. The elastic scattering peak

---

[3] The mean value of the total energy loss is given from the Bethe-Bloch formula. The energy loss distribution is given by the Landau distribution. The long Landau tail towards high energies is a result of the large fluctuations in high energy ionizations

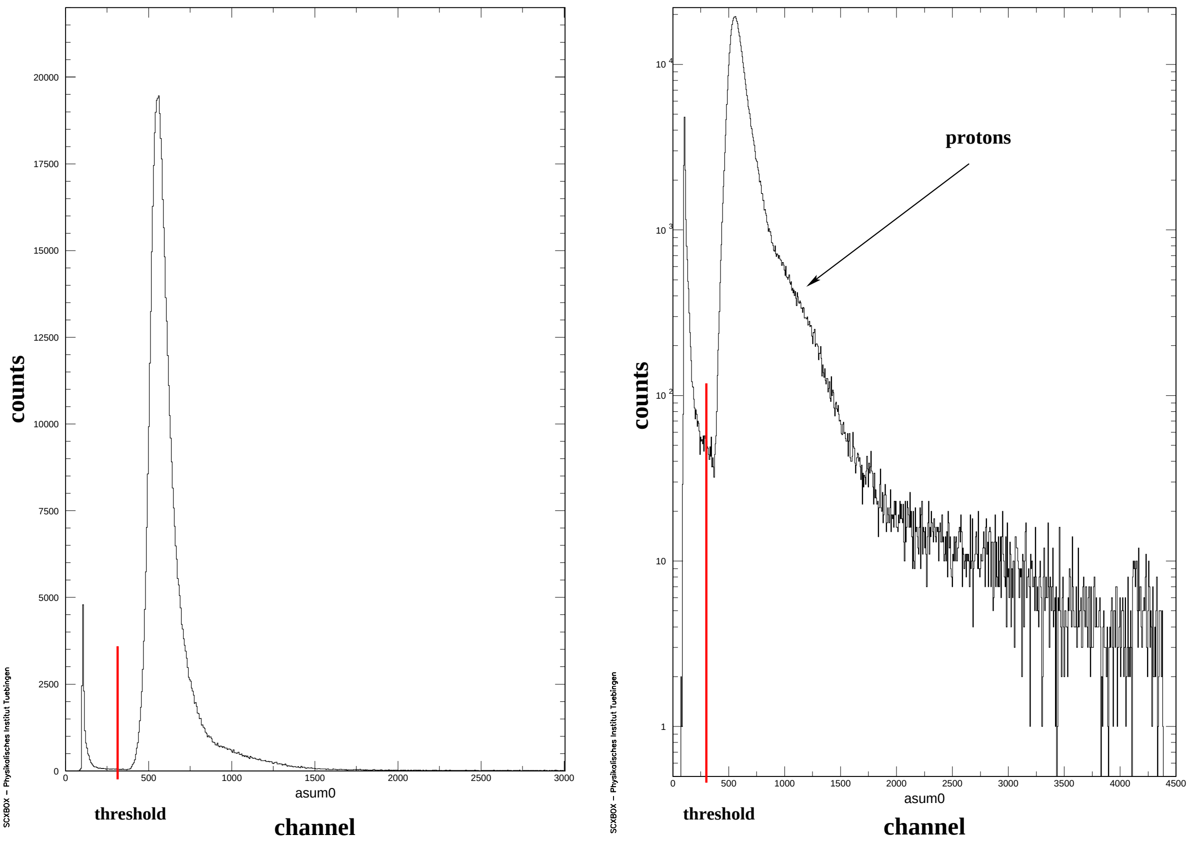

Figure 6.4: *Energy loss spectra in the back counter, linear (left) and logarithmic (right): Marked is the applied threshold of detected events*

is superimposed by a background of charged pions which first passed the target and were then scattered off the back detector. Only if this spectrum is generated under the condition that there was no hit in the back counter does the energy loss spectrum contain an elastic scattering peak (fig. 6.5 right hand side). The applied Gaussian fit gives a minimum which was used as the cut for scattered pion events.

6.6 Skimming

A practical step in the data analysis was the reduction of the amount of raw data. The idea of this process, which is called skimming, is that about 98 % of the transmitted pions leave the box detector through the back counter. For such an explicitly detected pion, there is no further need to look for coincident events in the other detector counters. Therefore for unique events of that type it is sufficient to increment the content of a scaler by one and to record the efficiency as well as the random content (compare Section 7.2). These events can then be removed from the raw data and the remaining events stored in a new and much smaller data file. Events with recoil protons originating from back scattered pions depositing energy in the back detector are also removed from the raw data and consequently counted as transmitted events. The advantage of the skimming process is that the data which are left for further analysis are reduced by a factor of 60 – 250, depending on the target and energy. The skimming process allows one to store all runs from one target and energy in one *ntuple* file. Further cuts and tests of the remaining events can then be applied easily and fast without the necessity of a new analysis of the data. The skimming process reduced the time for the data analysis. To ascertain that only events with a substantial charge deposition in the back detector underwent the simplified skimming process, the skim cut was applied in the rising slope of the energy loss spectra of the back counter such as it is shown in fig. 6.6.

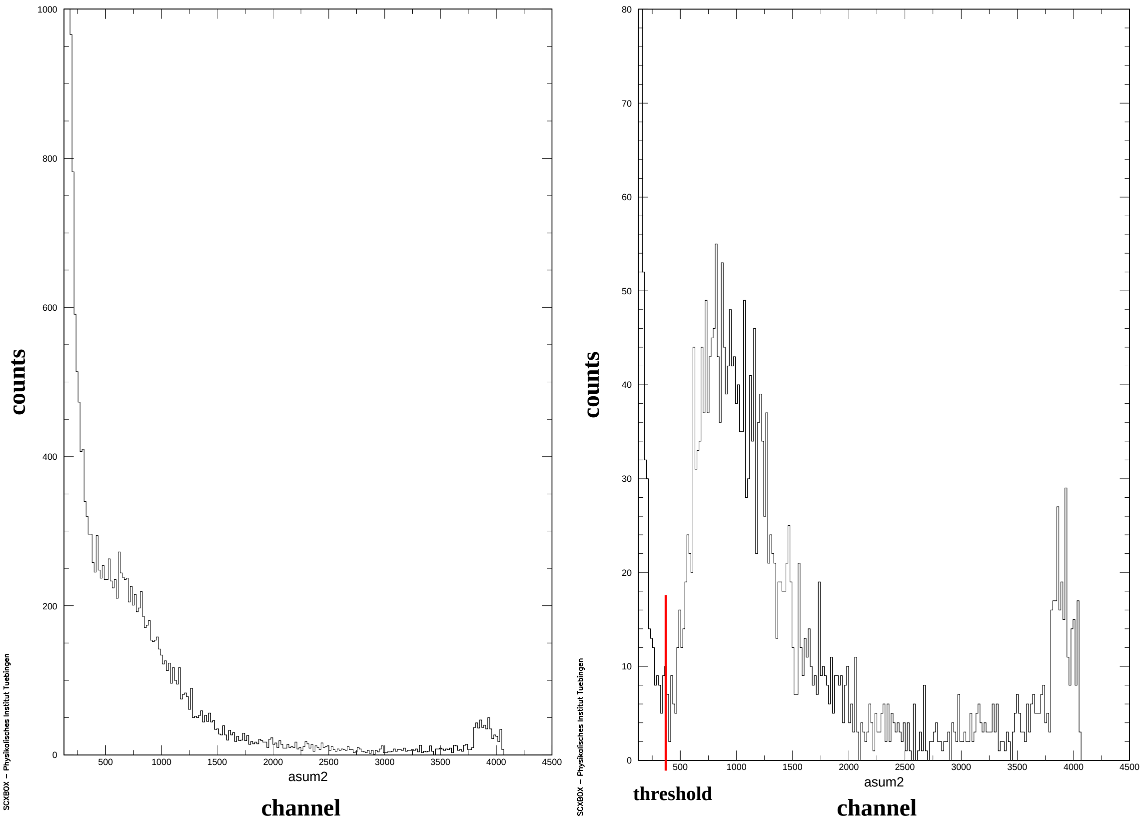

Figure 6.5: *Energy loss spectra in the up counter, for all events (left) and for events where there was no coincident detected event in the back counter (right). The detection threshold is represented by the solid bar.*

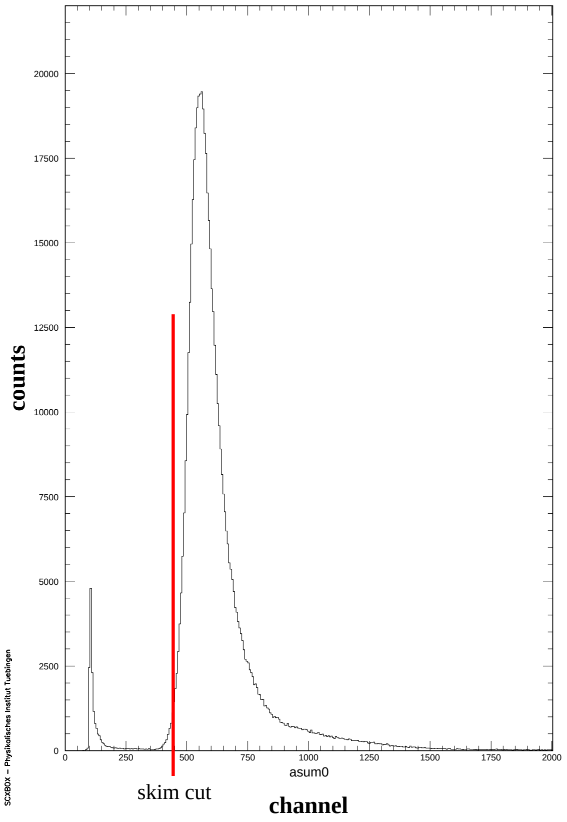

Figure 6.6: *Skim cut in the back counter spectra, all events right of the cut are counted and removed from the raw data.*

As a test the analysis was performed for one energy once without the skimming step and once with the skimming process. The numbers of transmitted events were exactly identical proving that the skimming process worked properly and did not influence our results.

6.7 Mid target energy

To tune the required pion energy and to determine the exact energy of the pions in the target, the energy settings of the beam lines were used as described in Section 4.2. The energy of the pions extracted from the production targets correspond to these settings. On their way to the target the pions have to pass the vacuum pipe windows, the three beam defining counters and the air from the end of the vacuum pipe to the target. The energy loss of the pions in this matter and half of the CH_2-target was calculated for each energy and subtracted from the tuned beam line energy.

6.8 The raw total SCX cross section

After the calibration and the determination of the thresholds in the spectra the extraction of the raw SCX cross sections is straightforward. For each target the transmission is determined (see Section 3.3) by

$$T = \frac{\text{transmitted events}}{\text{incident events}}.$$

The *incident events* are the counted pion trigger events. The *transmitted events* are extracted from the QDC spectra of the box detectors, applying the thresholds for transmitted events provided by the minima of the fits as described in Section 6.5.

The back counter was treated differently from the side counters: Since the majority of the transmitted events are detected by the back counter it seemed more convenient to count triggered events that were *not* detected in the back detector and mark them as *zeros*. “Detected events” are events with deposited energies above the threshold (fig. 6.4). To be more explicit, they are the skimmed events plus the events between the threshold (fig. 6.4) and the “skim cut” (see fig. 6.6). Consequently, “non detected events” are those below the threshold in the back detector and will be marked as “zeros”. Only in case of such a “zero” event were the side spectra analyzed.

If an event in the remaining box detectors was above the threshold it was counted as a detected event indicated as det_{up} for the up counter, det_{down} for the down counter, etc.. The following conditions were applied to obtain each event in the side detectors once and only once:

$$det_{up} = \overline{back} \cap up \tag{6.1}$$
$$det_{down} = \overline{back} \cap \overline{up} \cap down \tag{6.2}$$
$$det_{left} = \overline{back} \cap \overline{up} \cap \overline{down} \cap left \tag{6.3}$$
$$det_{right} = \overline{back} \cap \overline{up} \cap \overline{down} \cap \overline{left} \cap right \tag{6.4}$$
$$det_{front} = \overline{back} \cap \overline{up} \cap \overline{down} \cap \overline{left} \cap \overline{right} \cap front = single_{front} \tag{6.5}$$

Events detected in the side counters are:

$$\sum det_{side} = \sum det_{up} + \sum det_{down} + \sum det_{left} + \sum det_{right} + \sum single_{front} \tag{6.6}$$

The last condition (6.5) counts, in contrast to the other conditions, only true “single” hits in the front counter. Similarly, single events were also counted for the other detector parts:

$$single_{up} = \overline{back} \cap \overline{down} \cap \overline{left} \cap \overline{right} \cap \overline{front} \cap up \tag{6.7}$$

$$single_{down} = \overline{back} \cap \overline{up} \cap \overline{left} \cap \overline{right} \cap \overline{front} \cap down \tag{6.8}$$

$$single_{left} = \overline{back} \cap \overline{up} \cap \overline{down} \cap \overline{right} \cap \overline{front} \cap left \tag{6.9}$$

$$single_{right} = \overline{back} \cap \overline{up} \cap \overline{down} \cap \overline{left} \cap \overline{front} \cap right \tag{6.10}$$

And the sum of the single hits yields:

$$\begin{aligned}&\sum single_{side} = \\ &\quad \sum single_{up} + \sum single_{down} + \sum single_{left} + \sum single_{right} + \sum single_{front}\end{aligned} \tag{6.11}$$

Events where two or more of the side detectors were hit:

$$\sum multiple_{side} = \sum det_{side} - \sum single_{side} \tag{6.12}$$

The distinction between singles and multiples is important for the later efficiency corrections. Possible reactions yielding multiples are rescattering events in the counters, or for C-target nuclei, fraction debris causing the scattered pion or recoils to hit other detector counters afterwards and trigger more than one counter. The resulting raw transmission T is obtained by

$$\begin{aligned} T &= \frac{\sum \text{incident events} - (\sum zeros - (\sum single_{side} + \sum multiple))}{\sum \text{incident events}} \\ &= \frac{\sum det_{back} + \sum single_{side} + \sum multiple}{\sum \text{incident events}}. \end{aligned} \tag{6.13}$$

With the definition

$$\sum ors = \sum single_{side} + \sum multiple,$$

which correspond to $\sum det_{side}$ from equation 6.12, equation 6.13 is written as

$$T = \frac{\sum \text{incident events} - \sum zeros + \sum ors}{\sum \text{ incident events}}. \tag{6.14}$$

Note that for a det_{back} the side counters are ignored and therefore det_{back} includes events with or without hits in the side detectors (This will be of relevance for the corrections for random events). The raw SCX cross section is obtained from the measured transmissions of the different targets as described in Section 3.3.

Tables A.1 and A.2 show the number of *incident events* (triggers), extracted *zeros* and *ors* of each run for each of the three target measurements. The numbers are already corrected for detector efficiencies. The resulting cross sections are raw cross sections which still have to be corrected for various other (than efficiency) effects. The necessary corrections will be described in the following chapter.

Chapter 7

Corrections

This chapter deals with the different corrections which have to be applied to the extracted raw cross sections.

7.1 Efficiency correction

In Section 4.6 it has already been mentioned that the scintillation counters used, do not have an efficiency of 100 % for detecting charged pions. As well as the correction for random events, the efficiency correction can be directly obtained from the data taken.

The efficiency (ϵ) of the detector is a very important property (compare Section 4.6). A pion elastically scattered from the target which hits an efficiency counter has to pass the detector due to the geometric setup of the detector. The basic setup of the efficiency counters is indicated in fig. 4.8. The method used to obtain the detector efficiencies is to count the detector hits under the condition that an efficiency counter is also hit. The efficiency is given by the ratio number of coincident events to the number of events in the efficiency counter:

$$\epsilon = \frac{\sum det \cap effi}{\sum effi} \tag{7.1}$$

One problem that arises are random events which are events not related to the trigger event and which result mainly from other beam bunches (every 20 ns) or from other particles of the same beam bunch. Random events occur during the open QDC gate period (50 ns) while the data acquisition is waiting for signals. These randoms can hit the efficiency counters directly without passing the corresponding box detector and therefore reduce the measured efficiency. The random correction of the efficiencies is performed by only counting the events in the TDC spectra which occur in the *prompt* time window of 20 ns and subtracting the random events in this time interval:

$$\epsilon_{\text{corr}} = \frac{\sum(det \cap effi)_{prompt} - \sum(det \cap effi)_{random}}{\sum effi_{prompt} - \sum effi_{random}} \tag{7.2}$$

The prompt and random events are extracted from the recorded TDC spectra of the box and efficiency counters. The random events which occur in the prompt time interval are obtained from a random pulse which lies 20 ns earlier in the TDC spectrum. It is assumed that the same number of random events resides also within the prompt time window. The spectra are similar to the TDC spectra shown in fig. 7.2. For further informations concerning random events compare Section 7.2. Note that ϵ_{corr} is obtained from ratios in the TDC spectra and therefore is independent of their normalization.

The 7 mm thick back counter was a very efficient counter with an efficiency of 99.999 %. The 2 mm thick side counters had a typical efficiency of 99 %. For each counter the efficiency correction is applied to the measured events by dividing the detected number of events by the efficiency:

$$\sum det_{\text{effi corr}} = \frac{\sum det}{\epsilon_{corr}} \tag{7.3}$$

The $\sum det_{effi\ corr}$ represent the true number of detected events which were used to calculate the transmission. In terms of equation 6.11 and 6.12 this is written as:

$$\begin{aligned}\sum det_{side\ \ effi\ corr} = {} & \frac{\sum single_{up}}{\epsilon_{up}} + \frac{\sum single_{down}}{\epsilon_{down}} + \frac{\sum single_{left}}{\epsilon_{left}} + \frac{\sum single_{right}}{\epsilon_{right}} \\ & + \sum single_{front} + \sum multiple \end{aligned} \tag{7.4}$$

The efficiency of the back counter was monitored by three efficiency counters. One was positioned behind the center, the other two behind the left and right halves of the back scintillator. The measured efficiency for each of the counters was identical. The efficiency corrected *zero* events are given as

$$\sum zeros_{\ effi\ corr} = \sum \text{incident events} - \frac{\sum \text{incident events} - \sum zeros}{\epsilon_{back}}. \tag{7.5}$$

For technical reasons (compare Section 4.6) the front counter did not feature an efficiency counter and therefore the events from the front counter were not efficiency corrected. About 10^{-3} of the detected events hit the front counter. An efficiency correction would change the number of detected events on a level of 10^{-5} which definitely can be neglected. The efficiency correction of the multiples would result in an overcorrection because the probability of not detecting any event out of two hits is $\approx \ 10^{-5}$. Furthermore the multiples contribute only approximately $5 \cdot 10^{-4}$ to the number of detected events.

7.2 Correction for random events

The necessary information for random corrections was taken from TDC spectra such as in fig. 7.2. To generate the TDC start the last beam defining counter S3 was used in a coincidence logic with the S1 and S2 counters and the *tcap* (see fig. 4.15). The TDC stop for each channel was generated by a particle passing the specific counter and if no particle hit the counter during the open gate the TDC returned an entry into the overflow channel. In contrast to the QDC gate which was open for 50 ns the TDC gate was open longer and was closed after 156 ns. Fig. 7.1 shows a dotplot for the back counter where the QDC channel is plotted versus the TDC channel. The time when the gates were active is marked. All prompt entries in the QDC spectrum in fig. 6.4 are charges which were accumulated within the QDC gate marked in the TDC spectrum of fig. 7.1. The time spectrum of the back counter, as shown in fig. 7.2, is simply a projection of the spectrum in 7.1 and can be divided into three regions: The pre-prompt, prompt and post-prompt region.

7.3 Structure of the TDC spectra

Prompt region:
For the true events the start and stop of the TDCs result from the same beam particle, or its reaction products. The prompt peak also contains random background resulting from a secondary beam particle arriving together with the triggering event and hitting one of the box detectors, even if the triggering particle underwent a SCX process. Below we shall explain how the random events in the prompt time region were accounted for.

Pre-prompt region:
The majority of random events are produced by beam particles bypassing the beam defining counters. These are caused by pion events that generate the TDC start but do not stop it, since another, e. g. *earlier* particle stopped the TDC. As there exists no fixed time relation between these two events these random events produce a continuous background in the TDC spectra

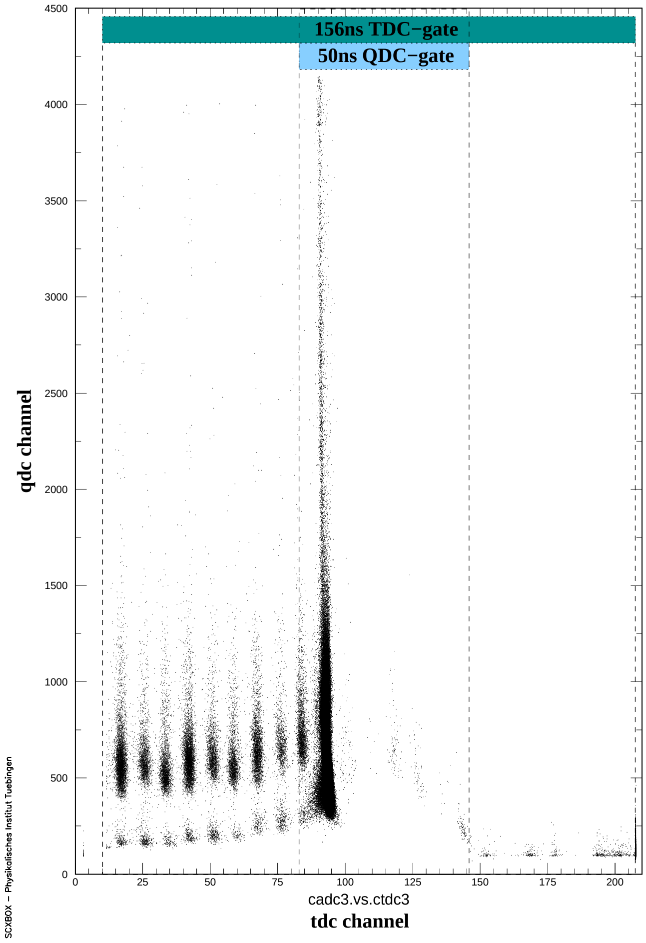

Figure 7.1: *Dotplot QDC versus TDC for the back counter. The TDC gate was active for 156 ns and the QDC gate was active for 50 ns.*

which is modulated by the 19.75 ns bunch structure of the accelerator (see figs. 7.2). In one of the worst cases of randoms the trigger rate was 6.1 kHz. With the 50 MHz of the cyclotron on the average a valid beam event was triggered only every ≈ 8200 cycles. The rate on the back counter was ≈ 98 % of the trigger rate if the trigger condition was included (compare Section 6.5). However without the trigger condition the uncorrelated raw rate on the back counter was e. g. about 1.3 MHz. This corresponds to approximately one event in every 38 beam cycles. The reason for this discrepancy is the geometry of the back detector with a 10 x 10.4 cm^2 plane perpendicular to the beam and the beam spread of the same order. The side counters are oriented parallel to the beam path and still see a rate between 60 and 300 kHz. With the same orientation as the back detector the front detector sees a total rate of ≈ 1.3 MHz. The probability for a hit in the back counter additional to the triggered event is 50 ns · 1.3 MHz = 0.065. For 6.5 % of the triggered events an additional particle hits the back counter. This means that one out of 15 SCX events with an outgoing neutral particle will be concealed by a random charged event hitting the back detector what is not negligible. Thus a random correction is essential.

Post-prompt region:
As shown in fig. 7.2 randoms are also present *after* the prompt peak if there was no prompt hit and if a particle from a later bunch hit the counter. The TDCs used were single hit TDCs which implies that the TDC only can register one hit which stops the TDC. The first detected hit stops the TDC and a possible later hit then gives no entry in the TDC spectrum. This effect is called shadowing. The shadowing caused by the few randoms is too small and can be neglected. This can be seen in the flat envelopes of the pre-prompt or post-prompt parts

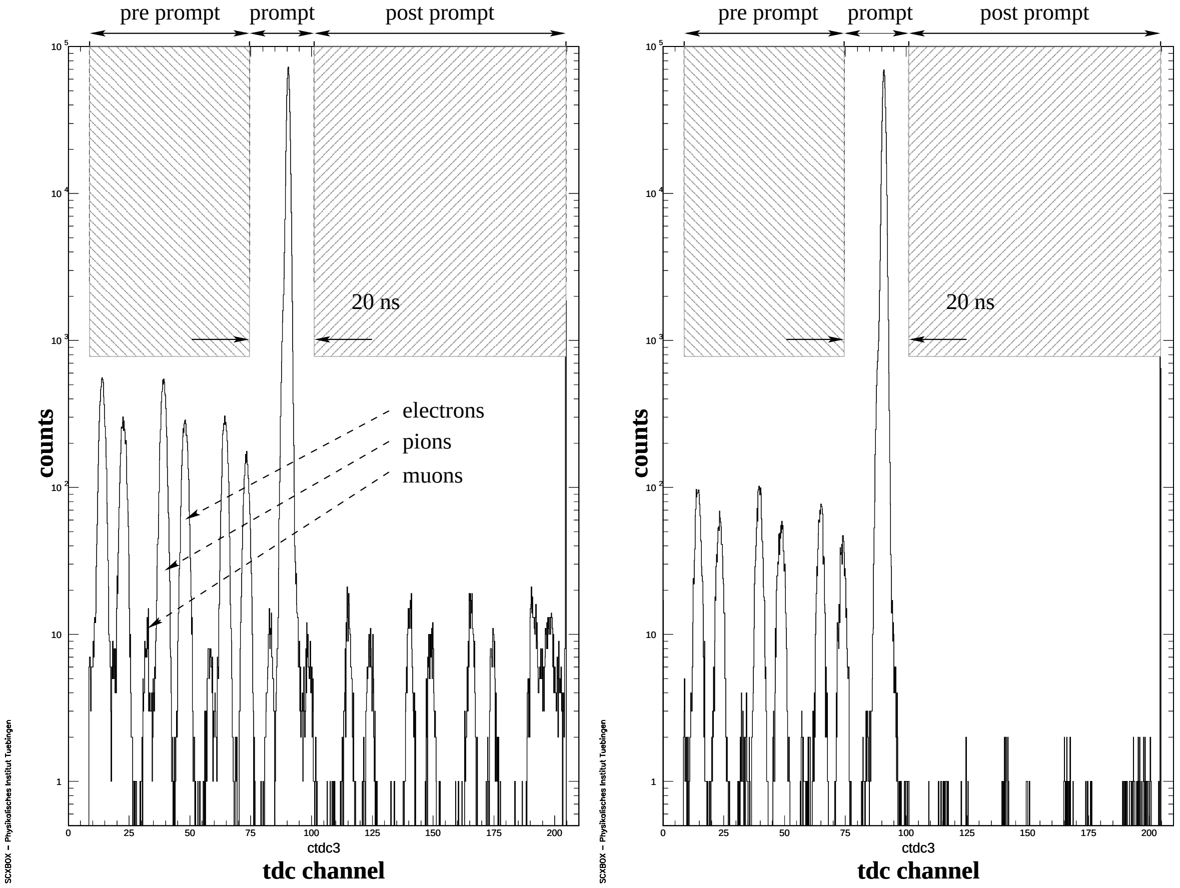

Figure 7.2: *Logarithmic TDC spectra of the back counter for a high rate (left) and a low rate (right) measurement*

of the spectra in fig. 7.2. The prompt events are dominant and therefore cause a substantial shadowing of the post-prompt spectrum. The number of randoms are roughly the same over the whole TDC range, but as seen in fig. 7.2 the post-prompt region contains fewer entries due to the shadowing caused by the prompt events. For a given momentum the three different particle types (e^-, μ^-, π^-) have different time of flights. For the three particle types each beam bunch encloses three separate peaks in the TDC spectra.

Estimation of the random correction

The QDC spectra were used to extract the transmitted detected events. We recall that for each trigger the QDCs accumulated incoming charge during 50 ns. This raw extraction also includes random events which were detected within the open QDC gate. For these random events a correction had to be applied. The simplest method would be to count the number of random and prompt events in the TDCs and use this information for a simple subtraction of the randoms from the prompt events. The problem that arises here is that the TDC has one specific hardware threshold, which could not be changed in the analysis. Therefore it was possible that for a QDC entry the TDC did not trigger because the signal was below the TDC threshold. Basing the analysis on the QDC spectra allows different thresholds to be used as well as the generation of TDC spectra related to the applied QDC thresholds. Thus, in the analysis, the detected events were extracted from the QDC spectra and the TDCs were used for the random correction. The extracted correction had to be independent of numbers of events and simply used the ratio between random and prompt events. The number of prompt events is determined from the contents during a 20 ns period which includes the prompt peak as well as the random pions, muons and electrons. The random events were counted within the 20 ns interval of a beam cycle before the prompt peak. The random events occurring within the 50 ns QDC gate were obtained by multiplying the random events with a factor of $t_{\text{QDC gate}}/t_{\text{beam cycle}} = 2.5$. For each of the side detectors the applied correction is:

$$\sum det_{\text{rnd corr}} = \sum det_{QDC} \cdot (1 - \frac{2.5 \cdot \sum random_{TDC}}{\sum prompt_{TDC} - \sum random_{TDC}}) \tag{7.6}$$

For all detected events in the side detectors it follows that:

$$\sum ors_{rnd\ corr} = \sum single_{side\ rnd\ corr} + \sum multiple \tag{7.7}$$

A random correction of the multiples is negligible since they contribute on a level of $5 \cdot 10^{-4}$ to the number of detected events. The correction applied for the back counter is more subtle. Here the events without a QDC entry, the so called *zeros*, are subject to correction. In a first approximation the correction follows the correction of the detected events (see equation 7.6). The increase of the *zeros* accounts for the concealing of *zeros* through random hits. The analysis process looks for single hits in the side counters but counts *each* hit in the back counter whether there was a hit in a side counter or not (hits in the back counter are single hits or multiple hits). Now, in the random correction for the back counter one recovers *zeros* for which the side counters were not analyzed. With a certain probability one would have found a side event thus destroying the *zero*. In next order the recovered *zeros* have to be corrected:

The first order correction is, by the same reasoning as above,

$$\sum zeros_{\text{rnd corr}} = \sum zeros \cdot (1 + \frac{2.5 \cdot \sum random}{\sum prompt - \sum random}) \tag{7.8}$$

With the corrected random content

$$\sum random = \sum zeros_{\text{rnd corr}} - \sum zeros = \sum zeros \cdot \frac{2.5 \cdot \sum random}{\sum prompt - \sum random}. \tag{7.9}$$

In second order the $zeros_{rnd\ corr}$ have to be reduced by the number of restored *zeros* for which a side event would have been found, had it not been for our strategy, that side detectors are ignored, if a hit in the back detector was found. The modified random content is as follows:

$$\sum random' = \sum random(1 - \frac{\sum ors_{rnd\ corr}}{\sum zeros_{rnd\ corr}}) \tag{7.10}$$

The correction $\sum ors_{rnd\ corr}/\sum zeros_{rnd\ corr}$ obviously represents the probability to observe a side detector event for a given *zero* event. It is sufficiently accurate to use the first order value $\sum zeros_{rnd\ corr}$ for this estimate and no iteration is required. The final result therefore is

$$\sum zeros'_{\text{rnd corr}} = \sum zeros \cdot (1 + \frac{2.5 \cdot \sum random}{\sum prompt - \sum random}(1 - \frac{\sum ors_{rnd\ corr}}{\sum zeros_{rnd\ corr}})). \tag{7.11}$$

Application

The random correction varied between 0.4 % and 10.5 % of the total SCX cross section depending on the beam rate and the beam line used. In general 10 % of the applied random correction resulted from the side counters and 90 % from the back counter. For the random correction of the πM1 measurements the TDC information was used as described.

Unfortunately the use of the TDC spectra in the πE3 runs was not possible. The timing was accidentally set up in a way that the TDC start was too close to the prompt events and as a result the pre-prompt random interval could not be extracted for a full beam cycle of 20 ns. This problem is evident in the spectra 7.3 and can be compared to fig. 7.2 from the πM1 beamline where the prompt peak is properly placed in the middle of the TOF spectrum. The post prompt region is shadowed by the prompt events and therefore no reliable random correction could be extracted from the post-prompt randoms. Fortunately the random background, relative to the true events, was in general about 10 times smaller in the πE3 channel than in the πM1 channel. This can be seen in the comparison of the ratio between the random and the prompt peak hight in the spectra in fig. 7.2 and 7.3 (left).

Fortunately, for all the runs in the πE3 channel and for some energies in the πM1 channel a **F**lash **A**nalog to **D**igital **C**onverter (FADC[1]) was connected to the back and front counter and recorded the pulse shape for each event. The FADC output for a single beam event is shown in fig. 7.4.

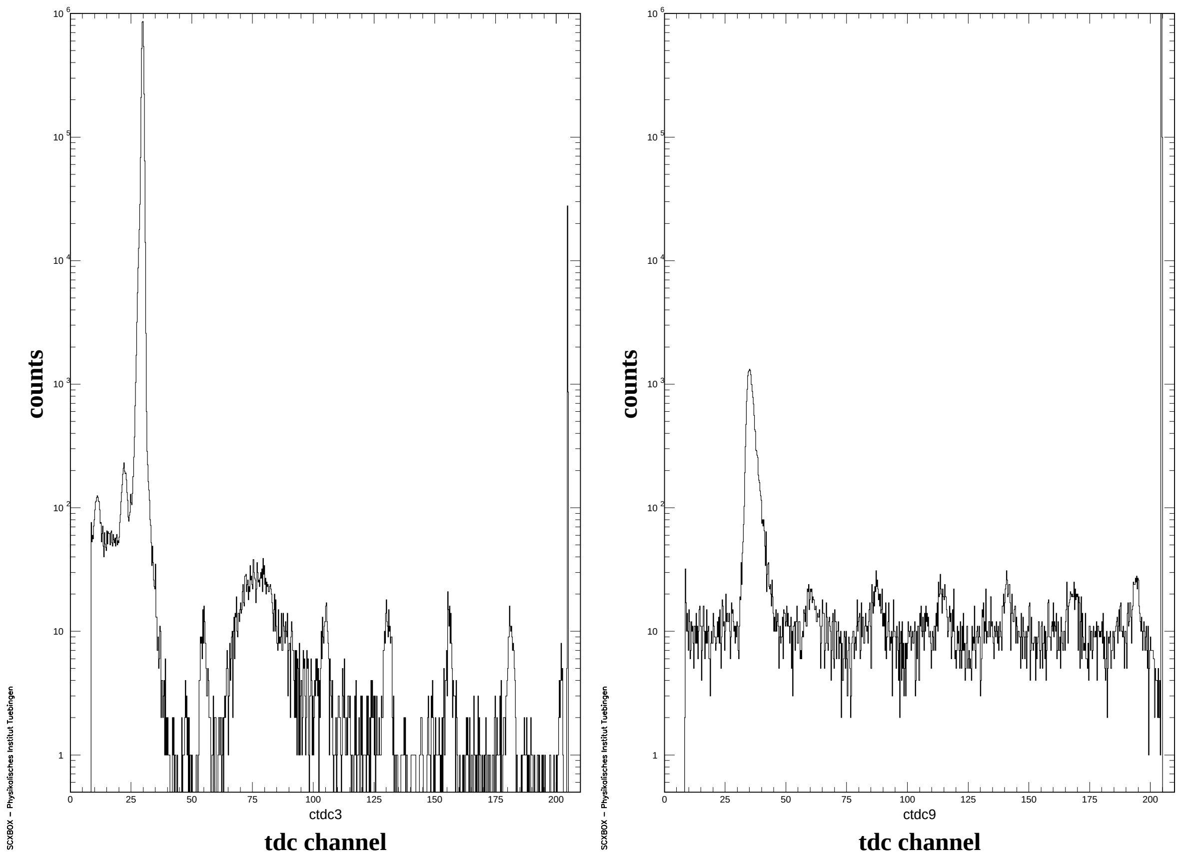

Figure 7.3: *TDC spectra of the back (left) and for a side (right) counter for a πE3 run*

For each trigger the FADC recorded a time interval of 128 ns with a sample rate of 4 ns and a depth of 8 bit. This information could be used to create QDC and TDC spectra. A simple but effective algorithm was used to create a TDC spectrum with a 4 ns time resolution: The FADC pulse was scanned for a rise in the signal which rises within 2 bins (8 ns) to full height. For the signal maximum a histogram was filled with an entry in the time axis, the algorithm stopped the scanning process and started with the next trigger event. TDC spectra for the back and front counters are shown in fig. 7.5.

From the generated TDC spectra the random correction was determined in the same manner as described before in this section. A comparison of the resulting random correction obtained from the TDC and the FADC for the few πM1 beamline energies where both spectra were available, gives an excellent agreement. This confirms, in spite of the poor time resolution of 4 ns, that the method used to determine the random correction from the FADC output worked. Hence the FADC generated TDC-spectra were used for all πE3 runs.

---

[1] VMW Wiener 7515, 4 channel FADC with a 250 MHz sample rate for each channel

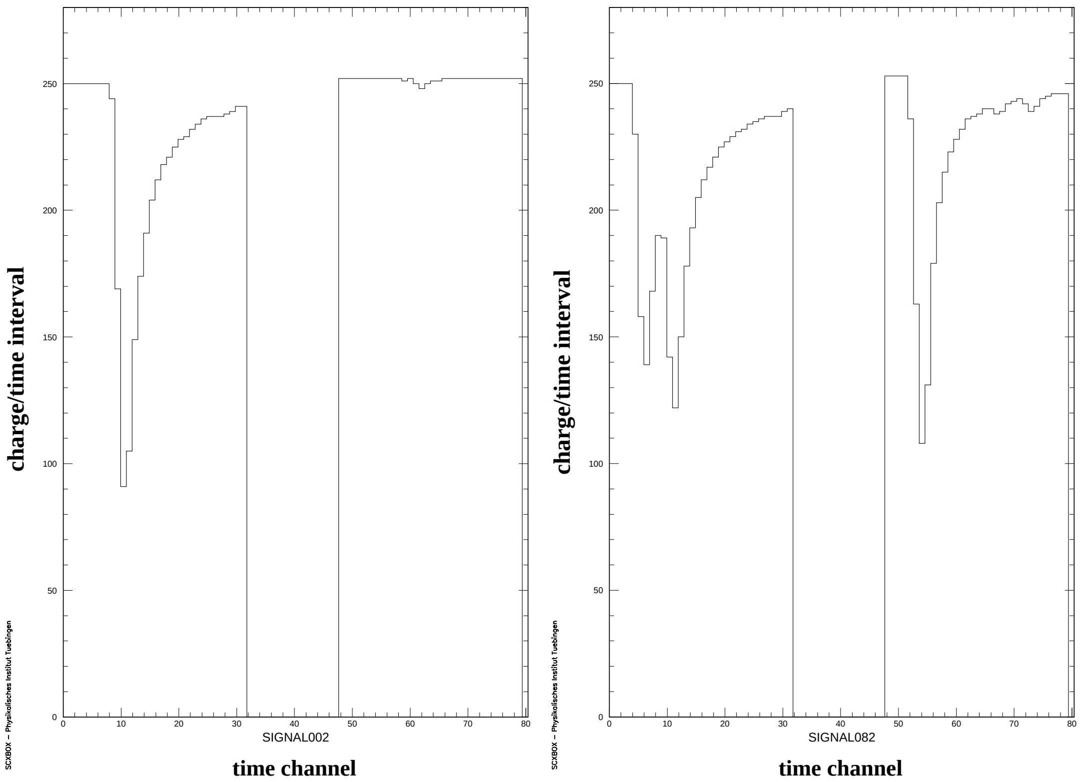

Figure 7.4: *FADC: Digitized pulse shape of a prompt pion in the back counter (channel 1 - 32 $\widehat{=}$ 128 ns) and the front counter (channel 48 - 79 $\widehat{=}$ 128 ns). In the left spectrum a single transmitted prompt event hits the back counter. The right spectrum shows a single hit of a transmitted prompt beam event in the back counter accompanied by a random event 20 ns earlier passing the back and the front counter.*

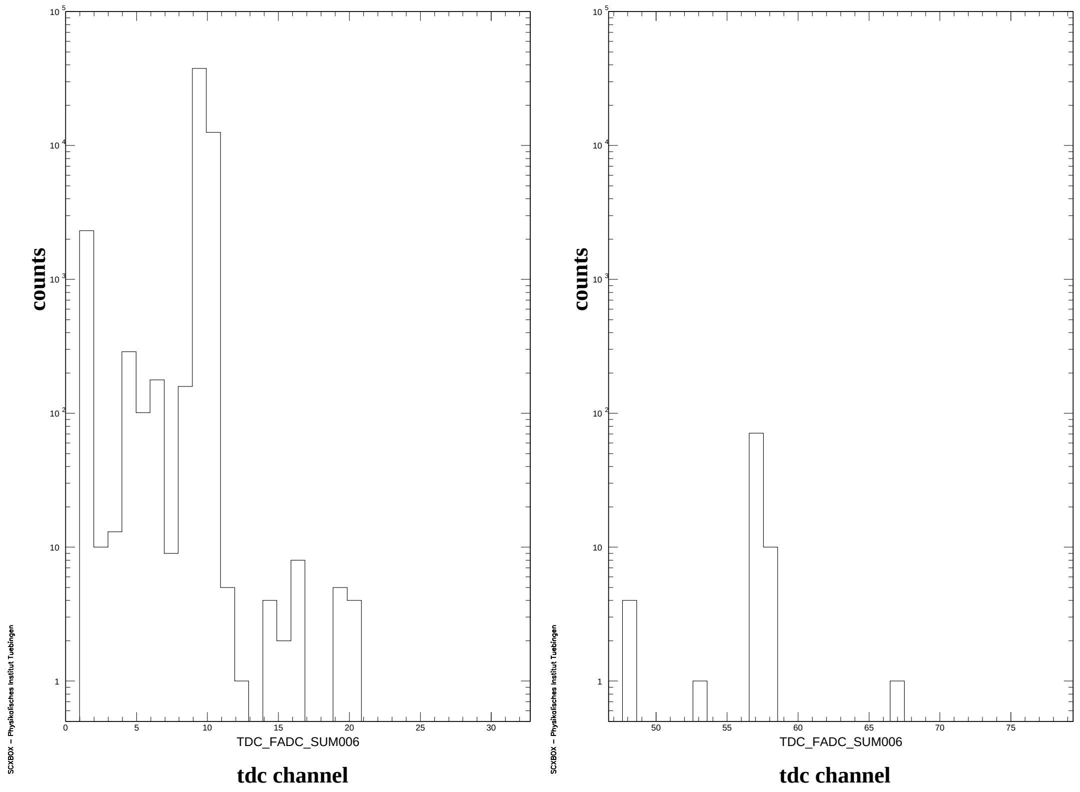

Figure 7.5: *TDC spectrum of the back (left) and the front counters (right) generated from the FADC data. The binning width of 4 ns results from the FADC sampling rate.*

Table 7.1: *Random correction for the πE3 channel*

Run ID	T_{exp} [MeV]	σ [mb] effi. corrected	rnd. corr. [mb]	σ_{raw} [mb] effi. rnd. corrected
1a[a]	−38.92	6.96(29)	0.06	7.02(29)
1b	−38.92	7.07(16)	0.08	7.15(16)
2	+38.92	1.78(16)	0.03	1.81(16)
3a	−39.48	4.31(52)	0.13	4.44(53)
3b	−39.48	4.76(24)	0.03	4.80(24)
4	+39.48	−0.56(26)	0.05	−0.61(26)
5	−39.72	5.63(32)	0.03	5.67(32)
6	−42.99	5.30(10)	0.03	5.33(10)
7a	−47.10	5.57(17)	0.03	5.60(17)
7b	−47.10	4.94(31)	0.02	4.96(31)
8	−47.61	5.39(34)	0.04	5.42(34)
9	−47.82	7.15(42)	0.04	7.19(42)
11a	−64.27	7.16(22)	0.03	7.19(22)
11b	−64.27	6.79(16)	0.03	6.81(16)
12	+64.27	−0.42(15)	0.02	−0.44(15)
15	−75.09	8.51(14)	0.07	8.58(14)
16	+75.09	−0.53(11)	0.00	−0.53(11)

[a] For more details about the subdivision of the run ID's (a, b, c, d) see Appendix A.

Table 7.2: *Random correction for the πM1 channel*

Run ID	T_{exp} [MeV]	σ [mb] effi. corrected	rnd. corr. [mb]	σ_{raw} [mb] effi. rnd. corrected
10a	−55.55	6.08(21)	0.26	6.34(22)
10b	−55.55	6.09(14)	0.32	6.41(15)
13a	−65.88	7.10(16)	0.40	7.50(17)
13b	−65.88	6.55(40)	0.47	7.02(42)
13c	−65.88	6.26(74)	0.58	6.84(76)
14	−66.31	7.47(40)	0.34	7.81(41)
17a	−76.10	8.15(23)	0.58	8.73(24)
17b	−76.10	8.87(18)	1.05	9.92(19)
17c	−76.10	8.35(38)	0.31	8.67(39)
17d	−76.10	9.53(67)	−0.02	9.51(67)
18	−96.47	14.64(24)	0.28	14.92(25)
19	−106.54	17.79(26)	0.50	18.29(26)
20	−116.62	22.74(19)	0.31	23.05(19)
21a	−126.70	27.03(41)	0.22	27.25(41)
21b	−126.70	25.44(38)	0.92	26.36(38)
22	+126.70	0.02(13)	0.05	0.07(14)
23	−135.92	32.63(25)	0.28	32.91(25)
24	−164.89	43.01(41)	0.27	43.28(42)
25	−165.22	42.75(57)	0.28	43.03(58)
26	−176.86	42.68(28)	0.27	42.95(28)
27	−196.96	38.53(26)	0.24	38.77(26)
28	−216.99	32.36(28)	0.21	32.57(28)
29	−217.29	32.32(34)	0.22	32.54(34)
30	−247.00	23.46(21)	0.23	23.69(21)

The random corrections applied for the different measurements is listed in tables 7.1 and 7.2. The random correction of the πE3 data consist only of corrections obtained from the front and back counter. As pointed out before the latter is responsible for about 90 % of the random correction and the correction of the πE3 data is very small, between 0.4 % and 4 % of the cross section. The side counters contribute approximately 10 % to the random correction and in the πE3 measurements the contribution of the side counters to the random correction was neglected. We denote the random and efficiency corrected results by σ_{raw}.

7.4 Corrections using Monte Carlo simulations

The detection of the outgoing neutrals from the SCX reaction and the pion decay was treated by Monte Carlo simulations. The simulation tools GEANT3 [GEANT3] based on the programming language FORTRAN, and GEANT4 [GEANT4] based on the C language were used for the simulations. The accurate detector setup initially programmed into GEANT3 (see fig. 7.6) could be imported and used in the GEANT4 simulations as well.

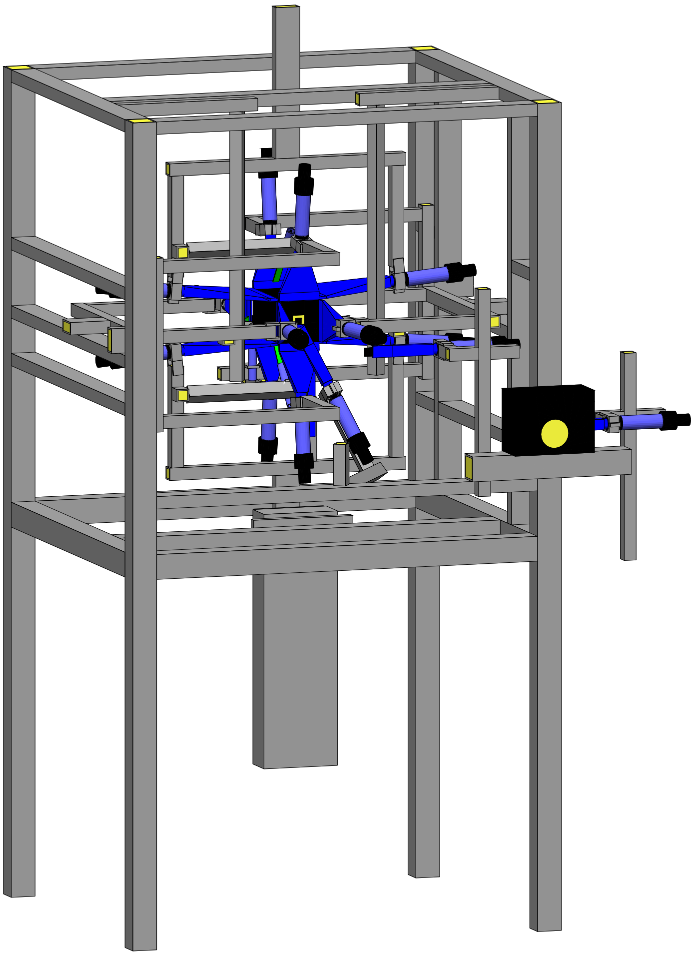

Figure 7.6: *Detector geometry used in the GEANT simulations.*

The models for the hadronic reactions included in GEANT3 contain considerable uncertainties. To meet the requirement of high accuracy a repetition of the simulations using GEANT4 was required. GEANT4 uses better models for the reactions of neutrons, especially at low energies. The GEANT4 simulations were performed within the framework of a diploma thesis by M. Bauer [Bau03]. Charged particles passing matter lose energy by ionization of atoms. The resulting so called δ-electrons usually have very low energies which are often below the detection threshold of the detectors used and it was not necessary to track these electrons in the simulation. Tests with different thresholds for the tracking energy were done (see [Bau03]). The corrections that were used here were taken from these GEANT4 calculations and had a tracking threshold energy of 100 keV.

7.4.1 Detection of neutrals

The correction for the detection of the neutrals specifies the probability of detecting a neutral particle (n , γ) or its reaction products in the 4π-detector and treating it falsely as a non-SCX event. Events fulfilling the beam definition and undergoing the SCX reaction with the subsequent deposition of at least the threshold energy in one of the box counters by an electromagnetic particle (e^+, e^-, γ) or a neutron are considered as such events. GEANT3 and GEANT4 used the same detector geometry as an input. The simulation can be compared to the measurement in the sense of an event by event particle creation with a specific momentum and location, particle tracking and interaction with matter. For the determination of the corrections only the SCX events are relevant out of all the possible reaction events. To simulate the SCX reaction and the detector response for this reaction, an event generator was used which produced a SCX reaction if a simulated primary pion hit the target. The reaction point in the target was chosen at random in a uniform distribution over the target volume.

Neutrons

The energy deposited by a hadron (proton, ion) that was traced, originating as neutron recoil, was the condition for a *detected* neutron. The interaction of neutrons comes with high uncertainties and therefore the systematic error was estimated to be 20 % of the correction using the GEANT3 simulations. In the final analysis the GEANT4 results were used because of the improved implementation of hadronic interactions which had motivated the GEANT4 simulations originally. Comparing the two GEANT results shows that the improved hadronic models in GEANT4 result in higher corrections at low energies (compare fig. 7.7). Possibly this results from the negligence of inelastic scattering processes in GEANT3 [Sch05]. The differences between GEANT3 and GEANT4 results will be accounted for as systematic uncertainty.

Gammas

One of the electromagnetic corrections is the detection of gammas resulting from the π^0 decay which generate secondary particles. Surprisingly the GEANT4 corrections obtained are higher than the GEANT3 corrections. The explanation for this is to be found in the lower detection thresholds for δ-electrons in the GEANT4 simulations.

Dalitz decay

The branching ratio for the Dalitz decay, $\pi^0 \rightarrow \gamma\, e^+e^-$, is very well known to be (1.198 ± 0.032) % [PDB] and the calculated GEANT3 and GEANT4 corrections show good agreement with this input value. Again the GEANT4 results were used for this correction. Fig. 7.8 shows the simulated fraction of the π^0 decay observed.

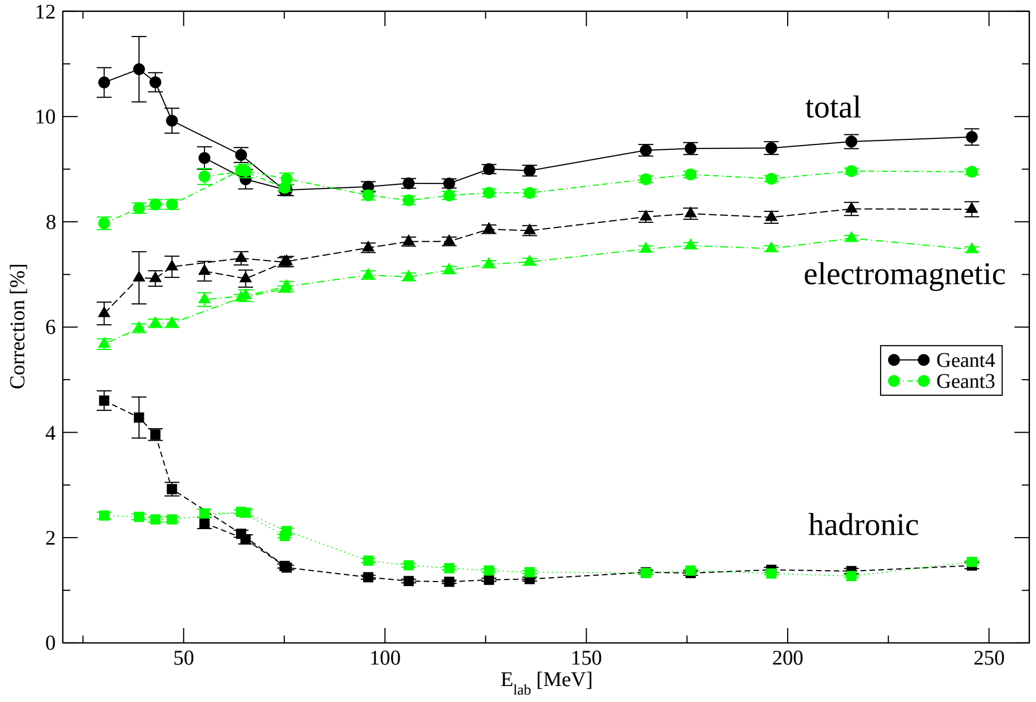

Figure 7.7: *GEANT3 and GEANT4 correction for neutrons and gammas as a percentage of all SCX-events*

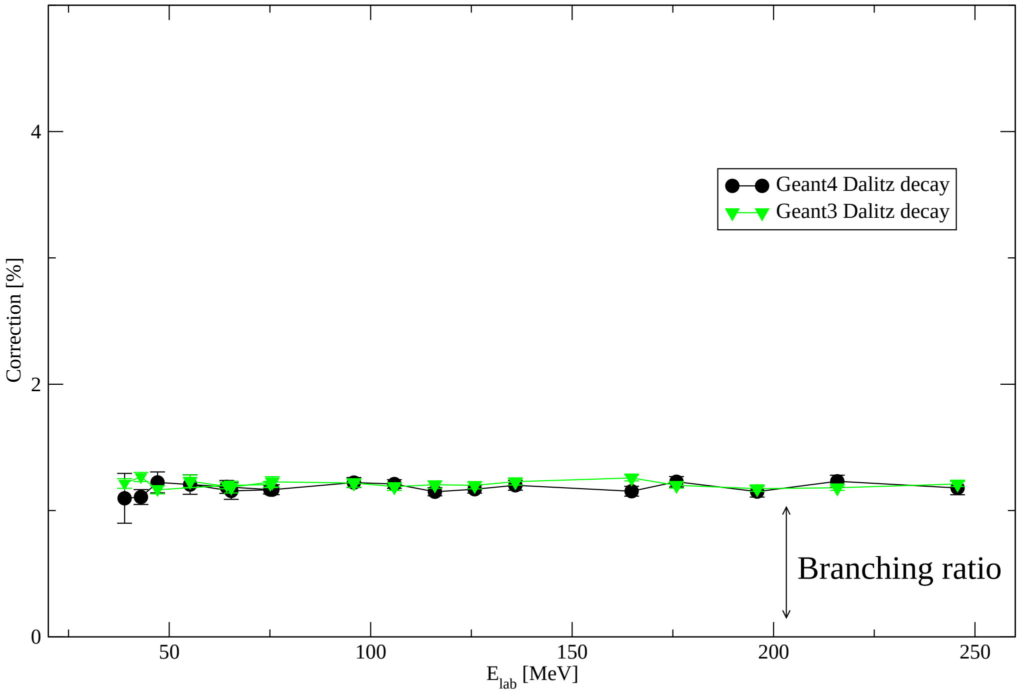

Figure 7.8: *Monte Carlo corrections for observed Dalitz decays as a percentage of all SCX-events*

7.4.2 Muon contamination of the beam

A further distortion of the SCX measurements arises from the weak π^- decay:

$$\pi^- \longrightarrow \mu^- \bar{\nu}_\pi \qquad\qquad \tau_\pi = 26 \text{ ns}$$

A pion decaying somewhere behind the last beamline magnet with the resulting muon fulfilling the beam definition will appear in the TOF spectrum of the S3 counter within the pion peak. It is impossible to identify these events in the analysis using the spectra recorded and therefore the number of muons have to be calculated in the MC simulation. The muons resulting from the decay kinematics end up in a decay cone with an angle depending on the energy of the pion. Therefore only a few of the decay muons follow the original flight path of the pion. Because this correction is straightforward in a Monte Carlo simulation and does not underly any complicated interaction models it was only determined with GEANT3. In fig. 7.9 the fraction of emerging muons is shown. The applied correction follows from the number of muons N_μ fulfilling the beam definition after the decay and the number of incident pions N_π:

$$\kappa_\mu = \frac{N_\mu}{N_\mu + N_\pi}$$

As seen in fig. 7.9 the correction does not strongly depend on the incident pion energy. At low energies the probability for a π^- decay increases but the angle of the muon cone opens up and therefore more muons miss the beam defining counters. The different experimental conditions in the πM1 and in the πE3 channel (distances between the beam defining counters) appear in

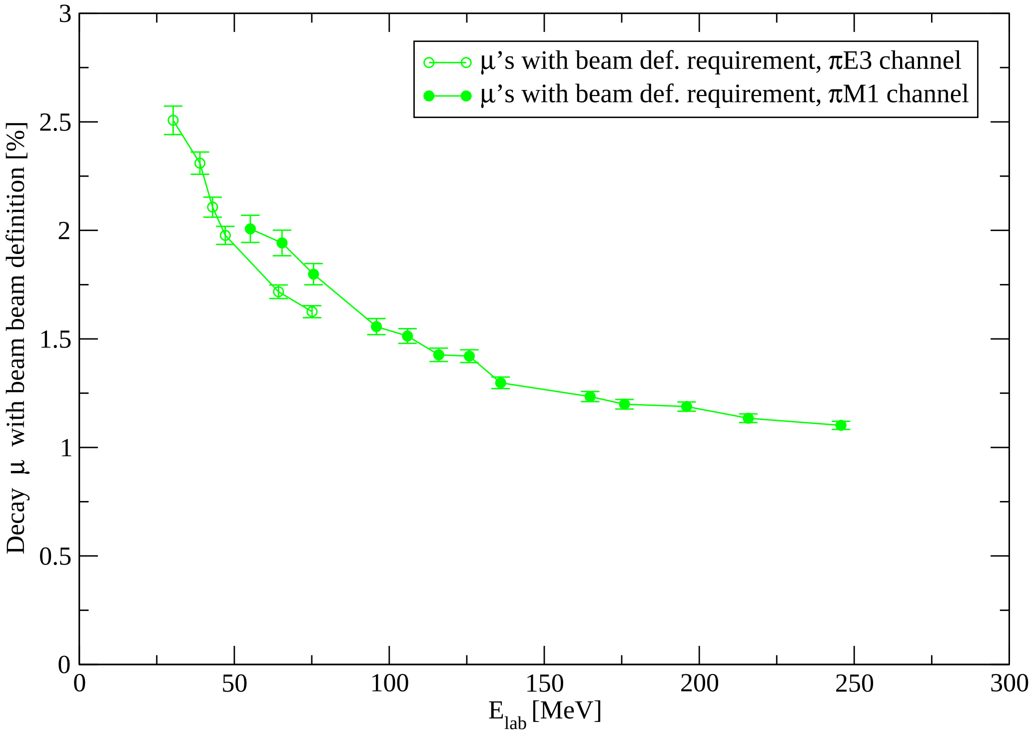

Figure 7.9: *Fraction of pions decaying into muons, extracted from the GEANT3 MC simulations. The correction results from the number of muons fulfilling the beam definition after the pion decay.*

the simulated muon fraction of the incident beam. The distance between the beam defining counters in the πE3 channel was shorter, therefore for identical energies fewer pions decay on their way to the target in the πE3 than in the πM1 channel.
The simulation of the beam started at a distance of 213 cm upstream from the target as a random homogeneous distribution of 2 x 2 cm^2 with a specified momentum along the flight path and no transverse momentum. The simulations always require that the beam definition which allows only a 2.1 x 2.1 cm^2 beam spot on the target is fulfilled. Therefore the simulation of a wider or divergent beam would not make a difference. As a test, a simulation with a different starting point was performed for generated pions of 125 MeV. The starting point was 400 cm upstream of the target compared to the 213 cm of the original simulation. There was no difference between the two simulations in the resulting corrections.

7.4.3 Application of the MC correction

The calculated correction was applied to the average cross section σ_{av} (see tables 10.1, 10.2) which is corrected for random, efficiency, target thickness and mid target energy. The corrections ($\kappa_{hadr},\ \kappa_{em},\ \kappa_{\mu},\ \kappa_{Dalitz}$) are given as a percentage and are applied as follows:

$$\sigma_{MC_{corr}} = \sigma_{av} \cdot \frac{1}{(1-\kappa_{hadr})\cdot(1-\kappa_{em})\cdot(1-\kappa_{Dalitz})\cdot(1-\kappa_{\mu})}$$

The absolute MC corrections ($\sigma_{MC_{corr}} - \sigma_{av}$) are listed in the tables 7.3, 7.4.

7.5 Radiative capture

The transmission measurement implies the detection of transmitted charged particles. The SCX process reduces the transmitted intensity of charged reaction products. Another reaction channel with outgoing neutrals which contributes to the decrease of the transmission is the radiative pion capture:

$$\pi^- p \rightarrow \gamma n$$

The total cross section for pion capture (σ_{RC}) had to be subtracted from the measured corrected cross section (see table 10.2):

$$\sigma_{final} = \sigma_{MC_{corr}} - \sigma_{RC}$$

The total cross section for radiative capture is obtained from the inverse photoproduction reaction

$$\gamma n \rightarrow \pi^- p.$$

From the priniple of detailed balance we obtain

$$\sigma_{tot}(\pi^- p \rightarrow n\gamma) = \frac{n_\gamma n_n}{n_{\pi^-} n_p} \frac{P^2_{\gamma\ cm}}{P^2_{\pi^-\ cm}} \sigma_{tot}(\gamma n \rightarrow \pi^- p) \tag{7.12}$$

where the statistical factor $n = 2s+1$, except for real photons which are always transversely polarized. Hence $n_\gamma = 2$ and we obtain

$$\sigma_{tot}(\pi^- p \rightarrow n\gamma) = 2\frac{P^2_{\gamma\ cm}}{P^2_{\pi^-\ cm}} \sigma_{tot}(\gamma n \rightarrow \pi^- p) \tag{7.13}$$

(see [Loc69]) with gamma momentum $P_{\gamma\ cm}$ and pion momentum $P_{\pi^-\ cm}$ written in the CM system. The photo nuclear cross section $\sigma_{tot}(\pi^- p \rightarrow n\gamma)$ was obtained from the SAID web page [SAID]. The radiative capture cross sections calculated for pion lab energies are listed in the tables 7.3 and 7.4.

Table 7.3: *MC and radiative capture corrections for the πE3 channel given as a percentage of the σ_{av} cross section (see table 10.1)*

Run ID	T_{exp} [MeV]	el.magn. hadr. %	π^- decay %	Dalitz decay %	total MC [mb]	radiative [mb]
1a	−38.92	10.90(62)	2.31(05)	1.10(20)	0.90	−0.74
1b	−38.92	10.90(62)	2.31(05)	1.10(20)	0.90	−0.74
3a	−39.48	10.90(62)	2.31(05)	1.10(20)	0.90	−0.74
3b	−39.48	10.90(62)	2.31(05)	1.10(20)	0.90	−0.74
5	−39.72	10.90(62)	2.31(05)	1.10(20)	0.90	−0.74
6	−42.99	10.65(18)	2.11(04)	1.11(06)	0.97	−0.72
7a	−47.10	9.92(24)	1.98(04)	1.22(08)	0.93	−0.69
7b	−47.10	9.92(24)	1.98(04)	1.22(08)	0.93	−0.69
8	−47.61	9.92(24)	1.98(04)	1.22(08)	0.93	−0.69
9	−47.82	9.92(24)	1.98(04)	1.22(08)	0.93	−0.69
11a	−64.27	9.27(14)	1.72(03)	1.19(05)	1.03	−0.65
11b	−64.27	9.27(14)	1.72(03)	1.19(05)	1.03	−0.65
15	−75.09	8.60(09)	1.80(04)	1.17(03)	1.17	−0.64

Table 7.4: *MC and radiative capture corrections for the πM1 channel given as a percentage of the σ_{av} cross section (see table 10.2)*

Run ID	T_{exp} [MeV]	el.magn. hadr. %	π^- decay %	Dalitz decay %	total MC [mb]	radiative [mb]
10a	−55.55	9.21(21)	2.01(06)	1.21(08)	0.99	−0.67
10b	−55.55	9.21(21)	2.01(06)	1.21(08)	0.99	−0.67
10c	−55.55	9.21(21)	2.01(06)	1.21(08)	0.99	−0.67
13a	−65.88	8.81(18)	1.72(03)	1.16(07)	1.04	−0.65
13b	−65.88	8.81(18)	1.72(03)	1.16(07)	1.04	−0.65
13c	−65.88	8.81(18)	1.72(03)	1.16(07)	1.04	−0.65
14	−66.31	8.81(18)	1.72(03)	1.16(07)	1.04	−0.65
17a	−76.10	8.60(11)	1.80(05)	1.17(04)	1.27	−0.64
17b	−76.10	8.60(11)	1.80(05)	1.17(04)	1.27	−0.64
17c	−76.10	8.60(11)	1.80(05)	1.17(04)	1.27	−0.64
17d	−76.10	8.60(11)	1.80(05)	1.17(04)	1.27	−0.64
18	−96.47	8.67(10)	1.56(04)	1.22(04)	1.94	−0.67
19	−106.54	8.73(09)	1.51(03)	1.21(03)	2.37	−0.70
20	−116.62	8.73(09)	1.43(03)	1.15(03)	2.94	−0.73
21a	−126.70	9.00(09)	1.42(03)	1.17(03)	3.51	−0.77
21b	−126.70	9.00(09)	1.42(03)	1.17(03)	3.51	−0.77
23	−135.92	8.97(10)	1.30(03)	1.20(04)	4.26	−0.79
24	−164.89	9.36(11)	1.23(02)	1.15(04)	5.75	−0.77
25	−165.22	9.36(11)	1.23(02)	1.15(04)	5.75	−0.77
26	−176.86	9.39(11)	1.20(02)	1.23(04)	5.76	−0.72
27	−196.96	9.40(12)	1.19(02)	1.15(04)	5.16	−0.59
28	−216.99	9.52(13)	1.13(02)	1.23(05)	4.40	−0.47
29	−217.29	9.52(13)	1.13(02)	1.23(05)	4.40	−0.47
30	−247.00	9.61(16)	1.10(02)	1.18(05)	3.20	−0.35

7.6 Target thickness effects

Trying to measure at pion energies below 38 MeV it became obvious that for low energies the differential measurement with solid targets was not practical anymore. For higher energies corrections for target thickness effects had to be applied also.

7.6.1 Correction for different mid target energies

Some measurements have been performed with different target thicknesses (see table 5.1). To be able to take an average, including results obtained with thin and mid targets, all cross sections were extrapolated to the target energy corresponding to thick targets. Energy loss tables and the *slope* of the SAID cross sections were used for this correction. Table 7.5 contains the original random and efficiency corrected cross section σ_{raw} and the mid-target energies and corrected cross sections σ_{thick}.

Table 7.5: *Cross sections for different target thicknesses, extrapolated to thick target thickness*

Run ID	T_{exp} [MeV]	σ_{raw} [mb]	T_{thick} [MeV]	$\delta\sigma_{\text{SAID}}$ [mb]	σ_{thick} [mb]
3a	-39.48	4.44(53)	-38.92	-0.043	4.40(53)
3b	-39.48	4.80(24)	-38.92	-0.043	4.76(24)
5	-39.72	5.67(32)	-38.92	-0.062	5.61(32)
8	-47.61	5.42(34)	-47.10	-0.052	5.37(34)
9	-47.82	7.19(42)	-47.10	-0.074	7.12(42)
14	-65.83	7.81(41)	-65.40	-0.074	7.74(41)
25	-165.11	43.03(58)	-164.78	-0.060	42.97(58)
29	-216.13	32.54(34)	-215.83	0.110	32.64(34)

7.6.2 Absorption effects at lower energies

The thicknesses of the C- and CH_2-target pairs were designed to obtain the same mid-target energies for beam pions. The different densities ($\rho_C = 1.86$ g/cm^3, $\rho_{CH_2} = 0.94$ g/cm^3) led to substantially different thicknesses (in mm). Therefore, reaction products scattered by about 90 degree had a larger solid angle to be stopped in for the CH_2-target than for the C-target. Conversely the areal density of the C-target in transverse direction was much larger than for the CH_2-target.

These effects led to absorption effects at low energies which affected the subtraction of the carbon cross sections in a complicated way. Moreover, a Monte-Carlo simulation was impossible because we lacked control over the heavy fragment formation following pion absorption in flight. As an experimental approach we measured the apparent SCX cross sections for π^+. The results are shown in table 7.6.

Table 7.6: *Results for the π^+ measurements*

Run ID	T_{exp} [MeV]	σ [mb] effi. corrected	σ_{raw} [mb] effi. rnd. corrected	σ_{thick} [mb]
4	$+39.48$	$-0.56(26)$	$-0.61(26)$	$-1.00(42)$
12	$+64.27$	$-0.42(15)$	$-0.44(15)$	$-0.44(15)$
16	$+75.09$	$-0.53(11)$	$-0.53(11)$	$-0.53(11)$
22	$+125.82$	0.02(13)	0.07(14)	0.07(14)

For the scattering on protons a zero total cross section of emerging neutrals was expected. The resulting π^+ cross sections σ_{raw} are efficiency and random corrected. It is easily seen that all other corrections do not apply. We interpreted the deviations from zero which decrease with increasing pion energy as a result of target effects. For simplicity a linear dependence of the π^+ cross sections was assumed and a linear fit yields equation 7.14. The results are shown in tables 7.7 and 7.8. From the fit function

$$\frac{\delta\sigma_{abs}}{mb} = 0.0148 \cdot \frac{E_{lab}}{MeV} - 1.5411 \tag{7.14}$$

plotted in fig. 7.10 the zero-crossing near 100 MeV can be seen. Above this energy the target absorption effects were neglected. At lower energies the value of the apparent π^+ cross section, as described by equation 7.14, was attributed to the target absorption and used in full as a correction (see tables 7.7 and 7.8). Due to the fit uncertainty and the approximation of a linear dependence the systematic error resulting from this correction is estimated to be 100 % of the correction (see Section 8.2). This correction has been determined using thick target pairs. If applied to the mid or thin targets is was simply scaled with the target thickness.

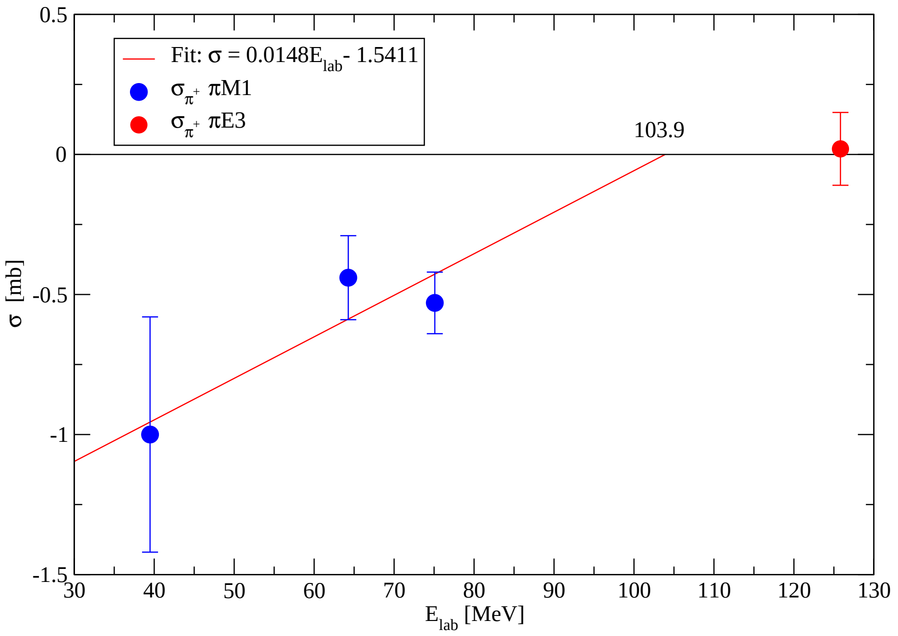

Figure 7.10: *Linear fit of the π^+ measurements*

Table 7.7: *Corrections due to target absorption effects for the πE3 channel*

Run ID	T_{exp} [MeV]	σ_{thick} [mb]	$\delta\sigma_{\text{abs}}$ [mb]	σ_{tgt} [mb]
1a	−38.92	7.02(29)	0.77	7.79(29)
1b	−38.92	7.15(16)	0.77	7.92(16)
2	+38.92	1.81(16)	0.77	2.58(16)
3a	−39.48	4.40(53)	0.48	4.88(53)
3b	−39.48	4.76(24)	0.48	5.24(24)
4	+39.48	−0.61(26)	0.48	−0.13(26)
5	−39.72	5.61(32)	0.34	6.95(32)
6	−42.99	5.33(10)	0.72	6.05(10)
7a	−47.10	5.60(17)	0.64	6.24(17)
7b	−47.10	4.96(31)	0.64	5.60(31)
8	−47.61	5.37(34)	0.41	5.78(34)
9	−47.82	7.12(42)	0.29	7.41(42)
11a	−64.27	7.19(22)	0.47	7.66(22)
11b	−64.27	6.81(16)	0.47	7.28(16)
12	+64.27	−0.44(15)	0.47	0.03(22)
15	−75.09	8.58(14)	0.34	8.92(14)
16	+75.09	−0.53(11)	0.34	−0.19(11)

Table 7.8: *Corrections due to target absorption effects for the πM1 channel*

Run ID	T_{exp} [MeV]	σ_{thick} [mb]	$\delta\sigma_{\text{abs}}$ [mb]	σ_{tgt} [mb]
10a	−55.55	6.34(22)	0.58	6.92(22)
10b	−55.55	6.41(15)	0.58	6.99(15)
10c	−55.55	4.94(71)	0.58	5.52(1.71)
13a	−65.88	7.50(17)	0.46	7.96(17)
13b	−65.88	7.02(42)	0.46	7.48(42)
13c	−65.88	6.84(76)	0.46	7.30(76)
14	−66.31	7.74(41)	0.28	8.02(41)
17a	−76.10	8.73(24)	0.34	9.07(24)
17b	−76.10	9.92(20)	0.34	10.26(20)
17c	−76.10	8.67(39)	0.34	9.01(39)
17d	−76.10	9.51(67)	0.34	9.85(67)
18	−96.96	14.92(25)	0.10	15.02(25)

Chapter 8

Estimation of errors

One of the important aspects of this experiment was to achieve a measurement with high statistical accuracy. To ensure the success for the low energy part of the experiment with the relatively small cross sections a substantial time for data taking was necessary. Furthermore a very careful treatment of the systematic errors was required to comply with the accuracy required. This chapter deals with the calculation of the *statistical* and *systematic* uncertainties.

8.1 Statistical errors

As pointed out in Section 3.3 the transmission T for each target is given by

$$T \ = e^{-\alpha\ \sigma} \tag{8.1}$$

For the relative statistical error of the cross section one gets

$$\frac{\Delta\sigma}{\sigma} = -\frac{1}{logT}\frac{\Delta T}{T}. \tag{8.2}$$

N as the number of trigger events (*beam events*) is not subject to statistical fluctuations. Rather the number of SCX events $N(1-T)$ (outgoing neutrals) is assumed to underly the Poisson statistics with one standard deviation as error:

$$\Delta(N(1-T)) = \sqrt{N(1-T)} \tag{8.3}$$

The left hand side of equation 8.3 can be written as

$$\Delta(N(1-T)) = \Delta N(1-T) - N\Delta T = N\Delta T \tag{8.4}$$

Therefore

$$\frac{\Delta T}{T} = -\frac{1}{TN}\sqrt{N(1-T)} = -\frac{1}{T}\sqrt{\frac{1-T}{N}} \tag{8.5}$$

Then the resulting statistical error from equation 8.2 follows as

$$\frac{\Delta\sigma}{\sigma} = -\frac{1}{logT}\frac{\sqrt{1-T}}{T\sqrt{N}} \tag{8.6}$$

Due to losses in air and in the last beam defining counter the real expression for the transmission through a target is

$$T \ = T_0 e^{-\alpha\ \sigma} \tag{8.7}$$

where T_0 is the empty transmission, which was not unity (compare Section 3.3). The empty transmission T_0 was measured in the same way as T and based on equation 8.7 the relative error in the cross section becomes

$$\frac{\Delta\sigma}{\sigma} = \frac{1}{logT_0 - logT}\sqrt{\frac{1-T_0}{N_0 T_0^2} + \frac{1-T}{NT^2}}. \tag{8.8}$$

The total SCX cross section was extracted from the cross sections for the C- and CH_2-targets by applying

$$\sigma_H = \frac{1}{2}(\sigma_{CH_2} - \sigma_C). \tag{8.9}$$

A slight complication that arises because of our sequence of measurements is that the cross sections of the CH_2- and C-targets contain the same empty transmission measurement and therefore are not statistically independent. Taking the statistical dependence into account the relative error for the π^-p SCX cross section becomes

$$\frac{\Delta\sigma_H}{\sigma_H} = \frac{\sqrt{(\frac{1}{\alpha_{CH_2}T_{CH_2}})^2\frac{(1-T_{CH_2})}{N_{CH_2}} + (\frac{1}{\alpha_C T_C})^2\frac{(1-T_C)}{N_C} + (\frac{1}{\alpha_C} - \frac{1}{\alpha_{CH_2}})^2\frac{1}{T_0^2}\frac{(1-T_0)}{N_0}}}{\frac{logT_{CH_2}}{\alpha_{CH_2}} - \frac{logT_C}{\alpha_C} - logT_0(\frac{1}{\alpha_{CH_2}} - \frac{1}{\alpha_C})} \tag{8.10}$$

Another source of statistical errors are the Monte Carlo simulations. The statistical errors of the simulations depend on the number of simulated events and are also subject to Poisson statistics. As an example the correction due to muon contamination (see Section 7.4.2) is obtained from

$$\kappa_\mu = \frac{N_\mu}{N_\mu + N_\pi}.$$

The resulting statistical error is

$$\delta\kappa_\mu = \frac{\sqrt{N_\mu}}{N_\mu + N_\pi}.$$

Note that the number of triggers ($N_\mu + N_\pi$) is not subject to statistical uncertainties. The Monte Carlo corrections were directly applied to the cross sections by multiplying the cross section with the calculated fraction of muons

$$\sigma_{\mu_{corr}} = \frac{\sigma_{av}}{1 - \kappa_\mu}.$$

Gaussian error propagation was used to arrive at the final statistical error

$$\delta\sigma_{\mu_{corr}} = \sqrt{\left(\frac{\delta\sigma_{av}}{1-\kappa_\mu}\right)^2 + \left(\frac{\sigma_{av}\cdot\delta\kappa_\mu}{(1-\kappa_\mu)^2}\right)^2}.$$

8.2 Systematic errors

The estimation of the systematic uncertainties, notably with respect to the problem of the target effects at lower energies, is very delicate. The following sources of systematic uncertainties were investigated:

Target absorption effects

The uncertainties arising from the target effects are the dominant errors up to a pion energy of about 75 MeV. The problem of the target effects is pointed out in Section 7.6.2. Within the target errors the contribution that results from absorption is the dominant contribution up to ≈ 100 MeV. Due to the large uncertainties in obtaining the absorption correction the error is taken to be 100 % of the correction itself.

Target thickness

The target thicknesses were obtained from weight and area measurements (see Section 4.4). As may be seen from table 4.3 the resulting uncertainties are well below 1 ‰, even if we account for an additional uncertainty of the effective thickness through the target angle. The uncertainty of the target angle is estimated to be about 3°. Therefore the contribution of the target thickness to the total error is negligible. From direct thickness measurements performed with a micrometer gage at 14 different points on the surface of each target the very good homogeneity of the targets could be confirmed. The uncertainty in the homogeneity achieved from this measurements was 1.3 ‰ for the thick CH_2-target and 1.1 ‰ for the thick C-target which were mostly used.

Random correction

In Section 7.2 the correction due to random effects is discussed. The systematic error in the random correction is generously estimated to be 30 % of the correction and is listed in tables 8.1 and 8.2.

Detector threshold

The analysis is based on events exceeding assumed thresholds in the detector QDCs (compare Section 6.5). To get an estimation of the uncertainty emerging from the applied thresholds, for each analysis, a set of 40 different thresholds were applied and the results calculated. Figs. 8.1 show the results for different thresholds in the back and up counters. The threshold applied in final analysis is marked.

As discussed in Section 6.5 the QDC threshold was set in the minimum between the pedestal and the ΔE-peak. The *QDC channels* on the abscissa start with the pedestal at index 0 (pedestal substracted). The systematic errors were obtained from the variation of the SCX cross section resulting from variation of that threshold location. The systematic errors for the back counter threshold were (arbitrarily) taken from a typically ± 22 % variation, for the side counters a ± 9 % variation was used. The smaller correction in the side counters originates from the different spectral shape in the side counters (compare fig. 6.4).

The results of the systematic errors are listed in the tables 8.1, 8.2. The errors were always summed in quadrature.

Monte Carlo simulation

In addition to statistical errors the corrections obtained from the Monte Carlo simulation also are subject to systematic errors. The main contribution here emerges from the uncertainty due to the detection of the neutrons (applied correction: $1-4$ %) and the slightly different results between GEANT3 and GEANT4 for the detection of electromagnetics (applied correction: $6-8$ %). Dalitz decay (applied correction: 1.2 %) as well as the muon contamination of the beam (applied correction: $2.3-1.1$ %) are well under control and in good agreement between GEANT3 and GEANT4. Due to the problematic hadronic correction at low energies, the error of the MC simulation is estimated as 1 % of the total SCX cross section up to 47 MeV and as 0.5 % above this. These estimates also take into account GEANT3 and GEANT4 simulations with different threshold cuts in the detector spectra. The applied errors are listed in tables 8.1 and 8.2.

Radiative capture

The radiative capture correction is obtained by using the inverse photo production reaction as explained in Section 7.5. From the most accurate direct measurements done by Salomon and Bagheri from 27 MeV up to 121 MeV [Sal84], [Bag88a] it can be seen that for energies above 40 MeV the error in the radiative capture cross section is less than 6 % of the $\pi^- p \to n\gamma$ cross section. The interpolation from the inverse photo production is straightforward and for higher

Table 8.1: *Summary of errors for the πE3 channel*

Run ID	abs. [mb]	rnd. [mb]	thresh. back [mb]	thresh. side [mb]	MC [mb]	rad. [mb]	$\delta\sigma_{sys}$ [mb]	$\delta\sigma'_{sys}$[a] [mb]	$\delta\sigma_{stat}$ [mb]	$\delta\sigma_{\text{tot}}$ [mb]	$\delta\sigma'_{\text{tot}}$[b] [mb]
1a	0.77	0.02	0.03	0.18	0.05	0.07	0.80	0.20	0.29	0.85	0.35
1b	0.77	0.02	0.15	0.25	0.05	0.07	0.83	0.31	0.16	0.84	0.34
3a	0.48	0.04	0.09	0.01	0.05	0.07	0.50	0.13	0.53	0.73	0.55
3b	0.48	0.01	0.06	0.24	0.05	0.07	0.55	0.26	0.24	0.60	0.36
5	0.34	0.01	0.12	0.11	0.05	0.07	0.39	0.18	0.32	0.50	0.37
6	0.72	0.01	0.14	0.12	0.06	0.07	0.75	0.21	0.10	0.76	0.23
7a	0.64	0.01	0.20	0.28	0.06	0.07	0.73	0.37	0.17	0.75	0.40
7b	0.64	0.01	0.11	0.02	0.06	0.07	0.66	0.15	0.31	0.73	0.34
8	0.41	0.01	0.02	0.25	0.06	0.07	0.49	0.27	0.34	0.60	0.43
9	0.29	0.01	0.31	0.15	0.06	0.07	0.46	0.36	0.42	0.62	0.55
11a	0.47	0.01	0.13	0.09	0.04	0.07	0.50	0.18	0.22	0.55	0.28
11b	0.47	0.01	0.06	0.17	0.04	0.07	0.51	0.20	0.16	0.53	0.25
15	0.34	0.02	0.06	0.13	0.05	0.06	0.38	0.16	0.14	0.40	0.22

[a] $\delta\sigma'_{sys}$: Systematic error without the error due to absorption effects ('abs.')

[b] $\delta\sigma'_{tot}$: Total error without the error due to absorption effects

Table 8.2: *Summary of errors for the πM1 channel*

Run ID	abs. [mb]	rnd. [mb]	thresh. back [mb]	thresh. side [mb]	MC [mb]	rad. [mb]	$\delta\sigma_{sys}$ [mb]	$\delta\sigma'_{sys}$[a] [mb]	$\delta\sigma_{stat}$ [mb]	$\delta\sigma_{\text{tot}}$ [mb]	$\delta\sigma'_{\text{tot}}$[b] [mb]
10a	0.58	0.08	0.03	0.08	0.03	0.07	0.60	0.14	0.22	0.64	0.26
10b	0.58	0.10	0.06	0.10	0.03	0.07	0.61	0.17	0.15	0.62	0.23
13a	0.46	0.12	0.17	0.06	0.04	0.07	0.52	0.23	0.17	0.54	0.29
13b	0.46	0.14	0.13	0.17	0.04	0.07	0.53	0.27	0.42	0.68	0.50
13c	0.46	0.17	0.02	0.04	0.04	0.07	0.50	0.19	0.76	0.91	0.78
14	0.28	0.10	0.03	0.07	0.04	0.07	0.32	0.15	0.41	0.52	0.44
17a	0.34	0.17	0.32	0.18	0.05	0.06	0.53	0.41	0.24	0.59	0.48
17b	0.34	0.32	0.37	0.19	0.05	0.06	0.63	0.53	0.19	0.66	0.56
17c	0.34	0.10	0.14	0.05	0.05	0.06	0.39	0.20	0.39	0.55	0.44
17d	0.34	0.01	0.13	0.06	0.05	0.06	0.38	0.16	0.67	0.77	0.69
18	0.10	0.08	0.13	0.14	0.08	0.07	0.25	0.23	0.25	0.36	0.34
19	0.00	0.15	0.24	0.21	0.09	0.07	0.37	0.37	0.26	0.45	0.45
20	0.00	0.10	0.11	0.09	0.12	0.07	0.22	0.22	0.19	0.29	0.29
21a	0.00	0.10	0.15	0.07	0.13	0.08	0.25	0.25	0.41	0.48	0.48
21b	0.00	0.28	0.64	0.20	0.13	0.08	0.74	0.74	0.38	0.83	0.83
23	0.00	0.08	0.18	0.22	0.17	0.08	0.35	0.35	0.25	0.43	0.43
24	0.00	0.08	0.08	0.18	0.22	0.08	0.32	0.32	0.42	0.53	0.53
25	0.00	0.08	0.06	0.21	0.22	0.08	0.33	0.33	0.58	0.67	0.67
26	0.00	0.08	0.29	0.14	0.22	0.07	0.40	0.40	0.28	0.49	0.49
27	0.00	0.07	0.15	0.16	0.19	0.06	0.31	0.31	0.26	0.40	0.40
28	0.00	0.06	0.08	0.19	0.16	0.05	0.27	0.27	0.28	0.39	0.39
29	0.00	0.07	0.01	0.14	0.16	0.05	0.23	0.23	0.34	0.41	0.41
30	0.00	0.07	0.11	0.10	0.12	0.04	0.21	0.21	0.21	0.30	0.30

[a] $\delta\sigma'_{sys}$: Systematic error without the error due to absorption effects

[b] $\delta\sigma'_{tot}$: Total error without the error due to absorption effects

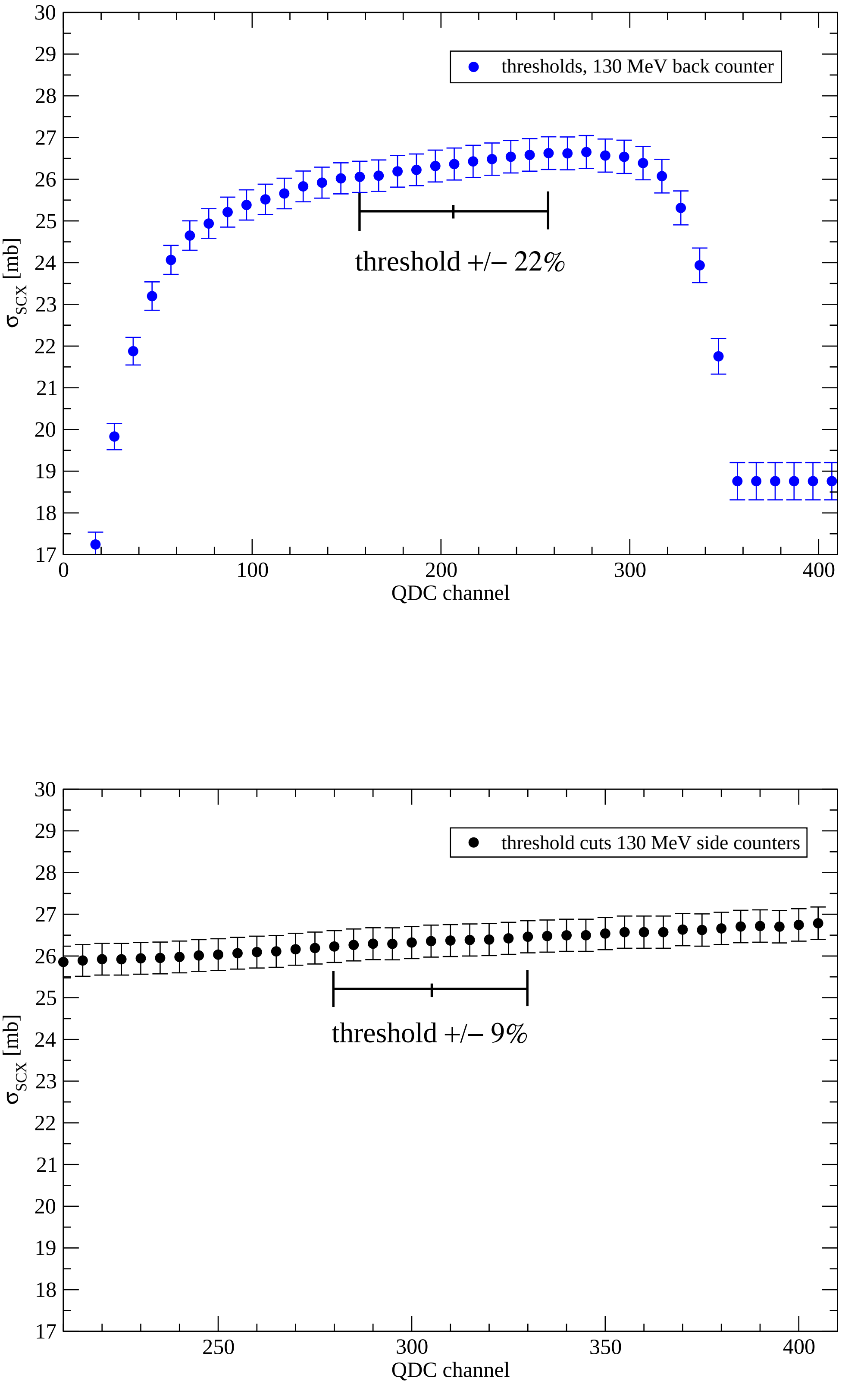

Figure 8.1: *Total cross section for various thresholds in the back (top) and side (bottom) counters for Run number 21b (130 MeV, high rate). The QDC channels are plotted after subtraction of the pedestal.*

energies there are a rich number of older references and the importance of the capture reaction decreases. An assumed systematic error of 10 % of the applied correction is very liberal and therefore the capture reaction does not pose a problem on the level of an SCX accuracy of $1-2$ %. The tables 8.1 and 8.2 summarize the applied errors.

Chapter 9

Experimental tests

During the beam times various tests of the experimental setup were performed to check the function of the detectors and the basic principle of the experiment. These tests are presented in this chapter.

9.1 π^+ tests

An obvious and simple test of the experimental accuracy is the π^+ test. Since no charge exchange is possible in the π^+p channel the resulting cross section must be zero. A positive pion beamline transports, in addition to π^+-particles, protons, μ^+- and e^+-particles of the same momentum. The TOF spectrum of the S3 counter for positively charged particles looks similar to the TOF spectrum of negatively charged channel shown in fig. 6.2. The only difference are the different fluxes of the various particle types. For a given flux of the primary proton beamline the flux of a π^+ beam is approximately five times higher than the π^- beam flux.

The analysis of the π^+ measurements follows the principle of the π^- data which is firstly, to get a good beam definition, secondly, the identification of the transmitted pions for the three different target settings and finally, the skimming procedure. Efficiency and random corrections have to be applied in the same manner as for the π^-. No further corrections due to the detection of neutrals or the radiative capture are necessary.

The expected SCX cross section on hydrogen is zero. The π^+ test has been performed at 38.92, 39.48, 64.27, 75.09 and 126.70 MeV. Roughly the cross section for production of neutrals for C and CH_2 is found to be 5 to 8 times smaller for π^+ beams than for π^- beams (see fig. 3.2). The results are listed in table 7.6. As the energies become lower the more the obtained results tend towards negative values. The reason of this trend is probably the target thickness effect at lower energies described in Section 7.6. The π^+ results were used to correct for the target effects described (see Section 7.6).

9.2 e^- and μ^- tests

The recorded events which fulfilled the beam definition condition also include muons and electrons of the channel momentum. In the analysis cuts on these particle types could be applied in the TOF spectrum (see fig. 6.2) in the same way as it was done for pions. The total cross sections for disappearing charged particles for electrons and muons was then extracted. Unfortunately, the statistics for the muons are poor due to their scarcity. In many cases the parasitic electron measurements were rendered impossible because a hardware veto on electrons was required to reduce the amount of data. Therefore, only a few useful cases were analyzed (see table 9.1). As with the π^+ test a zero cross section for outgoing neutrals was expected once the extracted cross sections were corrected for efficiency and random effects. Indeed table 9.1 shows zero results within two standard deviations which is quite satisfactory.

Table 9.1: *Results for total cross sections for electrons and muons*

Run ID	particle type	T_{exp} [MeV]	σ_{raw} [mb] effi. rnd. corrected
21b	e^-	−124.10	0.00(03)
23	e^-	−134.42	0.03(02)
21b	μ^-	−126.10	−0.11(18)

9.3 Beam rate tests

For energies below 80 MeV the SCX cross section becomes small. The πM1 channel was constructed as a high energy channel. To get enough statistics within a reasonable time the beam rate was raised by opening the slits in the beam line. To be able to evaluate the influence of the increased beam rate, runs with various beam rates have been recorded at 65.88, 76.10 and 126.70 MeV. The results of these tests are shown in table 9.2.

Table 9.2: *Results for total cross sections for different beam rates*

Run ID, rate	trigger [kHz]	single rate back counter [MHz]	T_{exp} [MeV]	σ [mb] effi. corrected	σ_{raw} [mb] effi. rnd. corrected
13a/b high	3.8	1.0	−65.88	7.02(14)	7.43(16)
13c low	2.9	0.7	−65.88	6.26(74)	6.84(76)
17a/b/c high	4.2	1.0	−76.10	8.57(13)	9.36(13)
17d low	1.7	0.3	−76.10	9.53(67)	9.51(67)
21b high	7.9	0.7	−126.70	25.44(38)	26.36(38)
21a low	5.0	0.2	−126.70	27.03(41)	27.25(41)

Unfortunately only the rate test at 126.70 MeV had approximately the same statistics for a reasonable estimation of the beam rate effects. After applying the random corrections the results of the runs with different beam rates agree within the statistical errors.

9.4 Tests with different target thicknesses

An important test of the target influence were the measurements with different target thicknesses. There were three different target sets available (see table 4.3). Due to the limited beam time and the importance of getting high statistics only the middle and thick targets were used in the πM1 beam line at 65.88, 164.89 and 216.99 MeV. In the πE3 channel measurements with the thin, middle and thick targets were taken at 38.92 and 47.10 MeV. Corrections for target thickness effects (see Section 7.6) have been applied. Tables A.1 and A.2 show the obtained results. For the sake of comparison all cross sections were plotted for energies corresponding to the mid-target energies of the thick targets. The necessary corrections for the cross sections were made adopting the slope of the SAID FA02 solution (see Section 7.6.1).

The obtained cross sections for the different thicknesses are listed in table 9.3 and agree with each other for the energies from 65.88 MeV and higher. The specified errors are statistical errors. For the lower energies it turns out that the determined cross sections do not agree and are influenced by target effects as discussed in Section 8.2. The results from table 9.3 are illustrated in fig. 9.1. The percent deviation of the cross sections determined with the thick (red triangles), mid (blue diamonds) and thin target (green circles) to those determined with the mid target are plotted. At high energies the agreement between the measurements with thick and mid targets is close to perfect. At low energies the discrepancies are obvious. The deviation of the SCX values for the thin targets may be of statistical nature. The three sigma deviation of the thick target results for 38 MeV is considered to be related to the target absorption. This

Table 9.3: *Cross sections for different target thicknesses, extrapolated to the thickness of the thick target. Only statistical errors are given.*

Target	T_{exp} [MeV]	σ_{thick} [mb]
thick	38.92	7.12(14)
mid	38.92	4.70(22)
thin	38.92	5.61(32)
thick	47.10	5.45(15)
mid	47.10	5.37(34)
thin	47.10	7.12(42)
thick	65.88	7.43(16)
mid	65.88	7.74(41)
thick	164.89	43.28(42)
mid	164.89	42.97(56)
thick	216.99	32.57(28)
mid	216.99	32.64(43)

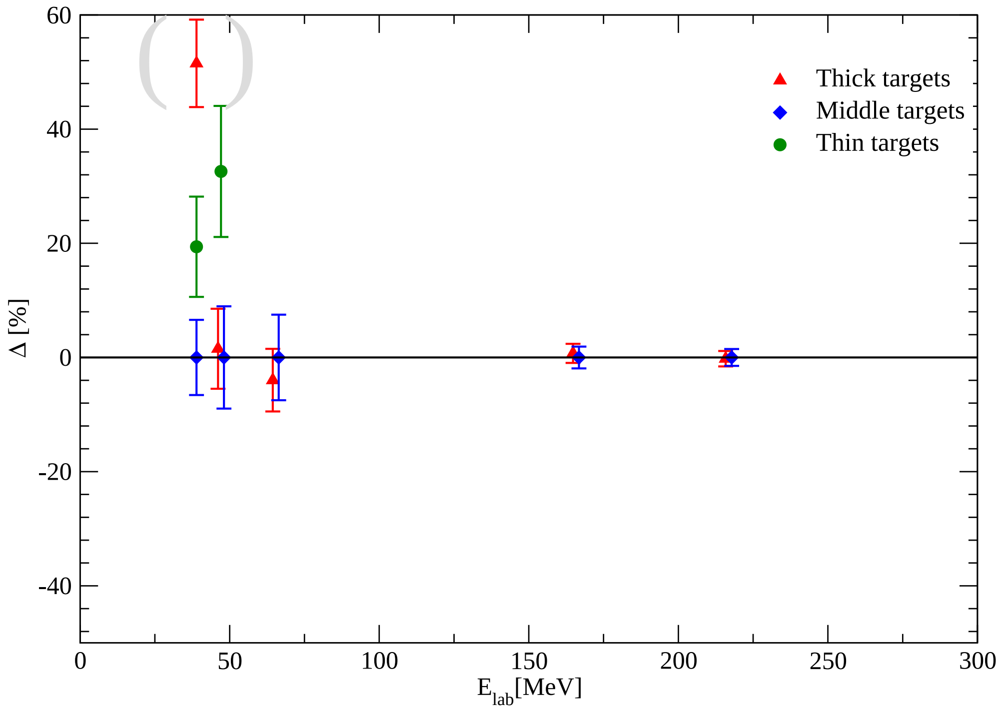

Figure 9.1: *Ratio plot of the total SCX cross section for the various target thicknesses used. The percent deviation Δ of the cross sections from values obtained with the mid targets is plotted. Only statistical errors of Δ obtained using error propagation are given.*

measurement was not included in the final results, while all others were included in the average. We emphasize that all values agree when total errors are used instead of statistical errors only.

Chapter 10

Results and discussion

In this chapter the final results for the total SCX cross sections are shown (Section 10.1). The results presented include SCX cross sections of 38 to 250 MeV incident pion energy. In Section 10.2 the results are discussed and compared to data from previous experiments and the SAID FA02 solution. A proposal of how to treat the results and to obtain a first estimation of the isospin breaking is presented in Section 10.3.

10.1 Total SCX cross sections

Fig. 10.1 shows the total SCX cross sections together with the predictions of the partial wave analysis SAID FA02 and the KH80. Results of this experiment are shown for 18 different incident pion energies between 38 and 250 MeV, distinct for the pion channels used. The cross sections from energies with several runs and the various subdivided runs were properly averaged and the MC and radiative capture corrections were applied after the weighted averaging. The inner error bars (blue and red) show the statistical errors while the outer error bars (black) display the total errors. The latter result from the quadratic addition of the statistical and systematic errors which were discussed in Chapter 8. The data have errors of about 2 % except for low energies (< 76 MeV). The main contribution to the errors at lower energies arises from the use of solid targets (see Section 8.2). The two overlapping data points for the two different pion channels used agree within the errors. The high energy beamline πM1 has different beam characteristics and quality than the πE3 channel and with the πM1 channel the low energy data were taken with a high beam rate which led to a major random correction (see Section 7.2). In fig. 10.2 the comparison of the data with other experiments and the SAID FA02 predictions is shown. Tables 10.1 and 10.2 list the results of this work. The corrections applied to the raw data were described in Chapter 7.1. Our results cover a larger energy range than any previous experiment and the errors are comparable to those of the most precise previous experiment (in Section 10.2.1).

Table 10.1: *Final results for the πE3 channel*

T_{thick} [MeV]	σ_{av} [mb]	MC corr. [mb]	rad. corr. [mb]	$\delta\sigma_{stat}$ [mb]	$\delta\sigma_{sys}$ [mb]	$\delta\sigma'_{sys}$ [a] [mb]	$\delta\sigma'_{tot}$ [b] [mb]	σ_{final} [mb]	$\delta\sigma_{tot}$ [mb]
38.92	5.42(19)	0.90(12)	−0.74	0.23	0.49	0.22	0.31	5.58	0.54
42.99	6.05(10)	0.97(06)	−0.72	0.12	0.75	0.21	0.24	6.31	0.76
47.10	6.17(13)	0.93(08)	−0.69	0.15	0.66	0.31	0.34	6.41	0.68
64.27	7.41(13)	1.03(07)	−0.65	0.15	0.51	0.19	0.24	7.79	0.53
75.09	8.92(14)	1.17(08)	−0.64	0.16	0.38	0.16	0.23	9.44	0.41

[a] $\delta\sigma'_{sys}$: Systematic error without the error due to absorption effects

[b] $\delta\sigma'_{tot}$: Total error without the error due to absorption effects

Table 10.2: *Final results for the $\pi M1$ channel*

T_{thick} [MeV]	σ_{av} [mb]	MC corr. [mb]	rad. corr. [mb]	$\delta\sigma_{stat}$ [mb]	$\delta\sigma_{sys}$ [mb]	$\delta\sigma'_{sys}$ [a] [mb]	$\delta\sigma'_{tot}$ [b] [mb]	σ_{final} [mb]	$\delta\sigma_{tot}$ [mb]
55.550	6.96(12)	0.99(07)	−0.67	0.14	0.60	0.16	0.21	7.28	0.62
65.882	7.89(15)	1.04(08)	−0.65	0.17	0.49	0.22	0.28	8.29	0.52
76.100	9.71(14)	1.27(08)	−0.64	0.16	0.56	0.44	0.47	10.34	0.58
96.465	15.02(25)	1.94(13)	−0.67	0.28	0.25	0.23	0.36	16.29	0.38
106.881	18.29(26)	2.37(14)	−0.70	0.29	0.37	0.37	0.47	19.96	0.47
116.624	23.05(19)	2.94(10)	−0.73	0.22	0.22	0.22	0.31	25.25	0.31
126.696	26.77(28)	3.51(15)	−0.77	0.32	0.51	0.51	0.60	29.51	0.60
136.765	32.91(25)	4.26(14)	−0.79	0.29	0.35	0.35	0.45	36.38	0.45
164.887	43.17(34)	5.75(19)	−0.77	0.39	0.32	0.32	0.51	48.14	0.51
176.857	42.95(28)	5.76(17)	−0.72	0.32	0.40	0.40	0.51	47.99	0.51
196.956	38.77(26)	5.16(15)	−0.59	0.30	0.31	0.31	0.43	43.34	0.43
216.994	32.60(22)	4.40(13)	−0.47	0.26	0.25	0.25	0.36	36.53	0.36
247.001	23.69(21)	3.20(12)	−0.35	0.24	0.21	0.21	0.32	26.53	0.32

[a] $\delta\sigma'_{sys}$: Systematic error without the error due to absorption effects

[b] $\delta\sigma'_{tot}$: Total error without the error due to absorption effects

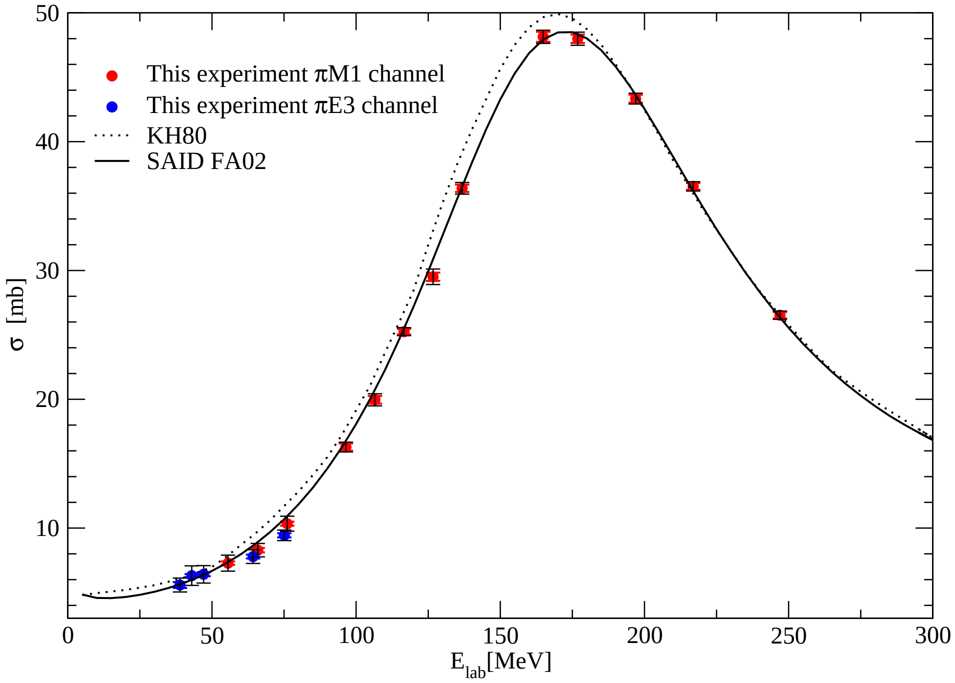

Figure 10.1: *SCX cross sections: shown are the results of this experiment (filled circles) with the total error compared to the SAID FA02 solution (black solid line) and the KH80 predictions (black dotted line).*

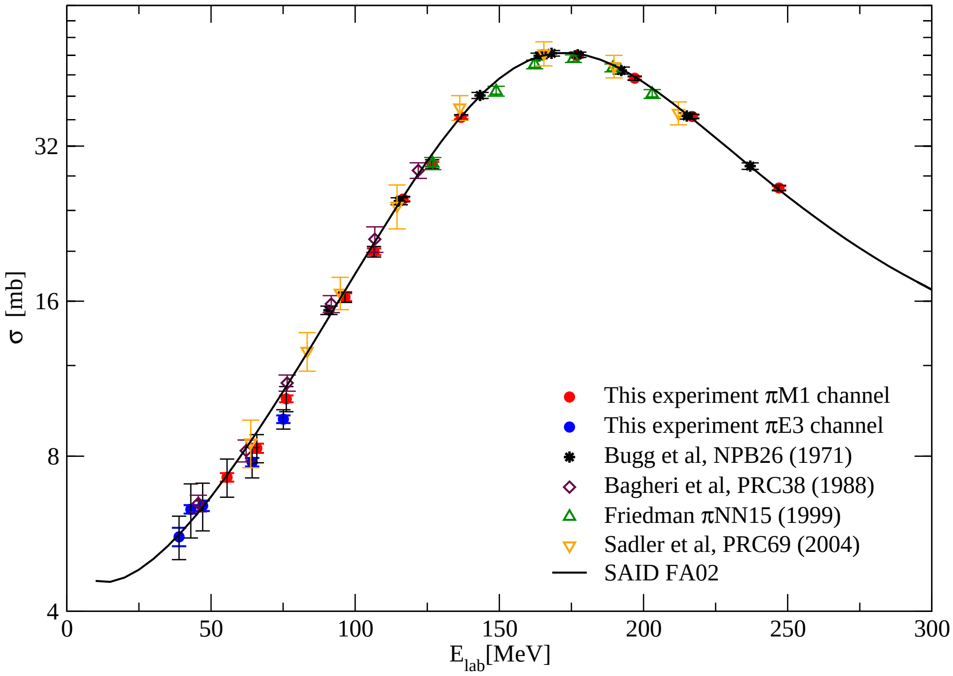

Figure 10.2: *SCX cross sections compared to other experiments: shown are the results of this experiment (filled circles) compared to other transmission experiments from Friedman et al. (triangles up) and Bugg et al. (stars) and the differential measurements from Sadler et al. (triangles down) and Bagheri et al. (diamonds). The SAID FA02 solution is represented by the black solid line.*

10.2 Discussion

10.2.1 Comparison to previous results

The comparison with previous measurements can be made with the help of fig. 10.2. The data show good agreement with the data of Bugg et al. [Bug71], taken as a transmission measurement with a liquid hydrogen target. The latest published data from Sadler et al. [Sad04] also show good agreement with our results over the whole energy range, but these data have too large errors, in order to give serious constraints on the cross section. The results from the TRIUMF measurement of Friedman et al. [Fri93], which were taken as a transmission experiment using the same targets as we tend to be slightly lower by close to 3 %. The detector setup was quite similar to ours except that the used scintillators were thicker by 50 %. Therefore, in view of the report that the TRIUMF data have a typical MC correction of 5 %, in contrast to our correction of ≈ 9 %, it is likely that the simple MC correction of the TRIUMF experiment was an underestimation [Fri05].

An expanded view of the low energy region is given in fig. 10.3. The TRIUMF measurements of Salomon et al. [Sal84] and Bagheri et al. [Bag88a] were taken with a liquid hydrogen target as differential measurements using the same NaJ-detector. The data of Bagheri et al. tend to be slightly higher than our measurements. The data of Salomon et al. agree perfectly with our data. Other available data such as the measurements of Comiso et al. [Com75], which was a measurement over the delta resonance with large errors and a single data point at 96.6 MeV from Frank et al. [Fra67], a differential measurement as well, are in full agreement with our measurements (not shown in the plots).

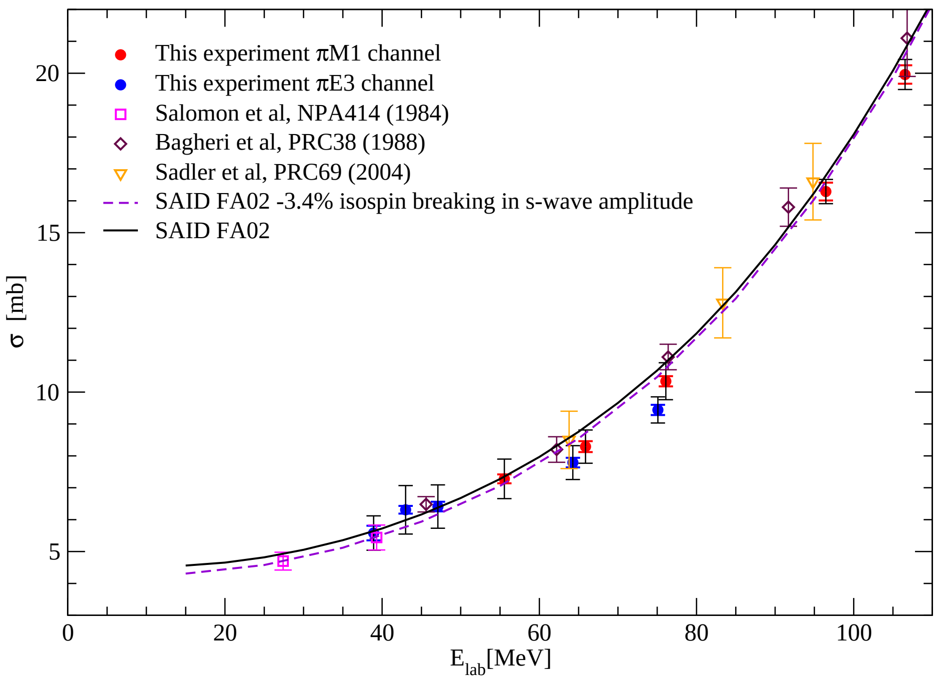

Figure 10.3: *SCX cross sections compared to other experiments at low energies: shown are the results of this experiment (filled circles) compared to differential measurements from Sadler et al. (triangles), Bagheri et al. (diamonds) and Salomon et al. (squares). The SAID FA02 solution is plotted as black solid line. The dashed line results from a 3.4 % reduction of the s-wave amplitude due to isospin breaking, as it results from a fit to the low energy data (< 107 MeV) if we include the data from refs. [Bag88a], [Sal84].*

10.2.2 Comparison to partial wave predictions

Fig. 10.1 shows our results together with the KH80 and the SAID FA02 predictions. Above 80 MeV there is an excellent agreement with the SAID FA02 phase shift analysis. The results for 76.10, 75.09, 65.88 and 64.27 MeV are below the SAID prediction and deviate from the predictions by $1 - 1.5$ standard deviations, even though the errors for these energies are larger than for the higher energies. The two data points at 75.09 and 64.27 MeV, taken at the low energy channel πE3 are even lower than the high rate results at 76.10 and 65.88 MeV measured at the πM1 beamline. For energies below 60 MeV our results again agree with the SAID prediction. Up to 170 MeV our results are evidently below the KH80 predictions. Only at energies below 60 MeV do the KH80 predictions agree with our measurements. The data by Bugg et al. also differs from the KH80 solution. This underlines the deficiencies observed by us.

10.3 Estimation of the resulting isospin breaking

The objective of this thesis was to check the reported isospin [GAK95], [Mat97b] violation of the order of 7 % in the s-wave amplitude. The basic assumption underlying our analysis is that the SCX cross section predicted by SAID is derived from the $\pi^{\pm}$p elastic scattering cross sections using the isospin triangle relation, thus corresponding to $A_0^{elastic}$ (see Section 2.1). This is only approximately true since the small amount of SCX data that currently exists may have influenced the SAID amplitudes to a small extent. It is safe to assume that the large amount of elastic scattering data will have dominated the phase shift analysis. Hence a comparison of our results with the SAID prediction effectively constitutes a test of the triangle relation (equation 2.4). The basis for our estimates are the representation of the total SCX cross section by s- and p-wave amplitudes as given in equation 2.13. For the application we used the amplitudes as given by SAID[1] (see Appendix B). In order to account for isospin breaking effects we introduced variations of amplitudes in (1) the s-wave, (2) the p_{33}-wave and (3) both.

10.3.1 s-wave model for the low energies

To obtain the SCX cross section with the s-wave amplitudes S_{31} and S_{11} modified by isospin breaking (real and imaginary part) equation 2.13 was used. We refer to this as the s-wave model. To study the effect of a s-wave variation we introduce a normalization factor f by

$$\sigma_s(f) = |S_{11} - S_{31}|^2 f^2 C \tag{10.1}$$

with

$$C = \frac{2 \cdot 4\pi}{9 \cdot k_i^2}\frac{k_f}{k_i}. \tag{10.2}$$

The cross section with the modified s-wave amplitudes then is calculated as

$$\begin{aligned}\sigma_{SAID}(f) &= \sigma_{SAID} + [\sigma_s(f) - \sigma_s(f=1)] \\ &= \sigma_{SAID} + (f^2 - 1)\sigma_s(f=1)\end{aligned} \tag{10.3}$$

σ_{SAID} is the total SCX cross section as provided by the SAID web page which is a better complete description than equation 2.13. This way we keep as much as possible of the genuine SAID cross section and vary only its s-wave part. As shown in fig. 2.4 the cross section is sensitive to the s-wave amplitudes at low energies. Therefore as a first step we fitted the normalization f to the data up to 106.54 MeV.

The cross section $\sigma_{SAID}(f)$ has been calculated for values of f from 0.86 to 0.98 for the energies below 106.54 MeV. For each value of f and each experimental data point i the χ^2 was calculated. Then the sum of χ_i^2 for all data points i up to 106.54 MeV was calculated as well as the reduced chi square (χ^2_{red}):

$$\chi^2 = \sum_i \chi_i^2 \tag{10.4}$$

$$\chi^2_{red} = \frac{\chi^2}{\text{number of data points - number of parameters}} \tag{10.5}$$

χ^2 plotted versus $(f-1)$ gives a parabola. The results are plotted in fig. 10.4. The smallest χ^2 is obtained for f =0.919 ± 0.022 if the *total* errors are used in the calculation. If we interpret the deviation from f =1 as a result of isospin breaking this suggests an isospin breaking of (-8.1 ± 2.2)%. In fig. 10.5 the data from this experiment are plotted with the SAID FA02 predictions and the SAID predictions with a -8.1 % variation of the s-wave amplitude. With the Bagheri and Salomon results included this values drops to -3.4 ± 1.3 % which shows large

---

[1] We are greatful to I. Strakowski for providing us with the list of amplitudes with a higher precision than available from the SAID web page

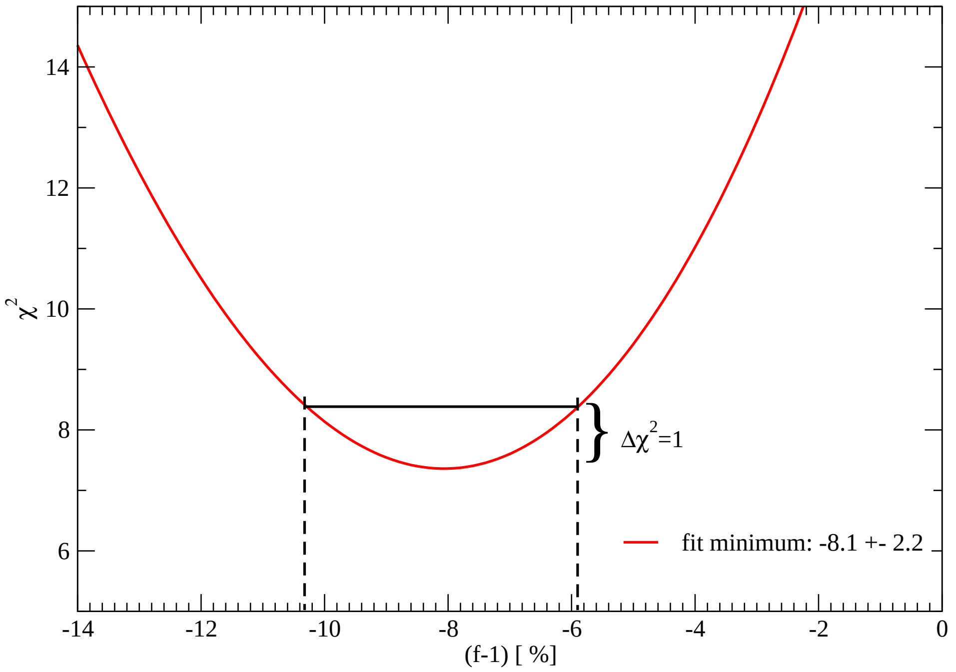

Figure 10.4: *χ^2 versus f-1 for data ranging from 38 to 107 MeV using the total error for the data points*

sensitivity to the experimental results. At a first glance this result seems to support the reported 7 % [GAK95], [Mat97b] effects. However the reduction of the s-wave amplitudes deteriorates the fit at high energies (black dotted line in fig. 10.8 top).

10.3.2 s-wave model for the full energy range

Next, the factor f with the smallest χ^2 was calculated for the whole energy range (38 - 250 MeV) covered by the experiment. Equations 10.3, 10.4 and 10.5 were used for all the measured data points as well as the measured data points plus the Salomon and Bagheri results. The resulting $(f-1)$ and the corresponding χ^2 and χ^2_{red} are shown in table 10.3 in the row "s-wave $38-250$ MeV". It is obvious that a modification of the s-wave amplitude by $(-4.4 \pm 1.4)\%$ results in a much better agreement of the model with the data than the unmodified model. It comes as no surprise that the apparent isospin breaking is smaller if the full energy range is included, since fig. 2.4 shows that s-waves hardly contribute above 100 MeV, since (see fig. 10.1) the fit to the SAID predictions is already very good.

10.3.3 p-wave model

Another, similar attempt, is a fit of all data but now varying the p_{33}-amplitude, which dominates the Δ-resonance. To this aim the relativistic Breit-Wigner (BW) form [Ped78]

$$\sigma_{BW}(W, W_0, \Gamma_0) = N\frac{8\pi}{k^2}\frac{W_0^2\Gamma^2}{(W_0^2 - W^2)^2 + W_0^2\Gamma^2} \tag{10.6}$$

with an energy dependent width

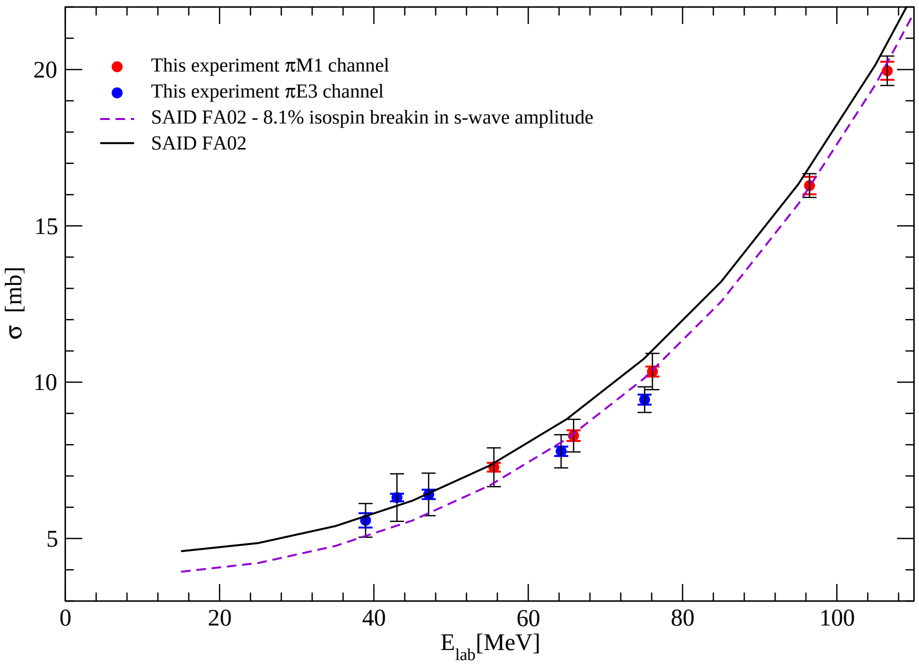

Figure 10.5: *SCX cross sections at low energies as measured in this experiment (blue and red filled circles) and as predicted by SAID FA02 with no (solid line) and a −8.1 % (dashed line) variation of the s-wave amplitude due to isospin breaking, as it results from the best fit in Section 10.3.1 to our data alone.*

$$\Gamma = \Gamma_0 (\frac{k}{k_0})^3 \frac{1 + k_0^2 a^2}{1 + k^2 a^2} \tag{10.7}$$

was used to describe the p_{33}-amplitude. We used a fixed normalization N=20/9 which exhausts the unitarity limit. Here k and W represent the pion momentum and the total πN energy in the c.m. system. In the fit W_0 (resonance energy) and the width Γ_0 were treated as free fit parameters. The reaction radius was set to $a = 1.15$ fm. For more details see [Ped78].

1st step:

We first checked that the p_{33}-amplitudes of SAID (see Appendix B) are indeed described by this Breit-Wigner form if $W_0 = 1230.8$ MeV and $\Gamma_0 = 110.7$ MeV. This was done by fitting the Breit-Wigner form of equation 10.6 to the p_{33} part of the SCX cross section

$$\sigma_{P_{33}} = 2|P_{33}|^2 \frac{2 \cdot 4\pi}{9 \cdot k_i^2} \frac{k_f}{k_i}. \tag{10.8}$$

$\sigma_{P_{33}}$ was obtained using equation 2.13 and removing the contribution of all other amplitudes. The calculation was made for pion lab energies from 15 MeV to 345 MeV in steps of 10 MeV. The excellent fit is illustrated by fig. 10.6 where the percentage deviation Δ of $\sigma_{P_{33}}$ from σ_{BW} is plotted

$$\Delta = \frac{\sigma_{P_{33}} - \sigma_{BW}}{\sigma_{BW}} \tag{10.9}$$

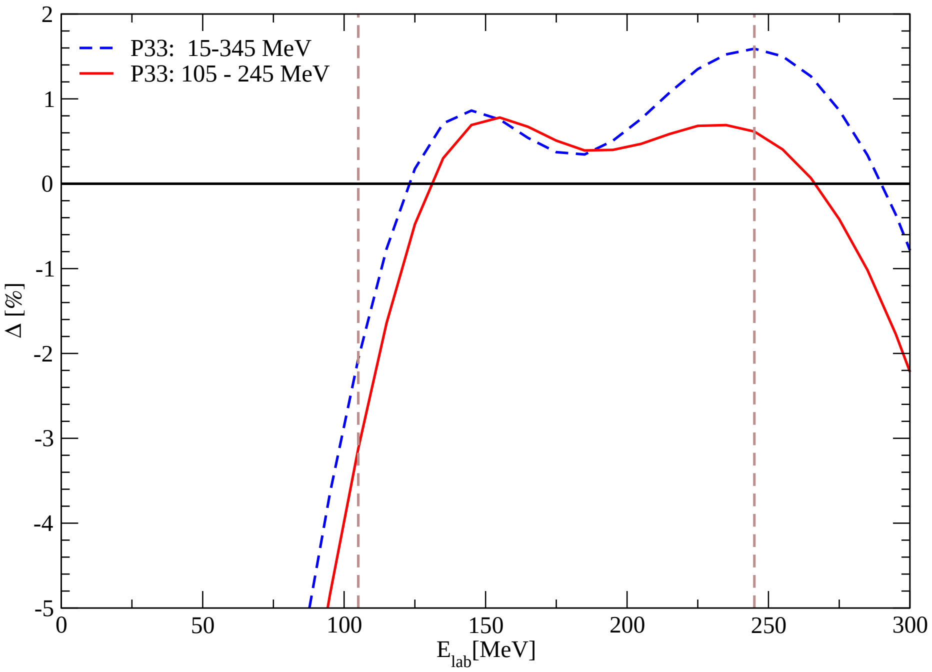

Figure 10.6: *Ratios of the fitted Breit-Wigner* σ_{BW} *and the calculated* p_{33} *part of the cross section:* $\Delta = \frac{\sigma_{P_{33}} - \sigma_{BW}}{\sigma_{BW}}$*, dashed line: ratio for the fit over the whole energy range* $15 - 345$ *MeV, solid line: ratio for the fit over the p-region from* $105 - 245$ *MeV*

Indeed, fig. 10.6 shows that the $\sigma_{P_{33}}$ cross section agrees to better than $2 \cdot 10^{-2}$ with the Breit-Wigner form within the energy region from 105 to 300 MeV (dashed blue line). In fig. 2.4 one can see that the p_{33} contribution to the total SCX cross section is dominant within the energy range of 105 to 245 MeV (referred to as p-region). Outside this region the s-wave contribution becomes more relevant. A fit of the Breit-Wigner form to $\sigma_{P_{33}}$ within this p-region gives $W_0 = 1231.1$ MeV and $\Gamma_0 = 112.2$ MeV. This fit shows an agreement of better than $1 \cdot 10^{-2}$ in the range 120 to 275 MeV. The latter results for W_0 and Γ_0 of this fit were used as start parameters in the following approach of fitting the p-wave contribution.

2nd step:

Next we varied the parameters W_0' and Γ_0' of the Δ^0-resonance to improve the fit of the SAID description to the SCX data. To this aim we introduced the ratio

$$r(W; W_0', \Gamma_0') = \sqrt{\frac{\sigma_{BW}(W, W_0', \Gamma_0')}{\sigma_{BW}(W, W_0, \Gamma_0)}} \tag{10.10}$$

which was used to modify the p_{33} contribution to the total SCX cross section. Starting with our last fit results of $W_0 = 1231.1$ MeV and $\Gamma_0 = 112.2$ MeV, the p_{33} amplitude in equation 2.13 was varied by the factor r to allow access to the SCX cross section obtained from the s- and p-wave amplitudes in dependence of W_0' and Γ_0':

$$\sigma_p(r) = [2|P_{13} - rP_{33}|^2 + |P_{11} - P_{31}|^2]C \tag{10.11}$$

The final expression to which a χ^2-fit was applied, is similar to equation 10.3:

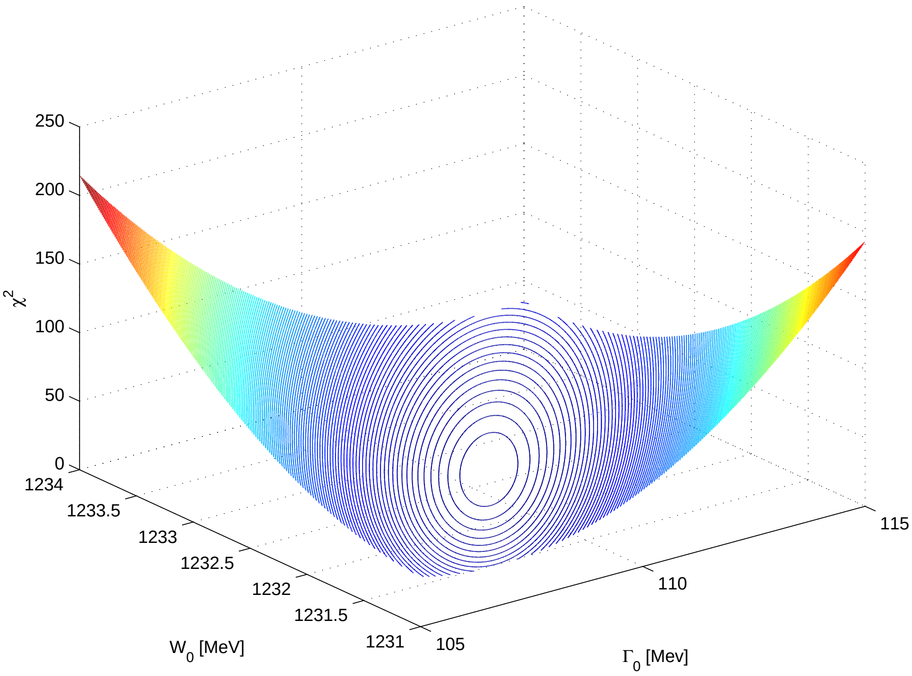

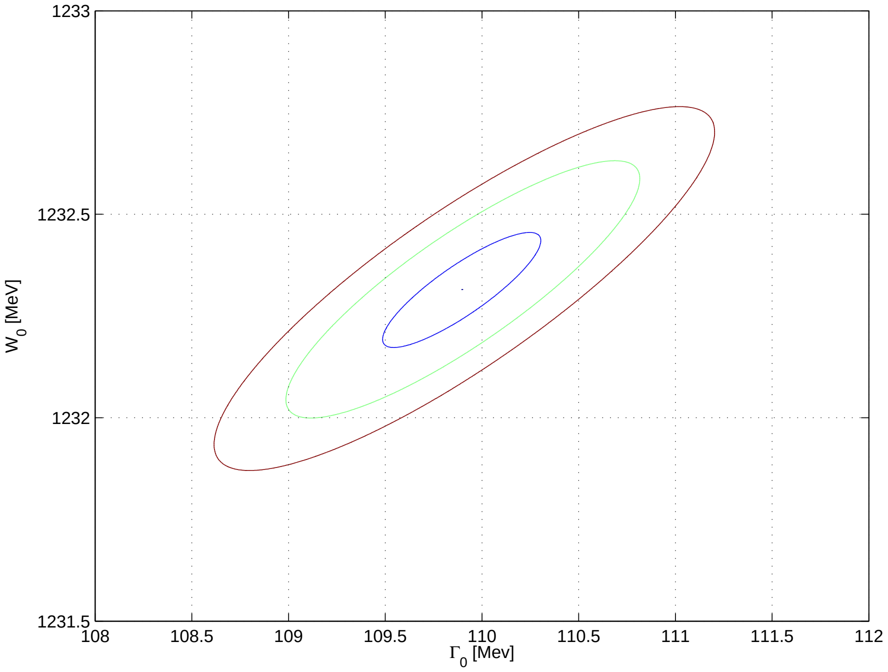

Figure 10.7: *Top: Fit result in a three dimensional plot showing the* χ^2 *in dependence of* W_0, Γ_0. *Bottom: The fit result projected in the* W_0 *and* Γ_0 *plane with 0.1, 0.5 and 1*σ *ellipses.*

$$\sigma_{SAID}(r) = \sigma_{SAID} + [\sigma_p(r) - \sigma_p(r = 1)] \tag{10.12}$$

What remains is a fit to the data minimizing $\chi^2(W_0', \Gamma_0')$ by varying r in equation 10.12. The results are shown in table 10.3 in the row "p-wave 38 – 250 MeV". With $W_0 = 1232.3$ MeV and $\Gamma_0 = 109.7$ MeV the model presented is as good as the s-wave fit. Figs. 10.7 shows the χ^2 for this fit in the W_0, Γ_0 plane. Other p-wave fits with a restricted energy range shown in table 10.3 were made to test the sensitivity of our data.

10.3.4 sp-wave model

As a final approach f, W_0 and Γ_0 were treated as free parameters. The resulting model is a combination of the s-wave model and the p-wave model (equation 10.1 and 10.11)

$$\sigma_{sp}(f, r) = \sigma_s(f) + \sigma_p(r) \tag{10.13}$$

and therefore

$$\sigma_{SAID}(r, f) = \sigma_{SAID} + [\sigma_{sp}(r, f) - \sigma_{sp}(r = 1, f = 1)] \tag{10.14}$$

The results of the sp-wave fit are shown in the "sp-wave" rows in table 10.3. The initial idea of the fit was to look for an isospin breaking in the s-wave at low energies. Yet, we find that the fit may be further improved by a modification of the p_{33}-wave. The smallest reduced χ^2 for our data is obtained from the fit with all three parameters used as free parameters. χ^2_{red} can not be understood to present the statistical variance because the total errors in the fit were used. Therefore the χ^2_{red} of about unity or better do not represent necessarily an excellent fit.

A sensitive representation of the data and the fit results are the ratio plots in figs. 10.8. The upper plot of fig. 10.8 shows the best fits for all data of this experiment adopting the total errors. The lower plot presents the same models but with the data of Salomon et al. and Bagheri et al. included. A careful inspection of figs. 10.8 shows the effect of the various parameter variations. The modification of the s-wave amplitudes affects the predicted SCX-cross section the most at the lowest energies, as was expected. A variation of the Δ^0-resonance has its strongest effects in the low energy slope, near 100 MeV. The tendency of the data to lie about 4 % below the original SAID prediction is reproduced by the sp-fit. But the experimental errors do not allow a clear distinction. Using only the data taken below 107 MeV in the s-wave fit, results in an even larger modification of -8.1 %. Overall the fits show that the best fit is obtained with a modification of both, the s- and the p_{33}-wave. This indicates that not only the s-wave should be taken into account in the context of the isospin breaking, but also the p-wave contribution should be considered. However this conclusion should be merely understood as a suggestion to look not only for isospin breaking in the s-wave amplitudes. On a closer look the fit results for the W_0 give similar results. The resonance width for the p-wave fit is smaller than the width extracted from the SAID amplitudes and far smaller than the values for the $\Delta^0(1232)$ published in the *Review of Particle Physics* [PDB] ($W_0 = 1233 - 1234$ MeV, $\Gamma_0 = 113 - 118$ MeV). The three p-wave fits for different energy ranges show the weak sensitivity of the resonance width Γ_0 to the low energy data points. In any case, the parameters of the Δ^0-resonance are much closer to those of the Δ^{++}-resonance ($W^{++} \approx 1232$ MeV, $\Gamma^{++} \approx 111$ MeV) that reported so far [PDB]. This suggests a very weak charge dependence of the Δ-resonances.

Table 10.3: *Fit results for various models using only results from this experiment*

Model	Energy range	Best fit parameters[a]			Energy range		All data	
		W_0 [MeV]	Γ_0 [MeV]	f-1 [%]	χ^2	χ^2_{red}	χ^2	χ^2_{red}
SAID	38 - 250 MeV	(1231.1)	(112.2)	0	31.7	1.76	31.7	1.76
s-wave	38 - 250 MeV	-	-	-4.4(1.4)	21.7	1.28	21.7	1.28
s-wave	38 - 107 MeV	-	-	-8.1(2.2)	7.4	0.82	28.5	1.68
p-wave	38 - 250 MeV	1232.3(0.2)	109.9(0.7)	0	20.3	1.27	20.3	1.27
p-wave	96 - 250 MeV	1231.7(0.2)	111.9(0.7)	0	7.8	0.98	20.7	1.29
p-wave	116 - 250 MeV	1231.7(0.2)	112.6(0.8)	0	5.8	0.97	22.9	1.43
sp-wave	38 - 250 MeV	1232.6(0.2)	111.9(0.7)	-3.5(1.4)	18.6	1.24	18.6	1.24
sp-wave[b]	38 - 250 MeV	1231.4(0.2)	111.0(0.6)	-1.5(1.1)	25.4	1.16	25.4	1.16

[a] errors based on total errors

[b] Including data of Bagheri et al. [Bag88a], and Salomon et al. [Sal84]

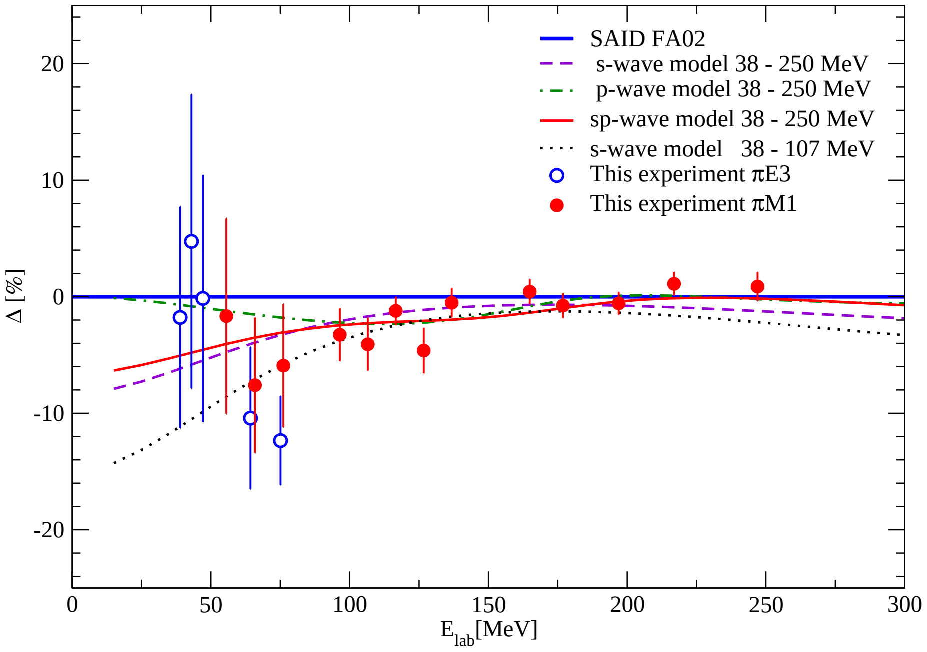

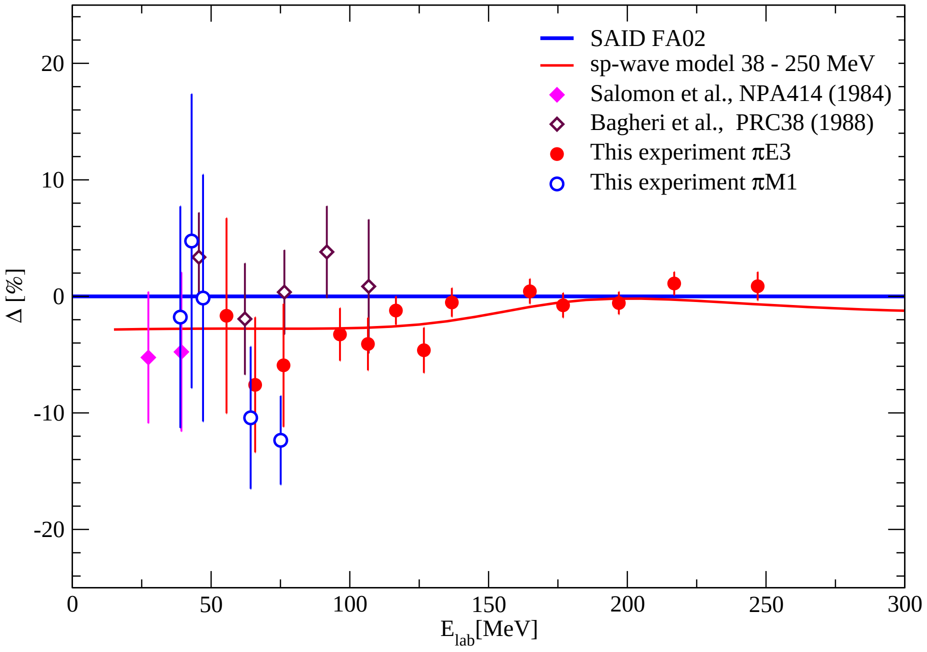

Figure 10.8: *Fractional deviation of measured and fitted SCX cross sections to those predicted from SAID FA02. Data points are from this experiment and from [Sal84], [Bag88b]. Inner error bars represent statistical errors only, outer error bars represent total errors. Top: Data from this experiment only. Bottom: With Bagheri and Salomon data included.*

Chapter 11

Summary and Conclusions

The motivation for the present work was in the lack of available πN-scattering data with high statistical accuracy. While nowadays for the elastic $\pi^{\pm}$p-scattering channels there is enough consistent data available, for the third easily accessible πN-channel, the SCX-reaction, reliable accurate experimental data was lacking. This lack could be the reason for the isospin symmetry breaking of about 7 % (in the s-wave amplitude) which has been seen previously. Therefore we developed a closed 4π-scintillator detector to measure the SCX-reaction using the transmission technique. The measurement covered an incident pion energy range of 38 to 250 MeV which is the largest energy range (at low energies) measured in one single experimental setup so far. This experiment expanded the available world data base by 50 %. The targets used, were a solid CH_2-target and for background subtraction a C-target. The solid targets allowed for convenient target handling and an uncomplex experimental setup. For each target the cross section for production of neutrals was measured and the difference between these gives the SCX cross section. With the use of precise Monte-Carlo simulations false detection of the neutrals (photons or neutrons) was determined and the resulting SCX cross section was corrected.

The statistical error of the measurement is typically about 1 %. The total error adds up to about 2 % over the Δ-resonance with increasing tendency for energies below 90 MeV. The larger systematic errors towards lower energies are caused by unforeseen target absorption effects that are complex and are not understandable by Monte-Carlo simulations. Runs with positively charged pions, from which a zero cross section for the production of neutrals was expected, were used to estimate the absorption effects and their systematic errors of up to 8.6 % at the lowest energies.

The results of the present experiment show good agreement with the previous accurate measurements of Bugg et al. [Bug71] which covered the Δ-resonance region. Yet, these data are about 3 % higher than the results of a similar experiment performed at TRIUMF [Fri93]. A closer look at the experimental details of that experiment indicates that in the Monte-Carlo simulations the detection of the neutrals was underestimated and a correction of the TRIUMF data of the same order as our corrections would equalize the TRIUMF data with our SCX results.

For the lowest energies we also have a good agreement with previous measurements. Only in the energy range from 60 to 80 MeV we have a significant deviation of about −8 % from the values of Bagheri et al. [Bag88a].

Our conclusions are based on the predictions of the SAID phase-shift analyses [SAID] which are the output of partial wave fits to the existing world data base of πp-scattering. SAID gives a good description of the elastic πp-scattering cross sections. An important aspect is that as an assumption in the SAID predictions the isospin symmetry is not broken. Therefore a deviation of our data from the SAID output, as happens in the energy range from 60 to 80 MeV, indicates a possible isospin breaking in the hadronic system.

A modification of the s-wave amplitudes and/or the p_{33} amplitude was done to obtain a better fit to the data and to be able to estimate the size of the isospin breaking. The best fit for the modification of the s-wave content was achieved for a $(4 \pm 1.5)\%$ reduction of the s-wave. A slightly better fit was obtained by an additional simultaneous modification of the position and width of the Breit-Wigner resonance which could indicate a charge dependence of the Δ-resonances. Furthermore it could be shown that the p_{33} part of the SAID cross section is very well described by a Breit-Wigner shape.

As an incidental remark, we suggest that the charge dependence of the Δ-resonances is much weaker than reported [PDB]. The specified position and width of the Breit-Wigner resonance for the Δ^0 are $W^0 \approx 1233.5$ MeV, $\Gamma^0 \approx 116$ MeV and differ from those of the Δ^{++} with $W^{++} \approx 1231$ and $\Gamma^{++} \approx 111$ MeV. Whereas the parameters for the Δ^0 we extract from our fits, with $W^0 \approx 1232$ and $\Gamma^0 = 110 - 112$ MeV, are closer to the Δ^{++} parameters.

As a final conclusion we propose that the SCX cross sections measured in the present work indicate a possible isospin breaking. However, the estimated violation of the isospin symmetry in the s-waves is half of the reported 7 % violation which was one of the original motivations for this experiment. Beyond, the results of this work suggest that the aspect of isospin breaking should not only include the s-waves alone but also the waves of higher order. Any further conclusions demand a phase-shift analysis including all available πN data, elastic and SCX, with a formalism which, other than assumed by SAID, does not imply conservation of isospin symmetry. Such an analysis is clearly beyond the scope of this experimental thesis.

Appendix A

Tables of total SCX cross sections

Table A.1: *Raw results for the $\pi E3$ channel*

Run ID target, rates	Triggers $C/CH_2/-$	Zeros effi.	Ors effi.	Zeros effi. rnd.	Ors effi. rnd.	1000(1-T)	σ_{raw} [mb] $C/CH_2/H$
1a[1]	27814798	575793	415308	577841	415134	5.850	103.64(39)
$-38.92MeV$	24645319	457527	333980	459073	333870	5.080	117.68(53)
thick, $4.6kHz$	27805137	288080	247206	288630	247182	1.491	7.02(29)
1b[1]	70884501	1466481	1057437	1471572	1057024	5.848	103.65(24)
$-38.92MeV$	103659794	1927156	1406734	1933628	1406310	5.087	117.96(26)
thick, $4.6kHz$	94649524	982586	843507	984377	843453	1.489	7.15(16)
2	26926385	425252	376291	425732	376220	1.839	27.02(23)
$+38.92MeV$	30239441	437729	388812	438215	388728	1.637	30.65(29)
thick, $6.2kHz$	30522553	265423	244297	265638	244286	0.700	1.81(16)
3a[1]	13897313	229968	178454	230547	178413	3.751	87.07(72)
$-39.48MeV$	13897012	210200	165041	210735	164992	3.292	95.94(95)
mid, $4.6kHz$	19455905	202049	173146	202391	173130	1.504	4.44(53)
3b[1]	52070566	857632	665045	858595	664824	3.721	86.13(41)
$-39.48MeV$	80742526	1222832	959485	1224148	959191	3.282	95.72(49)
mid, $4.6kHz$	34800333	361790	309944	362049	309920	1.498	4.80(24)
4	12565835	161430	148190	161565	148149	1.068	13.73(46)
$+39.48MeV$	21541132	256675	236515	256881	236502	0.946	12.51(54)
mid, $6.2kHz$	12568920	109163	100301	109252	100295	0.713	-0.61(26)
5	44333859	653514	521125	654179	521023	3.003	81.10(57)
$-39.72MeV$	79276518	1093160	877940	1094222	877768	2.730	92.44(66)
thin, $4.6kHz$	34800333	361790	309944	362049	309920	1.498	5.67(32)
6	206804241	3993887	2869356	3999495	2868390	5.469	96.64(14)
$-42.99MeV$	205256899	3490804	2536199	3495483	2535318	4.678	107.30(18)
thick, $5.3kHz$	203777867	1803849	1519278	1805269	1519133	1.404	5.33(10)
7a[1]	68071845	1231624	853127	1233570	852709	5.595	102.99(24)
$-47.10MeV$	71334307	1114448	777908	1116172	777564	4.747	114.19(30)
thick, $5.0kHz$	69125462	484759	397980	485212	397936	1.263	5.60(17)
7b[1]	18321824	136992	234679	339202	234565	5.711	102.52(50)
$-47.10MeV$	27047170	338691	302326	432821	302199	4.829	112.44(58)
thick, $5.0kHz$	10361808	432185	62529	77020	62523	1.399	4.96(31)
8	27823361	396609	289386	397143	289264	3.877	95.95(54)
$-47.61MeV$	41430641	526211	386590	526905	386435	3.390	106.79(63)
mid, $5.0kHz$	25969212	192938	156762	193117	156743	1.401	5.42(34)
9	27676685	339354	255153	339774	255087	3.060	89.38(69)
$-47.82MeV$	42929729	482551	363711	483134	363617	2.784	103.75(82)
thin, $5.0kHz$	25969212	192938	156762	193117	156743	1.401	7.19(42)
11a[1]	46992979	902446	582432	903443	582139	6.837	125.05(32)
$-64.27MeV$	59682652	957312	610615	958407	610320	5.832	139.43(37)
thick, $4.9kHz$	50021334	253140	174363	253393	174304	1.581	7.19(22)
11b[1]	109485166	2107670	1359246	2110002	1358563	6.863	125.65(21)
$-64.27MeV$	105276746	1687055	1075911	1688986	1075395	5.828	139.28(27)
thick, $4.9kHz$	116126767	587372	404419	587961	404283	1.582	6.81(16)

---

[1] different calibration

12	23575171	297354	262943	297454	262500	1.483	22.92 (22)
$+64.27MeV$	22353347	237806	211580	237882	211282	1.190	22.03 (29)
thick, $5.1kHz$	20349785	60453	50028	60484	49980	0.516	-0.44(15)
15	151079148	3182961	2073176	3191206	2071330	7.413	135.65(18)
$-75.09MeV$	151542731	2635161	1678326	2642232	1676877	6.370	152.80(24)
thick, $10.5kHz$	153971437	750340	488754	752291	488585	1.712	8.58(14)
16	46679435	662460	587429	663043	586997	1.629	27.08(16)
$+75.09MeV$	43076355	513037	458519	513461	458202	1.283	26.02(20)
thick, $10.5kHz$	56179160	146130	119005	146336	118961	0.487	-0.53(11)

Table A.2: *Raw results for the $\pi M1$ channel*

Run ID	Triggers	Zeros	Ors	Zeros	Ors	1000(1-T)	σ_{raw} [mb]
target, rates	$C/CH2/-$	effi.	effi.	effi. rnd.	effi. rnd.		$C/CH2/H$
10a[1]	49898866	869881	566936	882777	562627	6.416	115.88(30)
$-55.55MeV$	49794625	729112	471387	740111	468006	5.465	128.56(39)
thick, $3.0kHz$	45630232	228802	162139	231731	161279	1.544	6.34(22)
10b[1]	110418585	1924370	1253408	1952707	1244092	6.418	115.67(20)
$-55.55MeV$	114151373	1669388	1077641	1694345	1069610	5.473	128.48(26)
thick, $3.0kHz$	111902011	563822	398970	570850	396893	1.555	6.41(15)
13a[2]	96553689	1795724	1167112	1829896	1148154	7.061	130.60(22)
$-65.88MeV$	98264380	1513218	967287	1542576	951960	6.010	145.59(29)
thick, $3.9kHz$	107232863	469149	312800	477614	309075	1.571	7.50(17)
13b[3]	15432901	290539	188614	295022	185660	7.086	130.57(57)
$-65.88MeV$	15473840	239308	152663	243232	150274	6.007	144.62(73)
thick, $3.4kHz$	15455205	68008	44969	69036	44332	1.598	7.02(42)
13c[4]	4540937	86515	55926	87386	55438	7.036	129.46(96)
$-65.88MeV$	4540128	70919	45101	71732	44680	5.958	143.13(1.22)
thick, $2.9kHz$	26539292	118739	78283	119999	77680	1.595	6.84(76)
14 [4]	32214881	434441	288994	438963	286376	4.737	121.79(56)
$-66.31MeV$	27074773	308893	201639	312264	199805	4.154	137.41(79)
mid, $2.9kHz$	26539292	118739	78283	119999	77680	1.595	7.81(41)
17a[2]	46531738	924999	614522	943422	607338	7.223	137.95(32)
$-76.10MeV$	50041231	815734	530476	832358	523977	6.163	155.40(40)
thick, $4.2kHz$	61285273	239889	158755	244626	157319	1.425	8.73(24)
17b[2]	74443130	1485691	987440	1516894	972736	7.310	138.77(26)
$-76.10MeV$	82394762	1350401	875116	1380854	860705	6.313	158.61(33)
thick, $4.2kHz$	68546794	268187	175134	274151	172862	1.478	9.92(19)
17c[2]	13138833	273867	178308	275972	177222	7.516	142.71(60)
$-76.10MeV$	25455845	434677	277094	438149	275289	6.398	160.05(58)
thick, $4.9kHz$	24941115	102075	65270	102871	64984	1.519	8.67(39)
17d[4]	7163903	151144	98831	151731	98506	7.430	141.34(84)
$-76.10MeV$	5710047	99223	63356	99616	63195	6.378	160.36(1.19)
thick, $1.7kHz$	7258903	30414	19750	30531	19714	1.490	9.51(67)
18	52510429	1224399	825137	1233956	822354	7.838	146.98(32)
$-96.46MeV$	48008111	933602	604662	941108	602580	7.051	176.82(44)
thick, $6.2kHz$	48137569	214165	136242	216012	135924	1.664	14.92(25)
19	42896090	1064120	719387	1072880	716303	8.313	153.27(37)
$-106.54MeV$	50802991	1061891	685309	1071345	682286	7.658	189.85(46)
thick, $6.9kHz$	43647570	209046	129592	211006	129136	1.876	18.29(26)
20	89592591	2305100	1568003	2314214	1565459	8.357	154.72(25)
$-116.62MeV$	95672075	2098993	1347492	2108081	1345073	7.975	200.81(33)
thick, $5.1kHz$	93205687	443464	272576	445500	272156	1.860	23.05(19)
21a[4]	19867784	520291	353693	521483	353441	8.458	154.19(54)
$-126.70MeV$	21580900	490006	311599	491285	311358	8.337	208.69(72)
thick, $5.0kHz$	21712413	107759	65042	108052	64986	1.983	27.25(41)

[1] different calibration

[2] high rate

[3] medium rate

[4] low rate

21b[2]	24178357	605589	413620	611865	411694	8.279	151.52(49)
$-126.70MeV$	22828722	496258	317893	502036	316330	8.135	204.24(69)
thick, 7.9kHz	24232044	114052	69365	115470	69048	1.916	26.36(38)
22	23884477	479578	449554	480727	448612	1.345	27.81(19)
$+126.70MeV$	23946064	467374	444464	468257	443684	1.026	27.94(23)
thick, 8.3kHz	23854352	66845	63011	66991	62895	0.172	0.07(14)
23	58315696	1542088	1041926	1545793	1040863	8.659	151.09(32)
$-136.77MeV$	61486542	1440828	897602	1444896	896642	8.917	216.91(44)
thick, 10.5kHz	70096639	367678	206728	368883	206570	2.316	32.91(25)
24	18432968	455413	312933	456270	312659	7.791	136.41(54)
$-164.89MeV$	21810543	499316	307746	500457	307485	8.848	222.97(74)
thick 8.0kHz	21822644	103843	59156	104106	59125	2.061	43.28(42)
25	23963970	406846	279333	407592	279176	5.359	127.88(71)
$-165.22MeV$	18166534	286549	177557	287185	177441	6.041	213.95(1.14)
mid, 8.0kHz	18160897	86200	49010	86415	48980	2.061	43.03(58)
26	45896964	1093966	755581	1096079	755264	7.426	129.19(34)
$-176.86MeV$	42054114	935485	578560	937715	578326	8.546	215.09(52)
thick, 9.2kHz	42053612	192312	108847	192832	108806	1.998	42.95(28)
27	44643055	988760	690583	990716	690353	6.728	116.15(33)
$-196.96MeV$	44959675	924660	578835	926871	578648	7.745	193.68(48)
thick, 9.5kHz	44746318	189513	107469	190041	107423	1.846	38.77(26)
28	24785015	500467	353773	501388	353633	5.961	104.39(39)
$-216.99MeV$	42725328	788988	503094	790785	502889	6.738	169.53(44)
thick, 10.1kHz	67029566	244107	139464	244765	139416	1.572	32.57(28)
29	39644216	546572	384809	547588	384670	4.110	98.34(44)
$-217.29MeV$	43767516	555894	355339	557162	355206	4.614	163.41(61)
mid, 10.1kHz	67029566	244107	139464	244765	139416	1.572	32.54(34)
30	48650119	865983	627167	868213	626877	4.961	86.87(26)
$-247.00MeV$	48645015	773269	513254	775678	512985	5.400	134.26(38)
thick, 12.2kHz	59738147	193060	115858	193769	115808	1.305	23.69(21)

[2] high rate

Table A.3: *Averaging of cross sections for the $\pi E3$ channel*

Run ID	T_{exp} [MeV]	$\sigma_{tgt}(\delta\sigma_{stat})$ [mb]	T_{thick} [mb]	$\sigma_{av}(\delta\sigma_{stat})$ [mb]
3a	-39.48	4.88(53)	-	
3b	-39.48	5.24(24)	-	
5	-39.72	6.95(32)	-38.92	5.42(19)
6	-42.99	6.05(10)	-42.99	6.05(10)
7a	-47.10	6.24(17)	-	
7b	-47.10	5.60(31)	-	
8	-47.61	5.78(34)	-	
9	-47.82	7.41(42)	-47.10	6.17(13)
11a	-64.27	7.66(22)	-	
11b	-64.27	7.28(16)	-64.27	7.41(13)
15	-75.09	8.92(14)	-75.09	8.92(14)

Table A.4: *Averaging of cross sections for the πM1 channel*

Run ID	T_{exp} [MeV]	$\sigma_{tgt}(\delta\sigma_{stat})$ [mb]	T_{thick} [mb]	$\sigma_{av}(\delta\sigma_{stat})$ [mb]
10a	-55.55	6.92(22)	-	
10b	-55.55	6.99(15)	-	
10c	-55.55	5.52(1.71)	-55.55	6.96(12)
13a	-65.88	7.96(17)	-	
13b	-65.88	7.48(42)	-	
13c	-65.88	7.30(76)	-	
14	-66.31	8.02(41)	-65.88	7.89(15)
17a	-76.10	9.07(24)	-	
17b	-76.10	10.26(20)	-	
17c	-76.10	9.01(39)	-	
17d	-76.10	9.85(67)	-76.10	9.71(14)
18	-96.46	15.02(25)	-96.46	15.02(25)
19	-106.54	18.29(26)	-106.54	18.29(26)
20	-116.62	23.05(19)	-116.62	23.05(19)
21a	-126.70	27.25(41)	-	
21b	-126.70	26.36(38)	-126.70	26.77(28)
23	-136.77	32.91(25)	-136.77	32.91(25)
24	-164.89	43.28(42)	-	
25	-165.22	43.03(58)	-164.89	43.17(34)
26	-176.86	42.95(28)	-176.86	42.95(28)
27	-196.96	38.77(26)	-196.96	38.77(26)
28	-216.99	32.57(28)	-	
29	-217.29	32.54(34)	-216.99	32.60(22)
30	-247.00	23.69(21)	-247.00	23.69(21)

Appendix B

SAID SCX scattering amplitudes and total SCX cross sections

Table B.1: *s-wave amplitudes for* $T_\pi = 15 - 345 MeV$

T_{exp}	$S_{11\ Re}$	$S_{11\ Im}$	$S_{31\ Re}$	$S_{31\ Im}$
15.00	0.0685	0.0047	−0.0385	0.0015
25.00	0.0864	0.0075	−0.0540	0.0029
35.00	0.1000	0.0101	−0.0685	0.0047
45.00	0.1111	0.0125	−0.0826	0.0069
55.00	0.1204	0.0147	−0.0962	0.0093
65.00	0.1284	0.0168	−0.1096	0.0122
75.00	0.1354	0.0187	−0.1226	0.0153
85.00	0.1416	0.0205	−0.1353	0.0186
95.00	0.1471	0.0221	−0.1476	0.0223
105.00	0.1520	0.0237	−0.1596	0.0262
115.00	0.1563	0.0251	−0.1713	0.0303
125.00	0.1603	0.0264	−0.1826	0.0345
135.00	0.1638	0.0276	−0.1936	0.0390
145.00	0.1670	0.0287	−0.2043	0.0436
155.00	0.1699	0.0298	−0.2146	0.0484
165.00	0.1726	0.0307	−0.2247	0.0533
175.00	0.1751	0.0317	−0.2344	0.0583
185.00	0.1774	0.0326	−0.2437	0.0635
195.00	0.1796	0.0335	−0.2528	0.0687
205.00	0.1817	0.0343	−0.2616	0.0740
215.00	0.1837	0.0353	−0.2701	0.0794
225.00	0.1857	0.0362	−0.2784	0.0848
235.00	0.1877	0.0371	−0.2864	0.0903
245.00	0.1897	0.0382	−0.2941	0.0958
255.00	0.1918	0.0392	−0.3016	0.1013
265.00	0.1940	0.0404	−0.3088	0.1069
275.00	0.1962	0.0416	−0.3157	0.1125
285.00	0.1986	0.0429	−0.3225	0.1180
295.00	0.2011	0.0444	−0.3289	0.1236
305.00	0.2038	0.0459	−0.3352	0.1291
315.00	0.2067	0.0476	−0.3412	0.1346
325.00	0.2097	0.0495	−0.3469	0.1400
335.00	0.2130	0.0515	−0.3524	0.1454
345.00	0.2166	0.0538	−0.3577	0.1508

Table B.2: *p-wave amplitudes for* $T_\pi = 15 - 345 MeV$

T_{exp}	$P_{11\ Re}$	$P_{11\ Im}$	$P_{13\ Re}$	$P_{13\ Im}$	$P_{31\ Re}$	$P_{31\ Im}$	$P_{33\ Re}$	$P_{33\ Im}$
15.00	−0.0035	0.0000	−0.0016	0.0000	−0.0025	0.0000	0.0144	0.0002
25.00	−0.0067	0.0000	−0.0034	0.0000	−0.0053	0.0000	0.0321	0.0010
35.00	−0.0098	0.0001	−0.0054	0.0000	−0.0086	0.0001	0.0554	0.0031
45.00	−0.0127	0.0002	−0.0077	0.0001	−0.0122	0.0001	0.0842	0.0071
55.00	−0.0151	0.0002	−0.0100	0.0001	−0.0161	0.0003	0.1188	0.0143
65.00	−0.0169	0.0003	−0.0124	0.0002	−0.0202	0.0004	0.1595	0.0261
75.00	−0.0180	0.0003	−0.0149	0.0002	−0.0246	0.0006	0.2064	0.0446
85.00	−0.0184	0.0003	−0.0174	0.0003	−0.0292	0.0009	0.2592	0.0724
95.00	−0.0179	0.0003	−0.0199	0.0004	−0.0339	0.0012	0.3168	0.1131
105.00	−0.0165	0.0003	−0.0224	0.0005	−0.0388	0.0015	0.3764	0.1709
115.00	−0.0142	0.0002	−0.0249	0.0006	−0.0438	0.0019	0.4330	0.2500
125.00	−0.0108	0.0001	−0.0274	0.0008	−0.0489	0.0024	0.4780	0.3535
135.00	−0.0065	0.0000	−0.0298	0.0009	−0.0541	0.0029	0.4996	0.4802
145.00	−0.0010	0.0000	−0.0322	0.0010	−0.0595	0.0035	0.4849	0.6221
155.00	0.0057	0.0000	−0.0346	0.0012	−0.0648	0.0042	0.4253	0.7630
165.00	0.0135	0.0002	−0.0369	0.0014	−0.0703	0.0050	0.3228	0.8819
175.00	0.0227	0.0006	−0.0392	0.0015	−0.0758	0.0058	0.1913	0.9619
185.00	0.0331	0.0014	−0.0414	0.0017	−0.0813	0.0068	0.0511	0.9971
195.00	0.0450	0.0026	−0.0436	0.0019	−0.0868	0.0079	-0.0801	0.9931
205.00	0.0583	0.0045	−0.0457	0.0021	−0.0923	0.0090	-0.1918	0.9610
215.00	0.0731	0.0071	−0.0478	0.0023	−0.0978	0.0103	-0.2811	0.9125
225.00	0.0894	0.0107	−0.0498	0.0025	−0.1033	0.0117	-0.3493	0.8565
235.00	0.1073	0.0155	−0.0517	0.0027	−0.1088	0.0132	-0.3996	0.7988
245.00	0.1267	0.0218	−0.0536	0.0030	−0.1142	0.0147	-0.4359	0.7428
255.00	0.1475	0.0299	−0.0554	0.0032	−0.1196	0.0164	-0.4613	0.6901
265.00	0.1696	0.0402	−0.0572	0.0034	−0.1249	0.0182	-0.4784	0.6415
275.00	0.1927	0.0531	−0.0589	0.0036	−0.1301	0.0202	-0.4894	0.5969
285.00	0.2166	0.0691	−0.0605	0.0039	−0.1353	0.0222	-0.4958	0.5563
295.00	0.2408	0.0884	−0.0620	0.0041	−0.1404	0.0244	-0.4987	0.5192
305.00	0.2645	0.1114	−0.0635	0.0043	−0.1454	0.0266	-0.4989	0.4854
315.00	0.2872	0.1384	−0.0649	0.0045	−0.1503	0.0291	-0.4971	0.4544
325.00	0.3077	0.1694	−0.0663	0.0047	−0.1551	0.0316	-0.4938	0.4259
335.00	0.3251	0.2041	−0.0676	0.0050	−0.1599	0.0343	-0.4892	0.3997
345.00	0.3383	0.2419	−0.0688	0.0052	−0.1646	0.0372	-0.4837	0.3754

Table B.3: *s-wave amplitudes at the energies used in the experiments*

T_{exp}	$S_{11\ Re}$	$S_{11\ Im}$	$S_{31\ Re}$	$S_{31\ Im}$
27.40	0.0900	0.0082	−0.0575	0.0033
39.30	0.1051	0.0112	−0.0746	0.0056
45.60	0.1117	0.0126	−0.0834	0.0070
62.20	0.1263	0.0162	−0.1059	0.0113
76.40	0.1363	0.0189	−0.1244	0.0157
91.70	0.1453	0.0216	−0.1436	0.0211
106.80	0.1528	0.0239	−0.1618	0.0269
38.92	0.1046	0.0111	−0.0741	0.0055
42.99	0.1090	0.0120	−0.0798	0.0064
47.10	0.1132	0.0130	−0.0855	0.0074
64.27	0.1279	0.0166	−0.1086	0.0119
75.09	0.1355	0.0187	−0.1227	0.0153
55.50	0.1209	0.0148	−0.0970	0.0095
65.90	0.1291	0.0169	−0.1107	0.0124
76.10	0.1361	0.0189	−0.1240	0.0156
96.50	0.1478	0.0224	−0.1494	0.0228
106.50	0.1527	0.0239	−0.1614	0.0268
116.60	0.1570	0.0253	−0.1732	0.0309
126.70	0.1609	0.0266	−0.1845	0.0353
136.80	0.1644	0.0278	−0.1955	0.0398
164.90	0.1726	0.0307	−0.2245	0.0533
176.90	0.1755	0.0318	−0.2361	0.0593
197.00	0.1800	0.0336	−0.2546	0.0698
216.90	0.1841	0.0354	−0.2717	0.0804
247.00	0.1902	0.0384	−0.2956	0.0969

Table B.4: *p-wave amplitudes at the energies used in the experiments*

T_{exp}	$P_{11\ Re}$	$P_{11\ Im}$	$P_{13\ Re}$	$P_{13\ Im}$	$P_{31\ Re}$	$P_{31\ Im}$	$P_{33\ Re}$	$P_{33\ Im}$
27.40	−0.0074	0.0001	−0.0039	0.0000	−0.0061	0.0000	0.0372	0.0014
39.30	−0.0111	0.0001	−0.0064	0.0000	−0.0101	0.0001	0.0671	0.0045
45.60	−0.0129	0.0002	−0.0078	0.0001	−0.0124	0.0002	0.0861	0.0075
62.20	−0.0165	0.0003	−0.0117	0.0001	−0.0191	0.0004	0.1475	0.0222
76.40	−0.0181	0.0003	−0.0152	0.0002	−0.0252	0.0006	0.2134	0.0478
91.70	−0.0181	0.0003	−0.0191	0.0004	−0.0323	0.0010	0.2974	0.0980
106.80	−0.0161	0.0003	−0.0229	0.0005	−0.0397	0.0016	0.3870	0.1835
38.92	−0.0110	0.0001	−0.0063	0.0000	−0.0099	0.0001	0.0660	0.0044
42.99	−0.0122	0.0001	−0.0072	0.0001	−0.0114	0.0001	0.0779	0.0061
47.10	−0.0133	0.0002	−0.0081	0.0001	−0.0130	0.0002	0.0909	0.0083
64.27	−0.0168	0.0003	−0.0122	0.0001	−0.0199	0.0004	0.1563	0.0251
75.09	−0.0180	0.0003	−0.0149	0.0002	−0.0247	0.0006	0.2068	0.0448
55.50	−0.0152	0.0002	−0.0101	0.0001	−0.0163	0.0003	0.1209	0.0148
65.90	−0.0171	0.0003	−0.0126	0.0002	−0.0206	0.0004	0.1634	0.0274
76.10	−0.0181	0.0003	−0.0152	0.0002	−0.0251	0.0006	0.2119	0.0471
96.50	−0.0177	0.0003	−0.0203	0.0004	−0.0346	0.0012	0.3254	0.1204
106.50	−0.0162	0.0003	−0.0228	0.0005	−0.0395	0.0016	0.3855	0.1816
116.60	−0.0137	0.0002	−0.0253	0.0006	−0.0446	0.0020	0.4414	0.2651
126.70	−0.0102	0.0001	−0.0278	0.0008	−0.0498	0.0025	0.4837	0.3735
136.80	−0.0056	0.0000	−0.0303	0.0009	−0.0551	0.0030	0.5000	0.5044
164.90	0.0134	0.0002	−0.0369	0.0014	−0.0702	0.0050	0.3241	0.8807
176.90	0.0245	0.0007	−0.0396	0.0016	−0.0768	0.0060	0.1653	0.9718
197.00	0.0475	0.0029	−0.0440	0.0020	−0.0879	0.0081	-0.1036	0.9886
216.90	0.0761	0.0077	−0.0482	0.0024	−0.0989	0.0106	-0.2956	0.9022
247.00	0.1307	0.0232	−0.0540	0.0030	−0.1153	0.0151	-0.4417	0.7320

Table B.5: *SAID predictions of the total SCX cross section* σ_{SCX} *for* $T_\pi = 15 - 345 MeV$

T_{exp} [MeV]	σ_{SCX} [mb]	T_{exp} [MeV]	σ_{SCX} [mb]	T_{exp} [MeV]	σ_{SCX} [mb]
15.00	4.592	135.00	35.59	255.00	24.28
25.00	4.854	145.00	40.94	265.00	22.10
35.00	5.396	155.00	45.32	275.00	20.25
45.00	6.211	165.00	47.95	285.00	18.70
55.00	7.332	175.00	48.49	295.00	17.41
65.00	8.820	185.00	47.08	305.00	16.33
75.00	10.75	195.00	44.25	315.00	15.43
85.00	13.21	205.00	40.66	325.00	14.69
95.00	16.33	215.00	36.85	335.00	14.06
105.00	20.15	225.00	33.17	345.00	13.53
115.00	24.74	235.00	29.81		
125.00	30.00	245.00	26.84		

Table B.6: *SAID predictions of the total SCX cross section* σ_{SCX} *of the energies in the experimental measurement*

T_{exp} [MeV]	σ_{SCX} [mb]	T_{exp} [MeV]	σ_{SCX} [mb]	T_{exp} [MeV]	σ_{SCX} [mb]
27.40	4.96	38.90	5.68	106.50	20.81
39.30	5.71	43.00	6.02	116.60	25.56
45.60	6.27	47.10	6.42	126.70	30.94
62.20	8.36	64.30	8.70	136.80	36.57
76.40	11.06	75.10	10.77	164.90	47.93
91.70	15.22	55.60	7.40	176.90	48.36
106.80	20.92	65.90	8.97	197.00	43.59
		76.10	10.99	216.90	36.13

Appendix C

Beam line calibration of the beamline πM1

C.1 Calibration of the TOF spectra

To calibrate the TOF spectra, we used the 19.75 ns structure of the cyclotron. Fig. C.1 shows the 19.75 ns structure as seen in the B0 counter in the πM1-channel at 250 MeV. A fit of a Gaussian in each peak and the averaging of the obtained peak maxima gives a calibration value of 1.1110(26) ns/ch.

C.2 Energy calibration of the beamline πM1

As described in section 4.2.1 for the calculation of the time of flight for protons in the beam line calibration

$$T_{protons} = |T1_{long} - T0_{long}| - |T1_{short} - T0_{short}| \tag{C.1}$$

is used. Fig. C.2 shows the corresponding TOF peaks of the B0 counter and fig. C.3 shows the TOF spectra of the B1 counter.

Also to these TOF peaks a Gaussian fit was applied. With the relation C.1 and the TOF calibration the final time of flight is obtained. The counter B1 was used as the start counter for

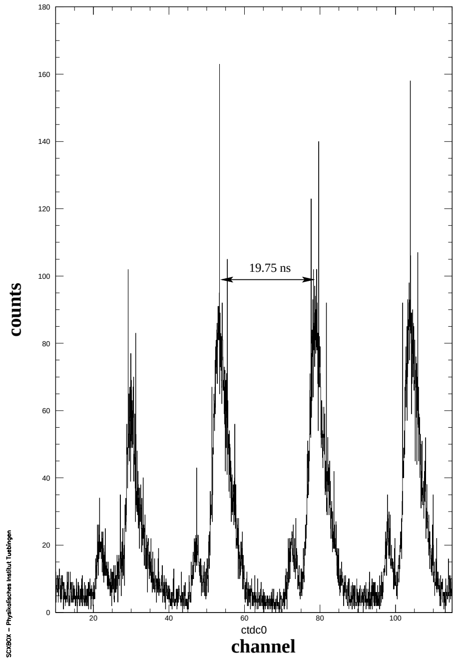

Figure C.1: *πM1 19.75 ns structure*

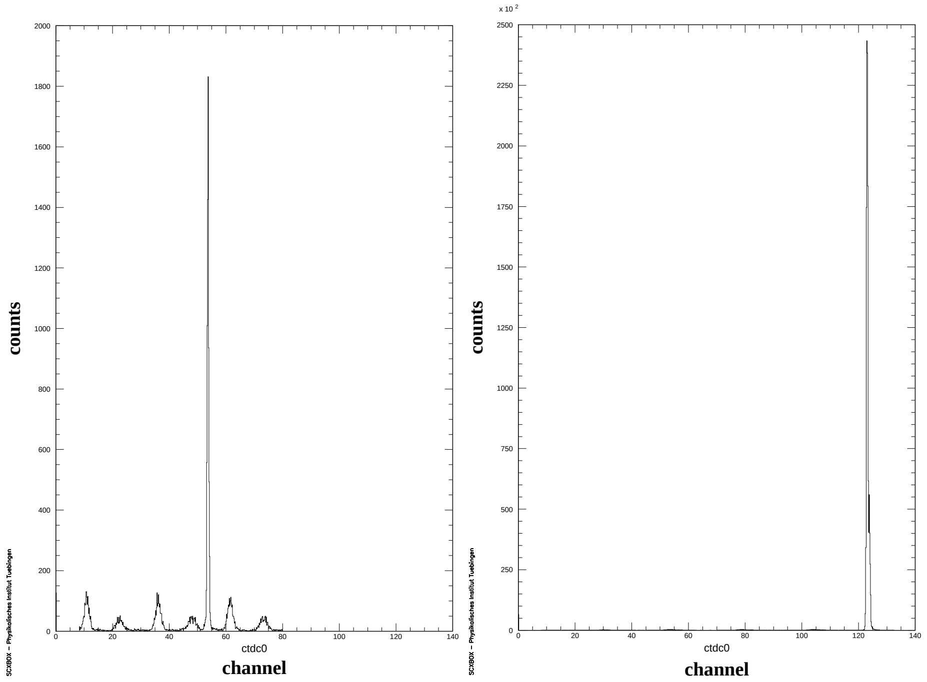

Figure C.2: *Time of flight difference for 250 MeV protons for the B0 counter: left spectra B0 setup 1, right spectra B0 setup 2. In the left spectrum the 20 ns structure can be seen*

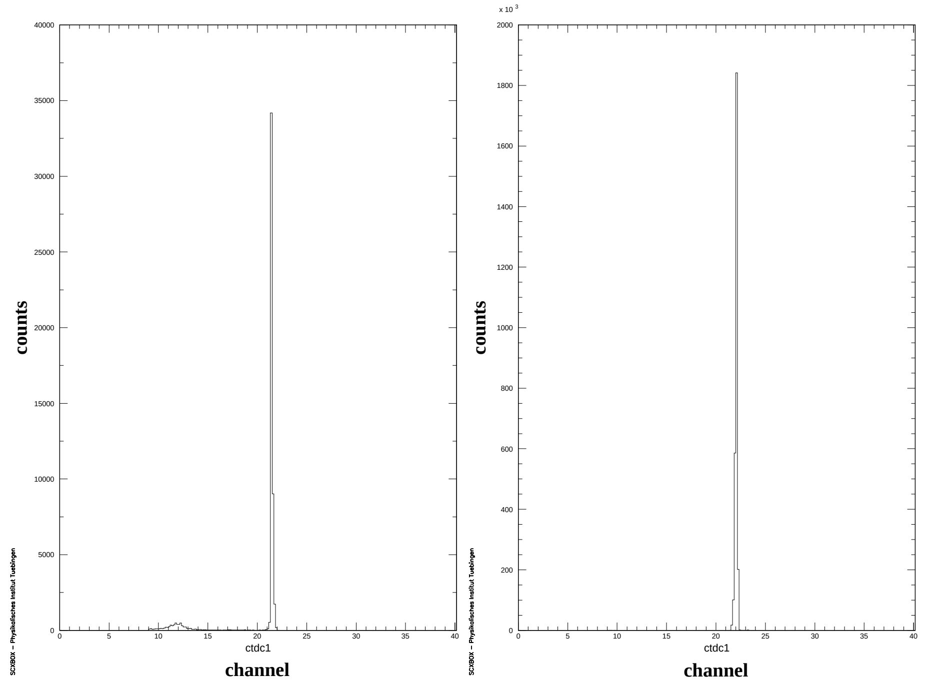

Figure C.3: *Time of flight difference for 250 MeV protons for the B1 counter: left spectra B1 setup 1, right spectra B1 setup 2*

the data acquisition. Therefore the peaks in the B1 spectrum are very narrow. The advantage of using the method with the two counters B0 and B1 is that relative time of flight is measured and the cable lengths and the time of the signal processing in the electronics is not needed for the calculation of the TOF. With a flight distance of 5.687 m in 54.91(13) ns results a speed for the protons of

$$v = \frac{5.687 \text{ m}}{54.91 \text{ ns}} = 0.103569 \ \frac{m}{ns}$$

With the mass of the proton of

$$M_{proton} = 938.27231(28)$$

MeV and the speed of light

$$c = 299792458\ \frac{m}{s}$$

and

$$P_{proton} = \frac{\beta \cdot M_{proton}}{\sqrt{1-\beta^2}} = 352.70\ \frac{\mathrm{MeV}}{c}$$

one obtains a kinetic energy of $E_{proton} = 64.10$ MeV.

This is the proton energy at the position of the B1 counter. The resulting energy of the protons entering the beam line can be calculated by adding the energy loss in the beam line windows, air and in the B0 counter to the obtained energy. Right before the momentum selecting magnet ASM11 the protons had a momentum of 364.83 MeV/c. The tuned in momentum was 363.71 MeV/c indicating a difference of about 3 promille. From the energy calibration of the 220 MeV settings a deviation of about 2 promille of the tuned in momentum was measured. Therefore the available beamline settings were considered as trustfull and used in our experiment. The energy of the other beam line settings is calculated from the proton momentum and the setting of the momentum selecting magnet ASM11:

$$P = \frac{ASM11(P)}{ASM11(363.71\ \frac{\mathrm{MeV}}{c})} 363.71\ \frac{\mathrm{MeV}}{c}$$

In table C.1 the proton momentum and the corresponding pion energies are given.

Table C.1: *Pion energies of the πM1 channel right behind the production target, calculated from the proton momentum*

P_{proton} [MeV/c]	ASM11 setting value [arbitrary units]	T_{beam} [MeV]	T_{thick} [MeV]
363.71	41439	250	247.001
331.40	37758	220	216.994
309.64	35279	200	196.956
287.53	32760	180	176.857
275.03	31335	168	164.887
241.97	27596	140	136.765
230.49	26261	130	126.696
218.91	24941	120	116.624
206.91	23574	110	106.881
194.70	22183	90	96.465
169.49	19311	80	76.100
156.28	17806	70	65.882
142.68	16256	60	55.550

Appendix D

Trigger for the SCXBOX detector

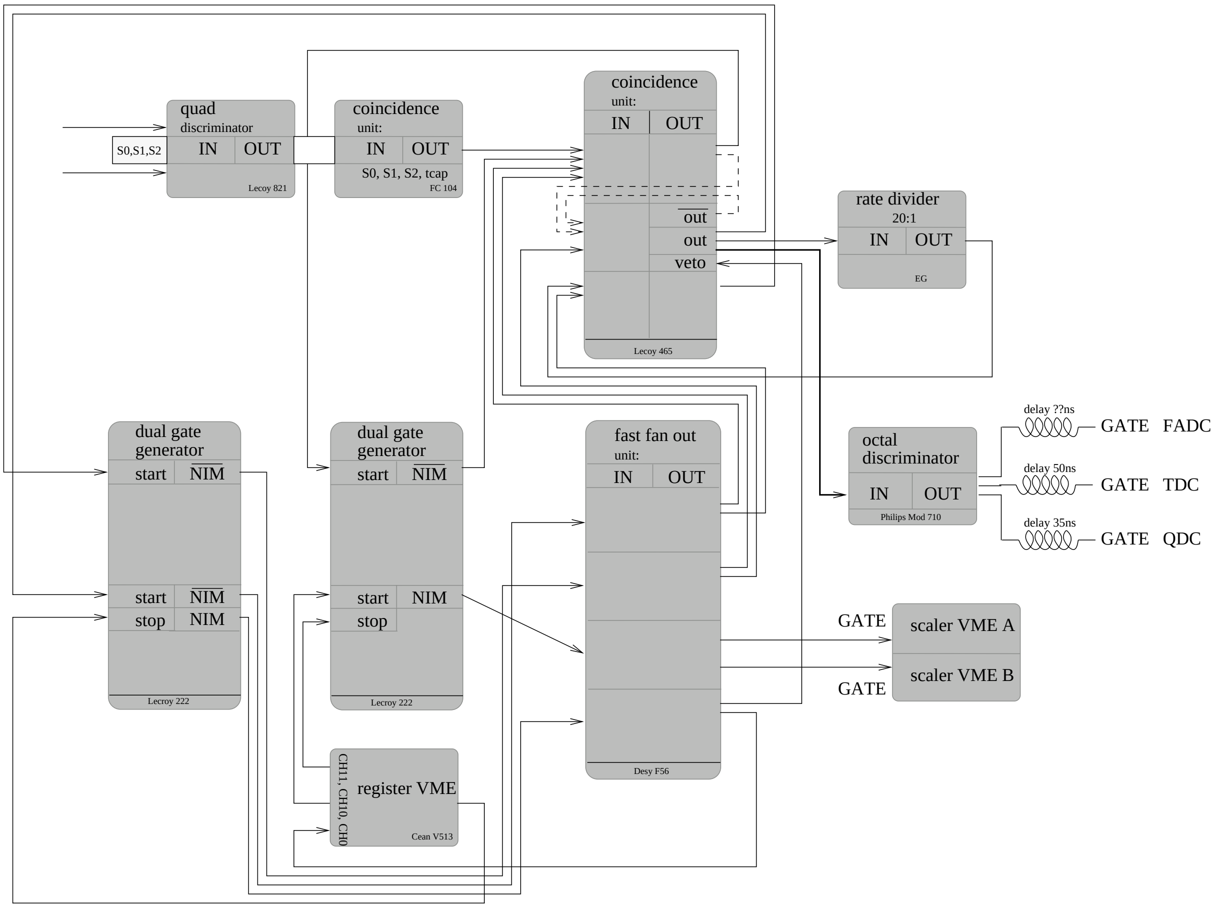

Figure D.1: *Connection diagram of the SCXBOX trigger*

Appendix E

Scintillator

EJ-200 Plastic Scintillator

This plastic scintillator combines the two important properties of long attenuation length and fast timing and is therefore particularly useful for time-of-flight systems using scintillators greater than one meter long. Typical measurements of 4 meter optical attenuation length are achieved in strips of cast sheet in which a representative size is 2cm x 20cm x 300cm.

The combination of long attenuation length, high light output, and emission spectrum well matched to the common photomultipliers recommends EJ-200 as the detector of choice for many industrial applications such as gauging and environmental protection where high sensitivity of signal uniformity are critical operating requirements.

Physical and Scintillation Constants:

Light Output, % Anthracene..........................	64
Scintillation Efficiency, photons/1 MeV e........	10,000
Wavelength of Max. Emission, nm..................	425
Rise Time, ns..	0.9
Decay Time, ns...	2.1
Pulse Width, FWHM, ns...............................	~2.5
No. of H Atoms per cm^3, x 10^{22}....................	5.23
No. of C Atoms per cm^3, x10^{22}.....................	4.74
No. of Electrons per cm^3, x 10^{23}...................	3.37
Density, g/cc:..	1.032

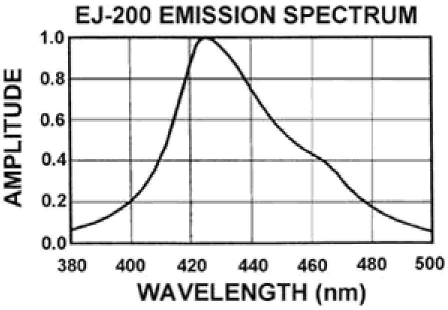

Polymer Base:	Polyvinyltoluene
Refractive Index:	1.58
Vapor Pressure:	Is vacuum-compatible
Coefficient of Linear Expansion:	7.8 x 10E-5 below +67° C
Light Output vs. Temperature:	At +60° C, L.O.=95% of that at +20° C No change from +20° C to -60° C
Chemical Compatability:	Is attacked by aromatic solvents, chlorinated solvents, ketones, solvent bonding cements, etc. It is stable in water, dilute acids and

alkalis, lower alcohols and silicone greases. It is safe to use most epoxies and "super glues" with EJ-200.

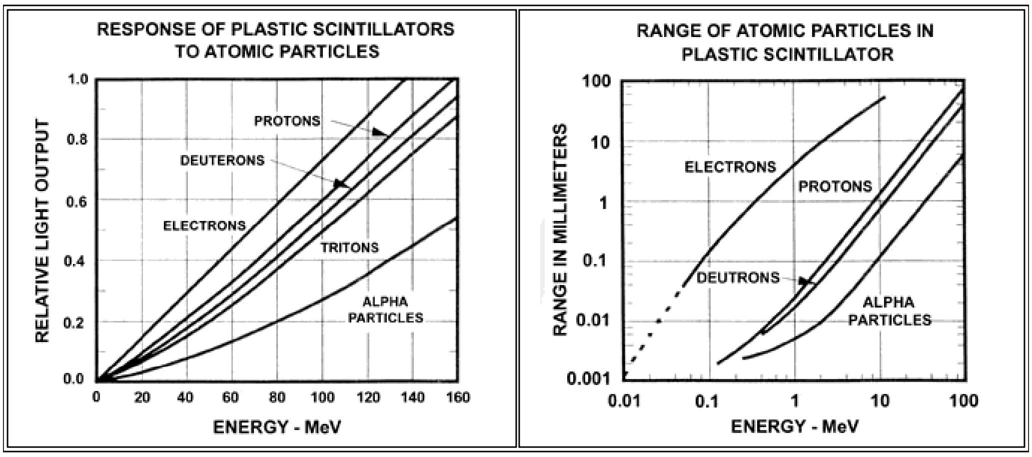

Return to Eljen Technology Home Page

For questions please contact Eljen Technology at: eljen@eljentechnology.com
Page last updated: September 30, 1999

Figure E.1: *Data sheet of the scintillator EJ-200*

Appendix F

Photomultipliers

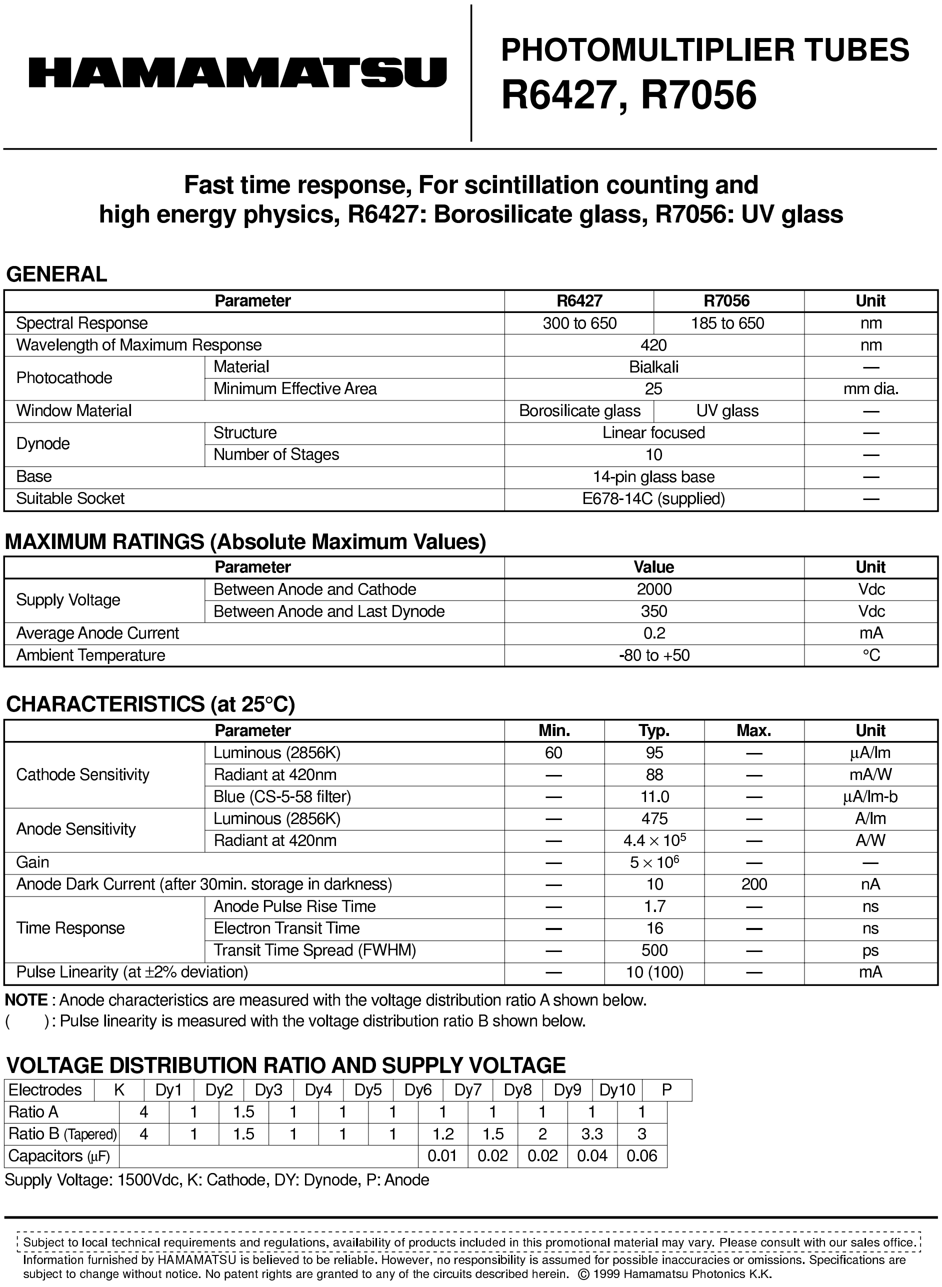

HAMAMATSU

PHOTOMULTIPLIER TUBES
R6427, R7056

Fast time response, For scintillation counting and high energy physics, R6427: Borosilicate glass, R7056: UV glass

GENERAL

Parameter		R6427	R7056	Unit
Spectral Response		300 to 650	185 to 650	nm
Wavelength of Maximum Response		420		nm
Photocathode	Material	Bialkali		—
	Minimum Effective Area	25		mm dia.
Window Material		Borosilicate glass	UV glass	—
Dynode	Structure	Linear focused		—
	Number of Stages	10		—
Base		14-pin glass base		—
Suitable Socket		E678-14C (supplied)		—

MAXIMUM RATINGS (Absolute Maximum Values)

Parameter		Value	Unit
Supply Voltage	Between Anode and Cathode	2000	Vdc
	Between Anode and Last Dynode	350	Vdc
Average Anode Current		0.2	mA
Ambient Temperature		-80 to +50	°C

CHARACTERISTICS (at 25°C)

Parameter		Min.	Typ.	Max.	Unit
Cathode Sensitivity	Luminous (2856K)	60	95	—	μA/lm
	Radiant at 420nm	—	88	—	mA/W
	Blue (CS-5-58 filter)	—	11.0	—	μA/lm-b
Anode Sensitivity	Luminous (2856K)	—	475	—	A/lm
	Radiant at 420nm	—	4.4×10^5	—	A/W
Gain		—	5×10^6	—	—
Anode Dark Current (after 30min. storage in darkness)		—	10	200	nA
Time Response	Anode Pulse Rise Time	—	1.7	—	ns
	Electron Transit Time	—	16	—	ns
	Transit Time Spread (FWHM)	—	500	—	ps
Pulse Linearity (at ±2% deviation)		—	10 (100)	—	mA

NOTE : Anode characteristics are measured with the voltage distribution ratio A shown below.
(   ) : Pulse linearity is measured with the voltage distribution ratio B shown below.

VOLTAGE DISTRIBUTION RATIO AND SUPPLY VOLTAGE

Electrodes	K	Dy1	Dy2	Dy3	Dy4	Dy5	Dy6	Dy7	Dy8	Dy9	Dy10	P
Ratio A	4	1	1.5	1	1	1	1	1	1	1	1	
Ratio B (Tapered)	4	1	1.5	1	1	1	1.2	1.5	2	3.3	3	
Capacitors (μF)							0.01	0.02	0.02	0.04	0.06	

Supply Voltage: 1500Vdc, K: Cathode, DY: Dynode, P: Anode

Figure F.1: *Data sheet of the photomultiplier HM-6427*

PHOTOMULTIPLIER TUBES R6427, R7056

Figure 1: Typical Spectral Response

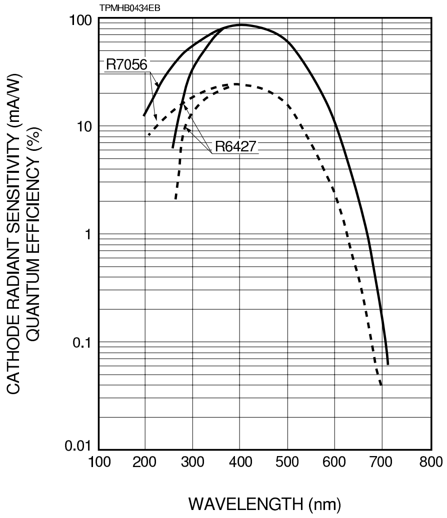

Figure 2: Typical Gain

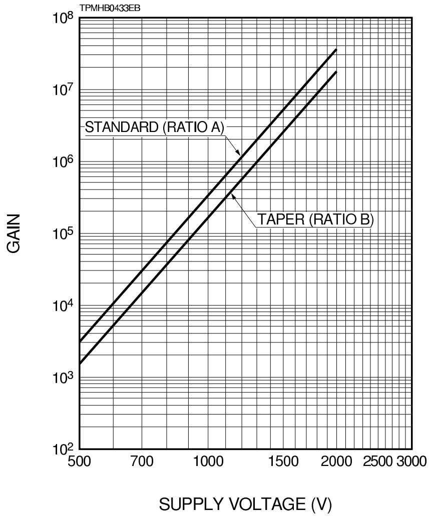

Figure 3: Typical Pulse Height Distribution (P.H.D.)

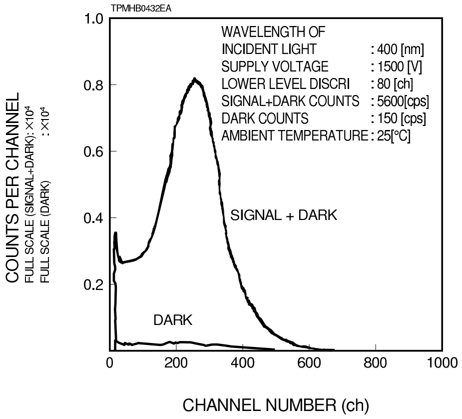

Figure 4: Time Response

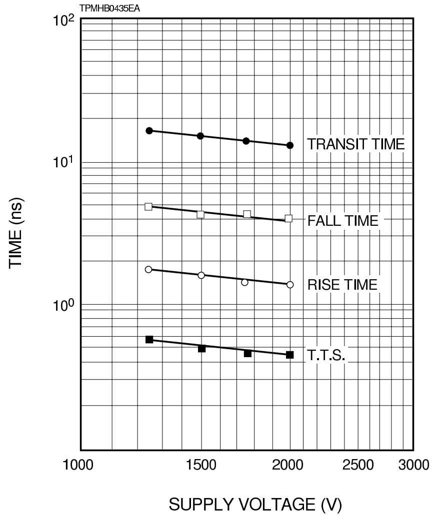

Figure F.2: *Data sheet of the photomultiplier HM-6427 continued*

Figure 5: Anode Output Waveform

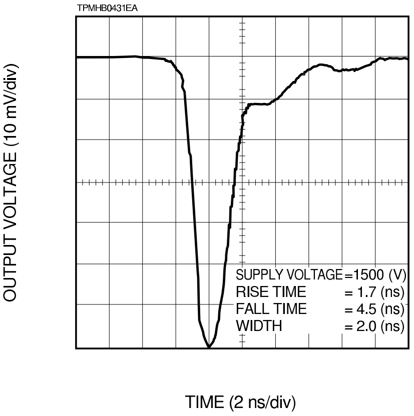

Figure 6: Transit Time Spread (T.T.S.)

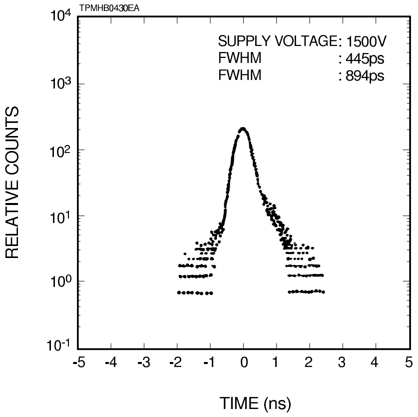

Figure 7: Dimensional Outline and Basing Diagram (Unit: mm)

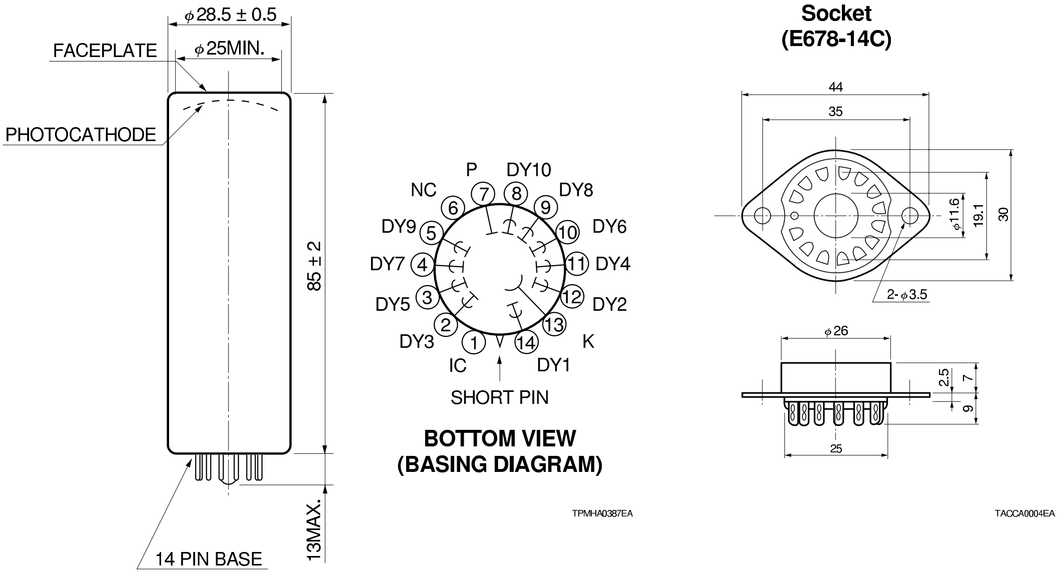

Figure F.3: *Data sheet of the photomultiplier HM-6427 continued*

PHOTOMULTIPLIER TUBES R6427, R7056

[ACCESSORIES]

●D-type Socket Assembly E2624-14 (for RATIO A)

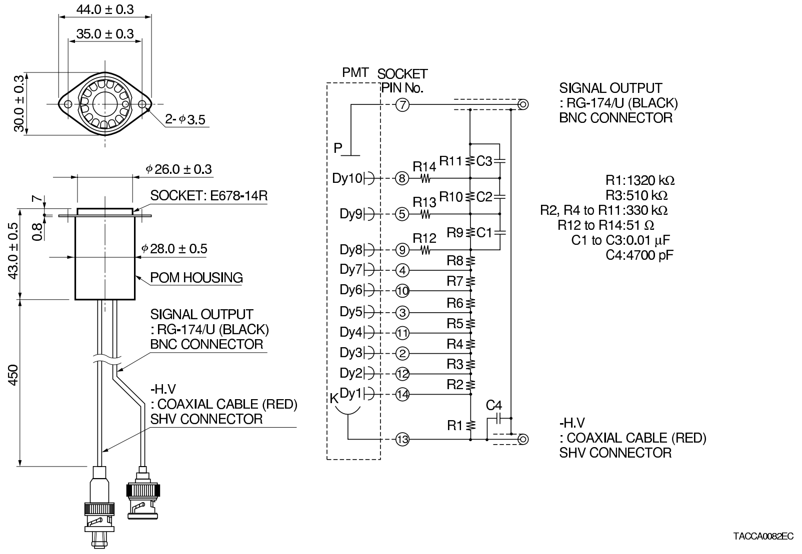

●D-type Socket Assembly E2624-04 (for RATIO B)

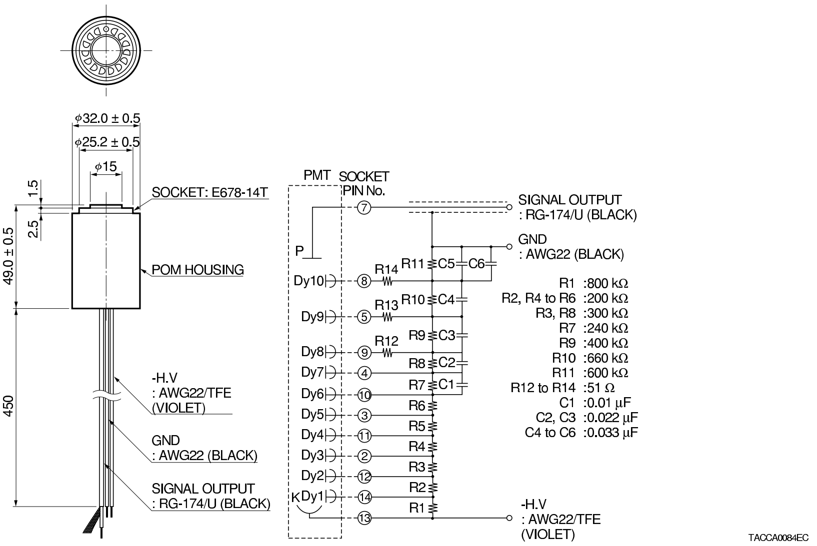

HAMAMATSU HOMEPAGE URL http://www.hamamatsu.com
HAMAMATSU PHOTONICS K.K., Electron Tube Center
314-5, Shimokanzo, Toyooka-village, Iwata-gun, Shizuoka-ken, 438-0193, Japan, Telephone: (81)539/62-5248, Fax: (81)539/62-2205
U.S.A.: Hamamatsu Corporation: 360 Foothill Road, P. O. Box 6910, Bridgewater. N.J. 08807-0910, U.S.A., Telephone: (1)908-231-0960, Fax: (1)908-231-1218
Germany: Hamamatsu Photonics Deutschland GmbH: Arzbergerstr. 10, D-82211 Herrsching am Ammersee, Germany, Telephone: (49)8152-375-0, Fax: (49)8152-2658
France: Hamamatsu Photonics France S.A.R.L.: 8, Rue du Saule Trapu, Parc du Moulin de Massy, 91882 Massy Cedex, France, Telephone: (33)1 69 53 71 00, Fax: (33)1 69 53 71 10
United Kingdom: Hamamatsu Photonics UK Limited: Lough Point, 2 Gladbeck Way, Windmill Hill, Enfield, Middlesex EN2 7JA, United Kingdom, Telephone: 44(20)8-367-3560, Fax: 44(20)8-367-6384
North Europe: Hamamatsu Photonics Norden AB: Smidesvägen 12, SE-171-41 SOLNA, Sweden, Telephone: (46)8-509-031-00, Fax: (46)8-509-031-01
Italy: Hamamatsu Photonics Italia: S.R.L.: Strada della Moia, 1/E, 20020 Arese, (Milano), Italy, Telephone: (39)02-935 81 733, Fax: (39)02-935 81 741

TPMH1187E04
DEC. 1999 SI
Printed in Japan (1000)

Figure F.4: *Data sheet of the photomultiplier HM-6427 continued*

Appendix G

Component drawing of the light guides

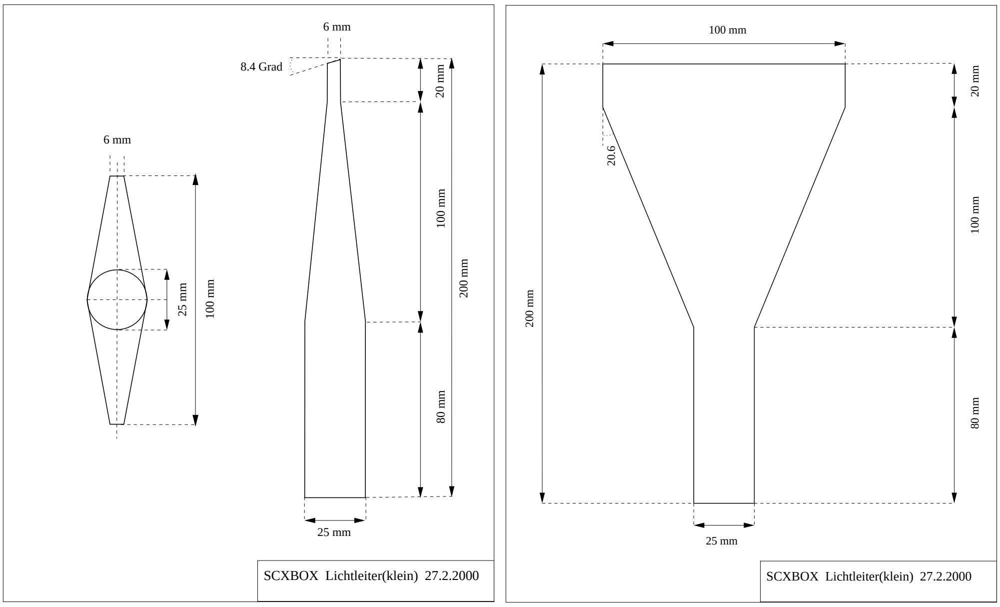

Figure G.1: *Component of the light guides for the front, back, up and down counter*

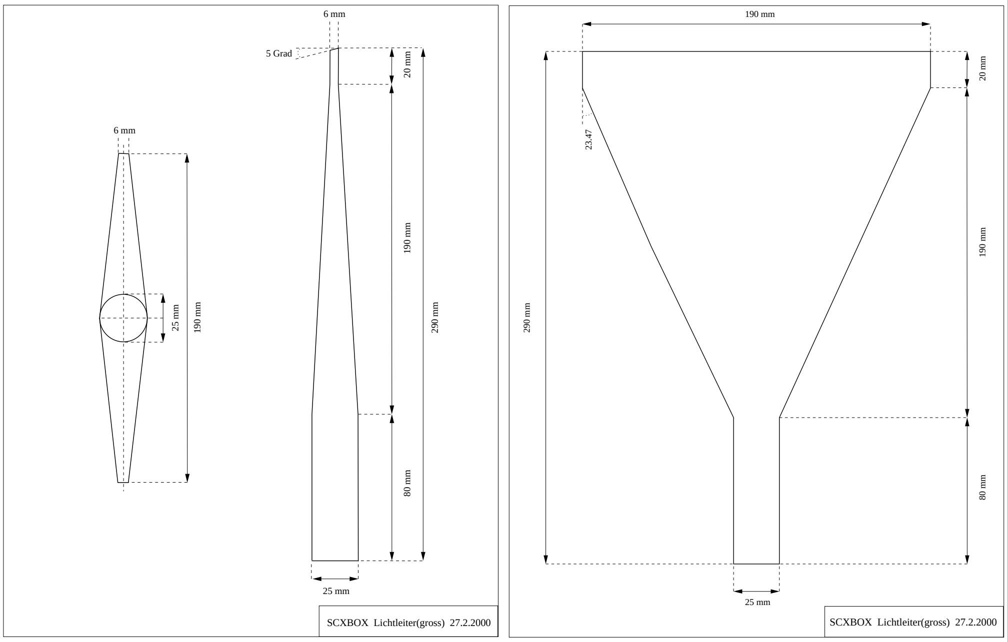

Figure G.2: *Component of the light guides for the up and down counters*

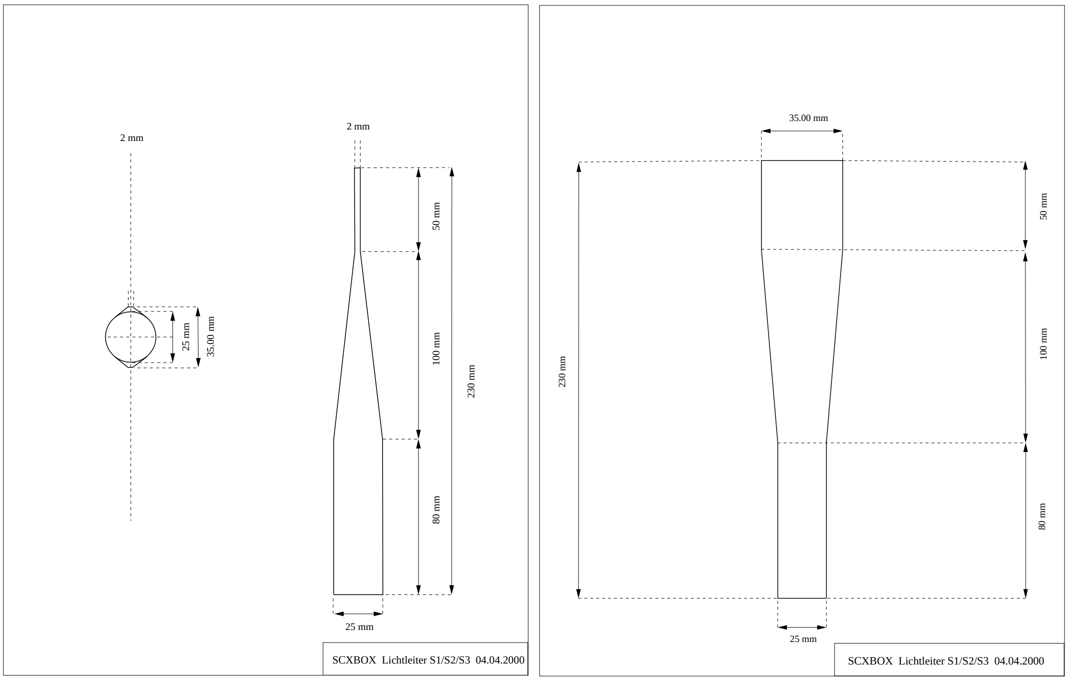

Figure G.3: *Component drawing of the light guides for the S1 and S2 counters*

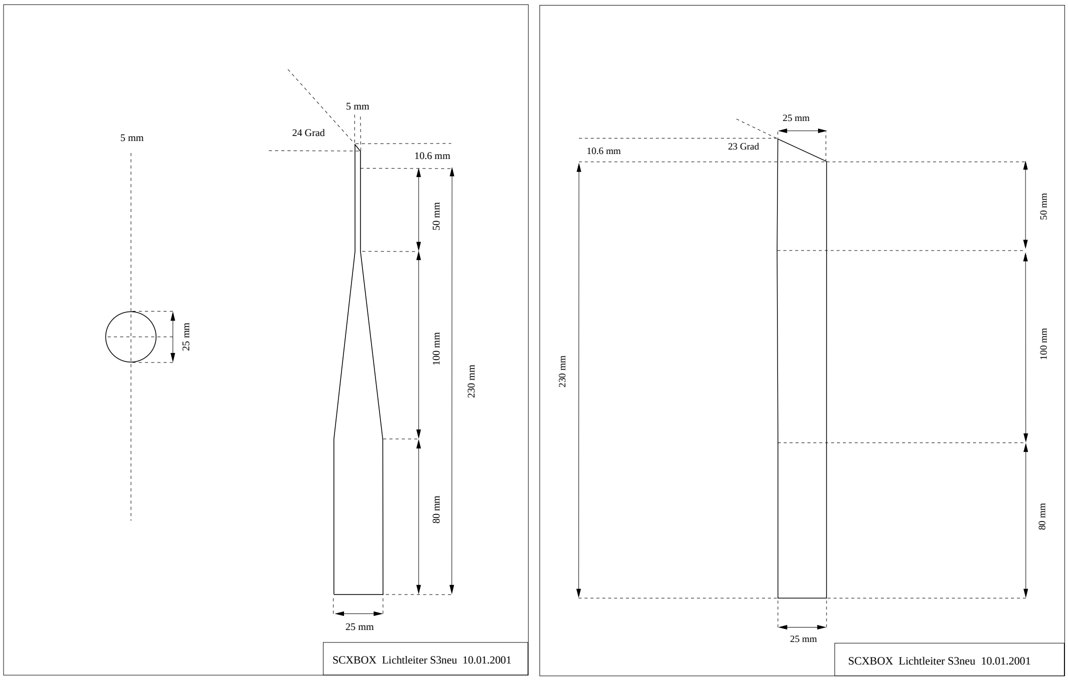

Figure G.4: *Component drawing of the light guides for the S3 counter*

Appendix H

Component drawing of the target holder

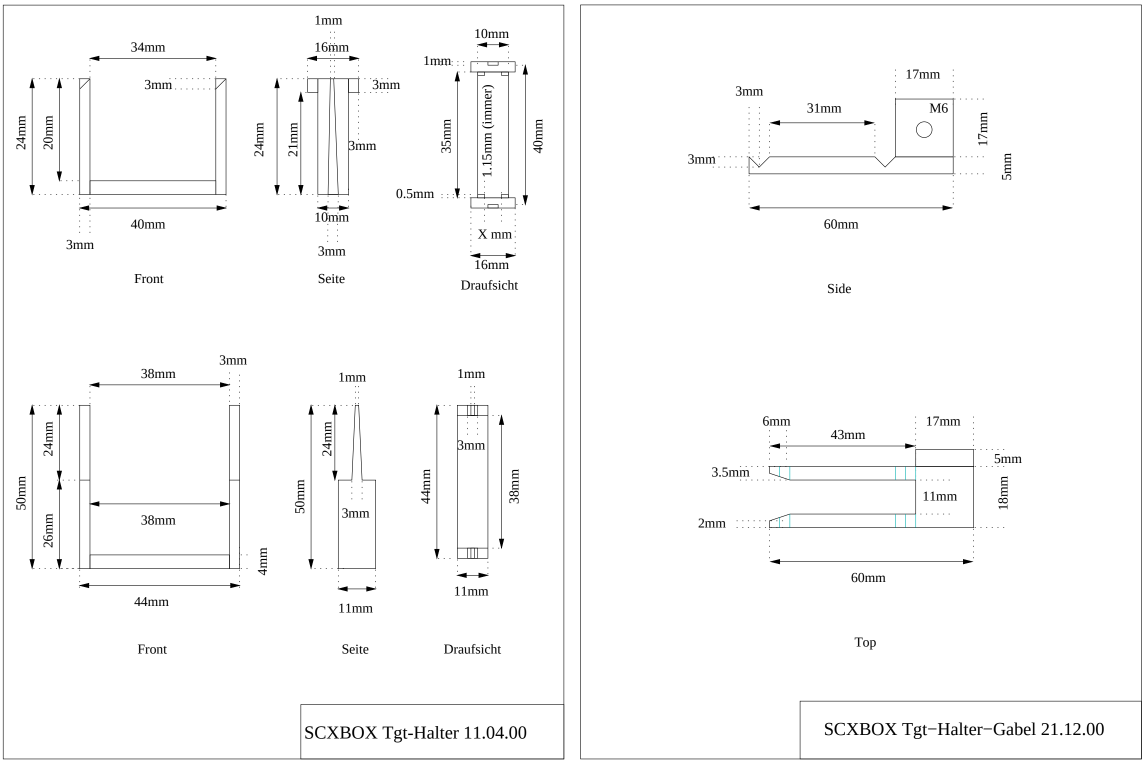

Figure H.1: *Component drawing of the target holder*

Appendix I

Component drawing of the photomultiplier holder

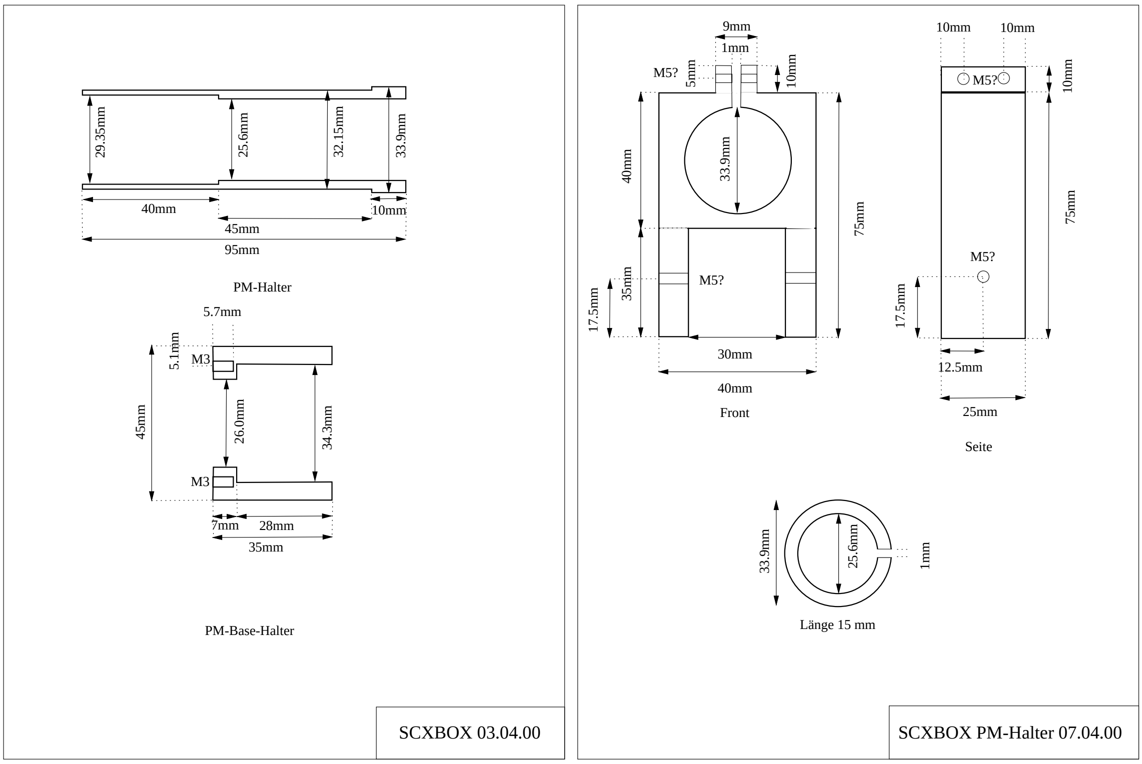

Figure I.1: *Component drawing of the photomultiplier holder*

Bibliography

[Bag88a] A. Bagheri et al,. Phys. Rev. C **38**, 875 (1988)

[Bag88b] A. Bagheri et al,. Phys. Rev. C **38**, 885 (1988)

[Bau03] M. Bauer, *Simulationen zur Messung des totalen Wirkungsquerschnittes der* $\pi^- p \rightarrow \pi^0 n$ *Ladungsaustauschreaktion*, Diplomarbeit, Universität Tübingen, 2003

[Bra90] J. Brack et al., Phys. Rev. C **41**, 2202 (1990)

[Ber72] P. A. Berardo et al., PRD6, **756** (1972)

[Bug71] D. V. Bugg et al., Nucl. Phys. B **26**, 588 (1971)

[CERN] CERNLIB Documentation Homepage: http://wwwinfo.cern.ch/asdoc/

[Cha97] Chatellard et al., Nucl. Phys. A **625**, 855 (1997)

[Com75] J. C. Comiso et al., PRD12, **738** (1975)

[Com99] J. Comfort et al., PSI research proposal R-99-02.1 (1999)

[Den98] H. Denz, *Vorbereitung von Experimenten zur Untersuchung der* πp*-Streuung*, Diplomarbeit, Universität Tübingen, 1998

[Den04] H. Denz, *Differential Cross Sections in* $\pi^\pm$ *Scattering at Low Energies*, Phd Thesis, Universität Tübingen, 2004

[DIR94] Proposal of the DIRAC-experiment at CERN (1994): http://www.cern.ch/DIRAC

[Fet99] N. Fettes et al., Phys. Lett. B **451**, 233 (1999)

[Fet01] N. Fettes, U.-G. Meißner et al., Phys. Rev. C **63**, 045201 (2001)

[FM97] N. Fettes und E. Matsinos, Phys. Rev. C **55**, 464 (1997)

[Fri93] E. Friedman et al., Phys. Lett. B **302**, 18 (1993)

[Fri05] private communication E. Friedman, The Hebrew University Jerusalem, 2005

[Fra67] S. G. F. Frank et al., Proc. Phys. Soc. (London) **69**, 609 (1967)

[GAK95] W. Gibbs, L. Ai, W. Kaufmann, Phys. Rev. Lett. **74**, 3740 (1995)

[GEANT3] GEANT: Detector Description and Simulation Tool, CERN Program Library Long Writeup W5013, http://wwwinfo.cern.ch/asdoc/pdfdir/geant.pdf

[GEANT4] GEANT4 Homepage: http://wwwinfo.cern.ch/asd/geant4/geant4.html

[Ham98] Hamamatsu Photodiodes Katalog, Hamamatsu Photomultiplier Katalog 1998

[ITM05] *Item MB building kit system* http://www.item-international.com 2005

[KH80] R. Koch, E. Pietarinen, Nucl. Phys. A **336**, 331 (1980)

[Hof98] G. Hofman et al., Phys. Rev. C **58**, 3484 (1998)

[Hof03] G. Hofman et al., Phys. Rev. C **68**, 018202 (2003)

[Kol69] D. S. Koltun, *Advances in Nuclear Physics*, Plenum Press 1969

[Leo94] W. R. Leo: *Techniques for Nuclear and Particle Physics Experiments*, Second Revised Edition, Springer, Berlin 1994

[Loc69] W. O. Lock, D. F. Meadsday *Intermediate Energy Nuclear Physics*, METHUEN & CO LTD 1970

[Mat97a] E. Matsinos, πN-Newsletter **13**, 132 (1997)

[Mat97b] E. Matsinos, Phys. Rev. C **56**, 3014 (1997)

[Mei04] R. Meier et al., Phys. Rev. Lett B **588**, 155 (2004)

[MID01] S.Ritt, $MIDASdataacquisitionsystem$, http://midas.psi.ch, 2001

[Nat99] National Semionductor Datenbl"atter 1999: http://www.national.com/pf/CL/CLC449.html

[Pav01] M. M. Pavan et al., Phys. Rev. C **64**, 064011 (2001)

[PAW] Cern, *Physics Analysis Workstation* ,http://wwwasd.web.cern.ch/wwwasd/paw/

[PDB] Phys. Let. B **592**, (2004)

[Ped78] E. Pedroni, Nucl. Phys. A **300**, 321 (1978)

[Phi94] Phillips Photonics, *photomultiplier tubes*, principles & applications (1994)

[PSI94] H. C. Walter et al., *PSI – Users' Guide – Accelerator Facilities*, Paul Scherrer Institut, 1994

[PSIM1] PSI beamlines, http://aea.web.psi.ch/beam2lines/ 2005

[PSIE3] PSI beamlines, http://aea.web.psi.ch/beam2lines/ 2005

[PPB02] K. Hagiwara et al., Phys. Rev. D **66**, 0100001 (2002)

[Sad04] M. E. Sadler et al., Phys. Rev. C **69**, 055206 (2004)

[SAID] CNS, Center for Nuclear Studies, Data Analysis Center: http://lux2.phys.va.gwu.edu/ (used solution FA02)

[Sal84] M. Salomon et al., Nucl. Phys. A **414**, 493 (1984)

[Sch05] private communication S. Scholl, Universität Tübingen, 2005

[Sev89] M. Sevior et al., Phys. Rev. C **40**, 2780 (1989)

[Wie95] R. Wieser, *Bestimmung der Analysierstärke der elastischen* $\pi^+\vec{p}$*-Streuung bei* T_π*=68.3 MeV*, Dissertation, Universität Karlsruhe, 1995

[Yuk35] H. Yukawa, Proc. Phys. Math. Soc. Japan **17**, 48 (1935)

List of Figures

List of Tables

Danksagung

Ich möchte mich an dieser Stelle bei allen bedanken, ohne die diese Arbeit nicht möglich gewesen wäre.

Zuerst geht mein Dank an meinen Betreuer Herr Prof. G. J. Wagner der sich sehr viel Zeit nahm und mit mir viel Geduld hatte. Besser und intensiver kann man nicht betreut werden.

Herrn Prof. H. Clement danke ich für die stetige Begleitung und dafür, daß er als Anlaufstelle für fachliche Probleme zur Verfügung stand.

Ohne PD Dr. R. Meier, der stets eine Antwort auf meine Fragen wußte, wäre dieses Experiment niemals aufgebaut und durchgeführt worden.

E. Friedman war mir zu jeder Zeit eine große Hilfe und stand mit Rat und Tat bereit. Die Strahlzeiten mit ihm werde ich in sehr guter Erinnerung behalten.

Ein spezielles Dankeschön geht an die Herren W. Rochow und M. Brandt, die sehr hilfsbereit waren. Besonders beim Polieren der Lichtleiter haben sie mir geduldig und gewissenhaft geholfen.

Den Werkstätten am Physikalischen Institut und deren Leitern Herr G. Brodbeck und Herr H. Schreyer danke ich für die Unterstützung während des Aufbaus des Detektors. Die experimentelle Arbeit hat mit der professionellen Hilfe der Angestellten des PSI immer Spaß gemacht. Ein “merci” in die Schweiz.

Die Arbeitsatmosphäre am PIT war ohne Ausnahme sehr herzlich und angenehm. Daher an alle Mitarbeiter, Doktoranden, Diplomanden welche bisher nicht namentlich genannt wurden, vielen Dank für die gute Atmosphäre und Unterstützung.

Ich danke auch allen Freunden, die meine Hochs und Tiefs mit allen meinen Launen ertragen mußten und an mich geglaubt haben.

Bei meinen Schwestern und meiner Mutter bedanke ich mich dafür, daß sie nie an mir zweifelten, immer ein offenes Ohr hatten und für mich da waren.

Zuletzt gilt mein Dank meinem vor über 12 Jahren verstorbenen Vater, ohne dessen Ermutigung und Unterstützung, finanziell wie moralisch, seine 4 Kinder sicher nicht studiert und promoviert hätten.